Masters Thesis

Design and Performance Comparison of a Horizontal Axis Wind Turbine and a Cross Flow Type Wind Turbine

Supervisor: Professor Young-Ho LEE

December 2012

Graduate School of Korea Maritime University

Department of Mechanical Engineering

Joji Vulibeci Wata

We certify that we have read this thesis and that, in our opinion, it is satisfactory in scope and quality as a thesis for the degree of Master of Mechanical Engineering, submitted by **Joji Vulibeci Wata**.

THESIS COMMITTEE

Chairperson: Prof. Dr. Kweon-Ha PARK
Division of Mechanical & Energy System Engineering, Korea Maritime University

Co-Chairperson: Prof. Dr. Hyung-Ho JUNG
Division of Mechanical & Energy System Engineering, Korea Maritime University

Supervisor: Prof. Dr. Young-Ho LEE
Division of Mechanical & Energy System Engineering, Korea Maritime University

December 2012

Department of Mechanical Engineering

Graduate School of Korea Maritime University

본 論文을 조지 블리베시 와타의 工學碩士
學位論文으로 認准함

위원장: 공학박사 박권하 (인)

위원: 공학박사 정형호 (인)

위원: 공학박사 이영호 (인)

2012 년 12 월 29 일

한국해양대학교 대학원

기계공학과

TABLE OF CONTENTS

List of Tables .... **III**

List of Figures .... **IV**

Abstract .... **VII**

Nomenclature .... **IX**

Chapter 1 Introduction **1**

- 1.1 Background 1
  - 1.1.1 Classifications of wind turbines 2
- 1.2 Motivation for study 6

Chapter 2 Basic theory of wind turbines **7**

- 2.1 Betz theory 7
  - 2.2 Blade element momentum theory 10
  - 2.2.1 The momentum theory 10
  - 2.2.2 Rotating wake/ Rotating annular stream tube 12
  - 2.2.3 Blade element theory 14
- 2.3 Prandtl’s tip loss factor 17
- 2.4 Design of a horizontal axis wind turbine blade 18
- 2.5 Cross flow type wind turbine 22

Chapter 3 Methodology **24**

- 3.1 Numerical modeling 24
- 3.2 Turbulence models 25
  - 3.2.1 Two equation turbulence models 25
- 3.3 Creating the geometry 29
  - 3.3.1 Model of horizontal axis wind turbine (HAWT) 29
  - 3.3.2 Model of the cross flow turbine 29
- 3.4 Mesh generation 40
  - 3.4.1 Horizontal axis wind turbine mesh 40
  - 3.4.2 Cross flow turbine mesh 42

3.5 Simulation setup 47

3.5.1 HAWT setup in CFX Pre 47

3.5.2 Cross flow turbine setup in CFX Pre 49

3.6 Solving the simulation 51

3.7 Post processing 51

Chapter 4 Results and Discussion 53

4.1 Horizontal axis wind turbine analysis 53

4.1.1 Power output 53

4.1.2 Streamlines 55

4.2 Cross flow wind turbine analysis 57

4.2.1 Turbine entry arc analysis results 57

4.2.2 Nozzle shape analysis 64

4.2.3 Diffuser entry arc analysis 74

4.2.4 Diffuser shape analysis 75

4.3 Comparison of the HAWT and cross flow turbine 78

Chapter 5 Conclusion 80

Acknowledgement 82

References 83

List of Tables

Table 1.1: Classification of wind turbine systems by rotor size 6
Table 2.1: Design Parameters for the HAWT 18
Table 3.1: Number of nodes in various domains 46
Table 3.2: Summary of the conditions in CFX Pre for the HAWT simulation............... 48
Table 3.3: Summary of the conditions for the cross flow turbine 50

List of Figures

Figure 1.1: A simplified diagram of the global wind flow patterns 2
Figure 1.2: A Savonius rotor is an example of a Drag type Wind turbine 3
Figure 1.3: Examples of VAWTs 4
Figure 1.4: Example of a HAWT with various parts labeled 5
Figure 2.1: Flow conditions for a disk shaped wind convertor 8
Figure 2.2: The relationship between the power coefficient and the velocity ratio 10
Figure 2.3: The simplified flow with several points for consideration 11
Figure 2.4: The wind turbine in the rotating wake theory 13
Figure 2.5: The Blade Element Theory analyses forces at N sections of the blade 14
Figure 2.6: Relationships between the flow velocities and forces on an airfoil 15
Figure 2.7: Power versus wind speed curve for two types of power control methods 19
Figure 2.8: Top view of a HAWT blade span with the highlighted areas indicating the regions for various airfoils 20
Figure 2.9: Chord distribution of the airfoil along the blade span 21
Figure 2.10: The twist distribution of the airfoils on the HAWT 22
Figure 3.1: Cross sections of the horizontal axis wind turbine 29
Figure 3.2: Cross flow turbine 30
Figure 3.3: Overall geometry of the cross flow turbine with the nozzle and turbine 30
Figure 3.4: The Turbine Entry Arc angle δ 31
Figure 3.5: Entry arc angle 30° case 32
Figure 3.6: Entry arc angle 90° 32
Figure 3.7: Entry arc angle 120° 33
Figure 3.8: Entry arc angle 135° 33
Figure 3.9: Nozzle analysis: Case 1 34
Figure 3.10: Nozzle analysis: Case 2 34
Figure 3.11: Nozzle analysis: Case 3 35
Figure 3.12: Nozzle analysis: Case 4 35
Figure 3.13: Nozzle analysis: Case 5 36
Figure 3.14: Nozzle analysis: Case 6 36
Figure 3.15: Diffuser entry angle 90° 37
Figure 3.16: Diffuser entry arc Angle 135° 37
Figure 3.17: Diffuser analysis: Case 1 38
Figure 3.18: Diffuser analysis: Case 2 38
Figure 3.19: Diffuser analysis: Case 3 39
Figure 3.20: Diffuser analysis: Case 4 39

Figure 3.21: Computational Grid of the domain for the wind turbine 41
Figure 3.22: Meshing near the Blade.. 41
Figure 3.23: Mesh volumes Surrounding the blade.. 42
Figure 3.24: Computational grid of the domain for the cross flow turbine.................... 43
Figure 3.25: Mesh of the nozzle 44
Figure 3.26: Mesh of the top strip part of the turbine.. 44
Figure 3.27: Mesh of the internal fluid domain... 45
Figure 3.28: Mesh for the turbine blade 45
Figure 3.29: Mesh for the diffuser.. 46
Figure 3.30: The setup of the HAWT simulation 47
Figure 3.31: Setup of the HAWT simulation indicating the interface region................ 48
Figure 3.32: Overview of the whole domain with the various boundary conditions shown... 49
Figure 3.33: The setup of the cross flow turbine parts. A case surrounds the turbine parts. 50
Figure 4.1: HAWT power output (kW) at various wind speeds (m/s)............................ 53
Figure 4.2: Power coefficient at various wind speeds.. 54
Figure 4.3: Streamlines over the suction side of the blade at 7m/s 55
Figure 4.4: Streamlines over the suction side of the blade at 10m/s 55
Figure 4.5: Streamlines over the suction side of the blade at 15m/s 56
Figure 4.6: Streamlines over the Suction side of the blade at 20m/s 56
Figure 4.7: Power coefficient versus Tip speed ratio for turbine entry arc analysis 58
Figure 4.8: Velocity contours at turbine entry arc at 30°.. 59
Figure 4.9: Pressure contours at the turbine entry arc at 30°.. 59
Figure 4.10: Velocity contours at the turbine entry arc at 90°.. 60
Figure 4.11: Pressure contours at the turbine entry arc at 90°.. 60
Figure 4.12: Velocity contours at the turbine entry arc at 120°...................................... 61
Figure 4.13: Pressure contours at the turbine entry arc at 120°...................................... 61
Figure 4.14: Velocity contours at the Turbine Entry Arc at 135° 62
Figure 4.15: Pressure Contours at the Turbine Entry Arc at 135° 62
Figure 4.16: Flow rate at the turbine entry arc for the arc angle analysis 63
Figure 4.17: Velocity profile over the inlet of the nozzle... 64
Figure 4.18: Power coefficient versus TSR for the nozzle shape analysis..................... 65
Figure 4.19: Flow rate at the entry arc for the nozzle case analysis............................... 66
Figure 4.20: Velocity profile at the turbine entry arc 67
Figure 4.21: Velocity vectors of case 1 of the nozzle analysis....................................... 68

Figure 4.22: Velocity contours of case 1 of the analysis 68
Figure 4.23: Velocity vectors of case 2 of the nozzle analysis 69
Figure 4.24: Velocity contours of case 2 of the nozzle analysis 69
Figure 4.25: Velocity vectors of case 3 of the nozzle analysis 70
Figure 4.26: Velocity contours of case 3 of the nozzle analysis 70
Figure 4.27: Velocity vectors of case 4 of the nozzle analysis 71
Figure 4.28: Velocity contours of case 4 of the nozzle analysis 71
Figure 4.29: Velocity vectors of case 5 of the nozzle analysis 72
Figure 4.30: Velocity contours of case 5 of the nozzle analysis 72
Figure 4.31: Velocity vectors of case 6 of the nozzle analysis 73
Figure 4.32: Velocity contours of case 6 of the nozzle analysis 73
Figure 4.33: Coefficient of power over various tip speed ratios for diffuser entry arc analysis 74
Figure 4.34: Flow rate for both cases at the turbine and diffuser entry arc areas........... 75
Figure 4.35: Coefficient of power at different tip speed ratios for the diffuser shape analysis 76
Figure 4.36: The flow rate of the 4 cases at the turbine entry arc region 77
Figure 4.37: Flow for the 4 cases at the diffuser entry arc region 78

Design and Performance Comparison of a Horizontal Axis Wind Turbine and Cross Flow Type Wind Turbine

Joji Vulibeci Wata

Department of Mechanical Engineering

Graduate School of Korea Maritime University

Abstract

A major concern these days is the adverse effect of human activities on the environment. Carbon emissions especially have been linked to global warming and climate change. In addition, the rising demand for energy has led many countries to look for new, renewable and environmentally friendly power sources for supply. One of these sources is the wind and this study looks two alternatives to harness the energy.

These two alternatives are wind turbines that are able to convert the kinetic energy available in the wind to useful mechanical energy which then can be used to generate electrical power. This study will investigate and compare the performance of the two types of wind turbines by using commercial CFD software. The following are several objectives of the investigation.

The first objective is to study and utilize the current theories in wind turbine technology to design a 10kW horizontal axis wind turbine blade. Once the blade is designed, the performance characteristics of the blade will be studied by using a commercial CFD code ANSYS CFX 13.0.

Once the investigation on the 10kW blade was completed, the next objective is to simulate a 10kW cross flow type wind turbine using ANSYS CFX 13.0. Also, several simulations were done to study the effect of a nozzle and diffuser on the performance of the cross flow wind turbine.

The final objective is to compare the performance characteristics of the 10kW horizontal type wind turbine to the 10kW cross flow type turbine with a nozzle and diffuser.

At the completion of this study, a horizontal axis wind turbine using 3 different airfoils was designed using various theories that were studied. This turbine was simulated using ANSYS CFX v13 and achieved an output power of 11.54kW at 10m/s and a power coefficient of 0.45 at the rated wind speed of 10m/s.

The cross flow turbine was numerically analyzed in the commercial code ANSYS CFX v13 with the nozzle and diffuser. It was found that the nozzle increased the velocity of the air entering the turbine and therefore increased the power output and power coefficient of the turbine. The diffuser did not have much effect on the performance characteristics. Furthermore, the best case turbine with a nozzle and diffuser attached produced about 2.8kW and a power coefficient of 0.11 at a wind speed of 10m/s.

Nomenclature

A:	Area	[m^2]
a:	Induction factor	
a':	Angular induction factor	
B:	Blade number	
C:	Chord length	[m]
C_P:	Power coefficient	
dF_D:	Incremental drag force	[N]
dF_L:	Incremental lift force	[N]
dF_N:	Incremental normal force	[N]
F:	Force	[N]
F_{tan}:	Tangential force	[N]
F_{thr}:	Thrust force	[N]
k:	Turbulence kinetic energy	[m^2/s^2]
KE:	Kinetic energy	[J]
$\dot{m}$:	Mass flow rate	[kgm/s]
P:	Power	[W]
P_{air}:	Available power in the air stream for conversion	[W]
P_n:	Pressure at station number n	[Pa]
P_{mech}:	Mechanical power produced of the convertor	[W]
Q:	Prandtl's tip loss factor	
r:	Radius	[m]
V:	Velocity	[m/s]
$\dot{V}$:	Volume flow rate	[m^3/s]
V_{rel}:	Relative wind speed	[m/s]
α:	Angle of attack	[°]
ρ:	Density	[kg/m^3]
ΔP:	Pressure difference between two points	[Pa]
ε:	Turbulence eddy dissipation	[m^2/s^3]
θ_p:	Section pitch angle	[°]
θ_t:	Section twist angle	[°]
φ:	Relative flow velocity angle to rotational plane	[°]

Chapter 1 Introduction

1.1 Background

One of the major concerns nowadays is the impact of human activity on the environment. Particularly, the emission of carbon dioxide from the use of non-renewable fossil fuels is a topic of much concern and debate. This is due to the fact that these fuels have been linked to global warming. In addition, an increasing demand for energy and the steady rise in fuel prices has led many countries to look for new sources of energy that are environmentally friendly and as well as renewable.

The International Energy Agency explains that [1]: “Renewable energy is derived from natural processes that are replenished constantly. In its various forms, it derives directly from the sun or from heat generated from the earth. Included in the definition is electricity and heat generated from solar, wind, ocean, hydropower, biomass, geothermal resources and bio-fuels and hydrogen derived from renewable sources”. With numerous sources of renewable energy sources available, much research is currently been undertaken to create or optimize methods to extract the energy. This study will focus on the extraction of energy from the wind.

The World Wind Energy Association published a report stating that the worldwide wind installed capacity had reached 254 GW by the first half of 2012 and it was expected to increase to 273GW by the end of 2012 [2]. It was also reported that although growth had slowed in some countries like China and United States, which currently lead the wind industry market, many other emerging countries such as Brazil and Mexico were adopting wind power to supplement the current power supplies. Furthermore, it reported that the growth in wind sector is expected to continue to increase even though some countries were experiencing financial difficulties. As interest in wind power continues to grow, more research is done to understand the wind and the methods to extract power.

The wind is caused by the pressure differences as a result of the uneven heating of the earth by the sun. At the equator, more solar radiation is absorbed than at the poles. Therefore, in a simple model, the air would rise from the equator and sink at the poles. But due to the earth’s rotation and seasonal variations in solar radiation, the circulation of the wind is much more complex. The wind blows primarily along the horizontal plane (as the vertical pressure gradient force tends to be cancelled by the gravitational force), moving from a high pressure region to a lower pressure one. A simplified figure of the directions of the wind around the earth [3] is given in Fig.1.1. This figure does not show the effect of land masses have on wind distribution.

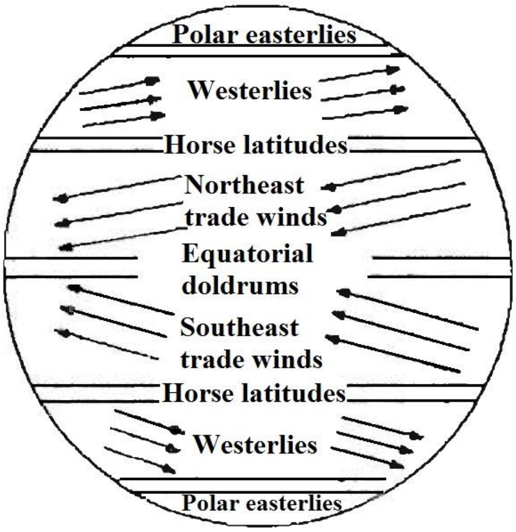

Figure 1.1: A simplified diagram of the global wind flow patterns

In addition to the pressure differences, seasonal variations of solar radiation and the earth’s rotation, the movement of the wind also affected by the inertial forces of the wind itself and the friction on the earth’s surface [4]. The movement or the kinetic energy of the wind can converted to some other form of energy by wind machines in order to be utilized in a useful manner. There are many types of wind machines available and it is useful to classify them into several categories.

1.1.1 Classifications of wind turbines

There are several ways to classify the wind machines. Some of these categories classify wind machines as lift or drag type wind machines, horizontal or vertical axis wind machines or according to their size and scale.

1.1.1.1 Lift and drag wind machines

The first type that will be discussed is the drag type wind machines. These are simplest kinds of machines that utilize the force of the wind impinging on the surface of the rotor blade/vane to drive the turbine, converting the kinetic energy into mechanical energy. An example of a drag type wind machine is given in Fig.1.2.

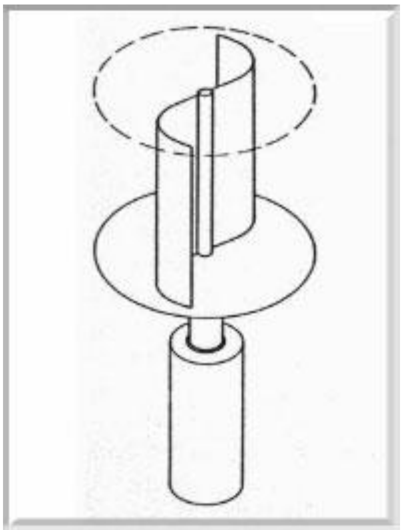

Figure 1.2: A Savonius rotor is an example of a Drag type Wind turbine

The second type is the lift type wind turbines that have rotor blade shapes that generate lift to turn the turbine. This type of turbine is mostly used today and the most common type is the propeller type turbine with a horizontal axis that uses airfoils as blade sections.

Mathematically, drag type turbines are less efficient than lift type turbines and lift type wind turbines are able to produce more power for the same surface area as a drag type wind machine [5, 6, 7]. This is due to the fact that the power producing surfaces of a drag type turbine cannot move faster than the wind and limit the relative wind speed. The relative wind is proportional to the power produced and thus a lower relative wind speed would mean that low power will produced by the turbine. On the contrary, lift type turbines are able to achieve relative wind velocities that are much greater in magnitude than the free stream velocity. Because of this, lift type turbines are utilized for power generation. Some wind machines can use a combination of lift and drag forces to convert the wind energy. These are generally not as efficient as more technologically advanced lift type turbines.

Another classification method used to classify turbines is to categorize the turbines by the rotational axis of the rotor.

1.1.1.2 Horizontal and vertical axis wind turbines

Wind machines or wind turbines are also classified by their rotational axis. These categories are known as horizontal axis wind turbines (HAWT) or vertical axis wind turbines (VAWT).

Vertical axis wind turbines are some of the oldest designs of wind rotors. Initially, VAWTs were built as drag type rotors but in 1925, the Darrieus rotor was invented that used lift. Some of examples of other types VAWTs are given in Fig.1.3. VAWTs have some advantages such as simple design, the housing of mechanical and electrical components near the ground and no yaw system.

Disadvantages include low tip ratios, low self-starting ability and the inability to control the power or speed by pitching the blades.

Horizontal axis wind turbines rotate around a horizontal axis. Most of these are designed on a propeller type concept and are the most common types of turbines used for commercial power generation. HAWTs are used because of several advantages.

Firstly, the rotor speed and power output can be controlled by pitching the rotor blades around the longitudinal axis. Secondly, the blade can be optimized aerodynamically and this will lead to higher efficiency and power output. Finally, the technology of HAWT designs is more advanced compared to that of VAWT designs.

However, HAWTs require a yawing system to ensure the wind is flowing directly into the rotor swept area for maximum efficiency and are sensitive to the turbulence in the wind. In addition, the generator must also be mounted on the nacelle at the rotor height which can complicate maintenance.

The final method that will be described here, classifies wind turbines by the size of the rotor diameter.

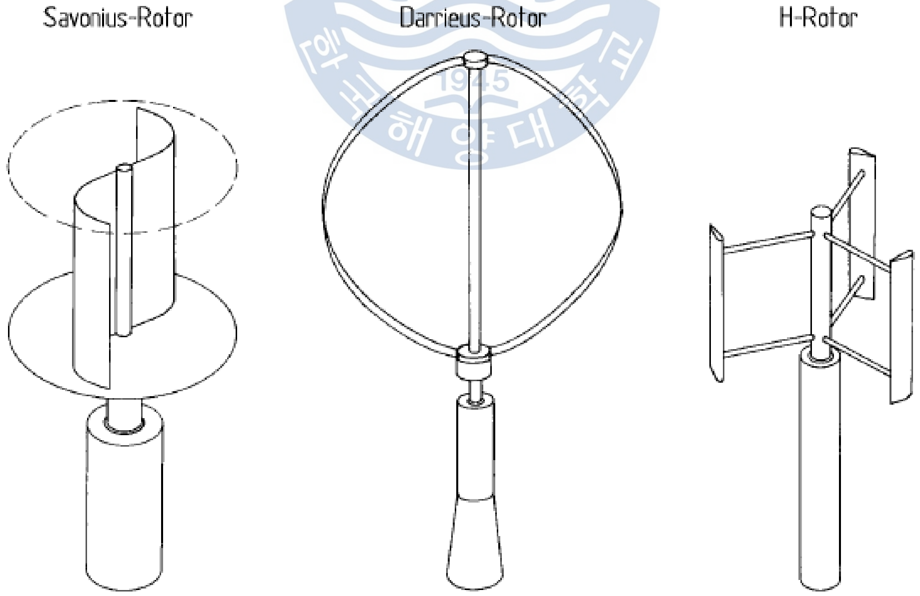

Figure 1.3: Examples of VAWTs

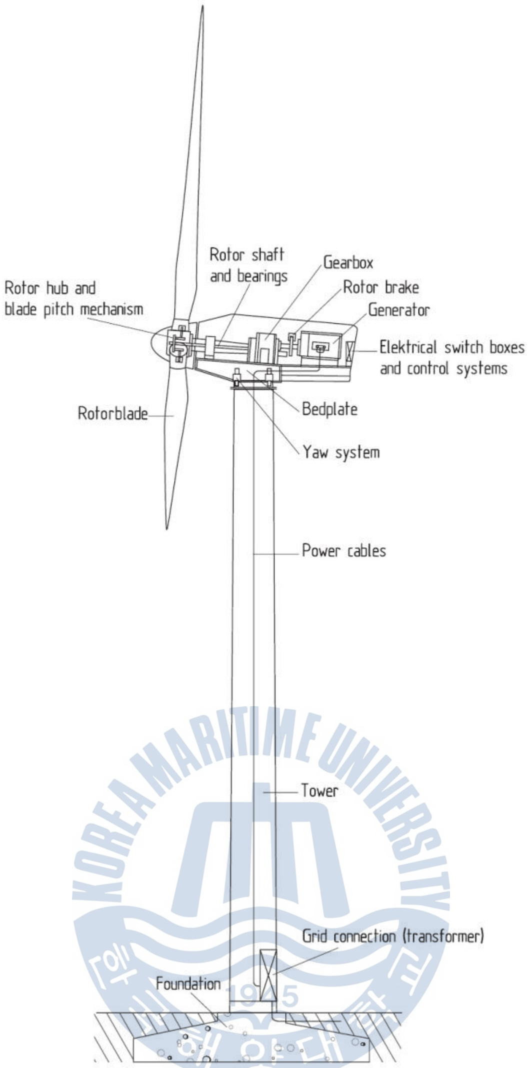

Figure 1.4: Example of a HAWT with various parts labeled

1.1.1.3 Rotor size classification of turbines

Both the output power and size of the wind turbines can vary from one machine to another. Thus a classification system that can group the various sizes into a category is very useful. The table below shows a summary of the scale and the respective power rating according to the rotor diameter of the turbine [8, 9].

Table 1.1: Classification of wind turbine systems by rotor size

Scale	Power Rating	Rotor Diameter
Micro	50 W to 2 kW	less than 3m
Small	2 kW to 40 kW	3m to 12m
Medium	40kW to 999kW	12m to 45m
Large	More than 1 MW	46m and larger

1.2 Motivation for study

This study will be looking at the design and performance of two types of small scale 10kW wind turbines that can be used for power production.

By using commercial computer-based software, a lift type HAWT and a drag type cross flow type wind turbine will be modeled and the power and performance characteristics of these two turbines will be analyzed and compared.

In order to understand the relationship between the power produced by a turbine and the physics of the flow, several theories have been developed and the accepted theories will be discussed in the next section.

Chapter 2 Basic theory of wind turbines

2.1 Betz theory

As discussed earlier, the wind turbine converts the kinetic energy of the stream into mechanical energy. The principle of this conversion was shown by Albert Betz. Betz showed how for a certain cross sectional area of an air stream, the extractable mechanical energy was restricted to a proportion of the available energy in the stream. He also found that the optimal point at which power conversion was the highest could be determined by the ratio of the flow velocity in front of the convertor to the flow velocity behind the convertor [10].

Fig.2.1 shows the flow conditions for a disk shaped wind convertor.

The kinetic energy of the air of mass (m) at a velocity (v) is given by the equation (2.1):

$$KE = \frac{1}{2} m\, v^2 \quad (Nm) \qquad (2.1)$$

The volume flow rate (V’) through a cross sectional area (A) can be expressed as the equation (2.2):

$$\dot{V} = v\, A \quad (m^3/s) \qquad (2.2)$$

Now the mass flow rate is given as equation (2.3):

$$\dot{m} = \rho\, v\, A \quad (kg/s) \qquad (2.3)$$

Combining these equations, the equation (2.4) for power in the air stream can be written as:

$$P_{air} = \frac{1}{2}\, \rho\, v^3 A \quad (W) \qquad (2.4)$$

Because mechanical energy is extracted the kinetic energy of the airstream will decrease. This means that at a constant flow rate, the reduction of the flow velocity behind the convertor will increase the size of the cross sectional area of the airstream. Therefore the mechanical energy extracted is the difference in the power of the air stream before and after the convertor given in equation (2.5):

$$P = \frac{1}{2} \rho\, A_1 {v_1}^3 - \frac{1}{2} \rho\, A_2 {v_2}^3 = \frac{1}{2} \rho\, (A_1 {v_1}^3 - A_2 {v_2}^3) \quad (W) \qquad (2.5)$$

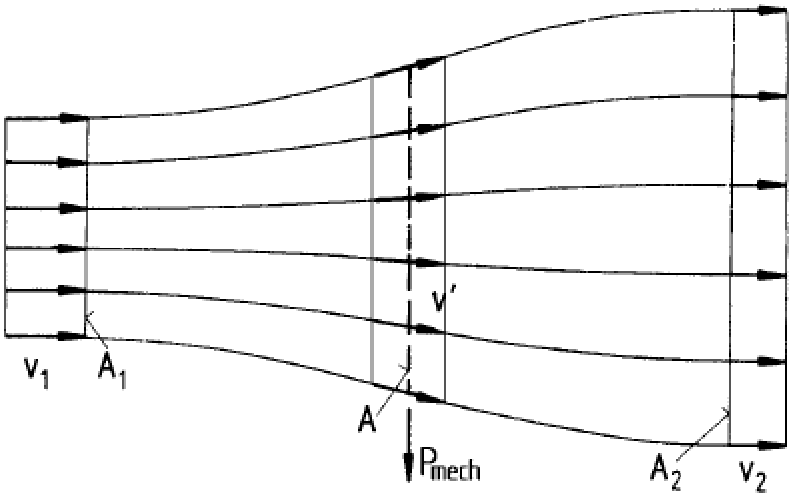

Figure 2.1: Flow conditions for a disk shaped wind convertor

Since the mass flow must be maintained, the continuity equation can be written as equation (2.6)

$$\rho\, v_1\, A_1 = \rho\, v_2\, A_2 \quad (\mathrm{kg/s}) \tag{2.6}$$

So therefore equation (1.5) is rewritten as shown in equation (2.7),

$$P = \frac{1}{2}\dot{m}({v_1}^2 - {v_2}^2) \quad (\mathrm{W}) \tag{2.7}$$

Using equation (2.7) only, the maximum power output would be obtained if v_2 was zero. However, this implies that the flow behind the convertor is stopped and there would be no more flow through the turbine. In order to obtain a physically meaningful result, the maximum extractable power output must be related to the ratio between the outflow and inflow velocities (v_2/v_1).

To do this, another relation must be made to express the power of the convertor by using the law of conservation of momentum.

The force of the air (thrust) exerts on the convertor is shown by equation (2.8):

$$F_{thr} = \dot{m}\,(v_1 - v_2) \quad (\mathrm{N}) \tag{2.8}$$

This thrust is counteracted by equal and opposite force by the convertor on the airflow.

The thrust pushes the airflow at a velocity (v'). The power can be calculated by equation (2.9):

$$P = F_{thr}\, v' = \dot{m}(v_1 - v_2)v' \ \ (W) \qquad (2.9)$$

Therefore the mechanical power can be extracted either from the power difference before and after the convertor or from the thrust and flow velocity. Equating the two equations (2.7) and (2.9) giving equation (2.10), the relationship for the flow velocity v' can be found as equation (2.11):

$$\frac{1}{2}\dot{m}\,({v_1}^2 - {v_2}^2) = \dot{m}(v_1 - v_2)v' \quad (W) \qquad (2.10)$$

$$v' = \frac{v_1 + v_2}{2} \quad (m/s) \qquad (2.11)$$

The mass flow rate for the airstream can be written as equation (2.12):

$$\dot{m} = \rho\, A\, v' = \frac{1}{2}\,\rho\, A\,(v_1 + v_2) \quad (kg/s) \qquad (2.12)$$

The mechanical output power of the convertor can be then written as equation (2.13):

$$P_{mech} = \frac{1}{4}\rho\, A\,({v_1}^2 - {v_2}^2)(v_1 + v_2) \quad (W) \qquad (2.13)$$

The ratio between the mechanical power extracted by the convertor and the available power in the wind is called the power coefficient (C_P) and this can be written as equations (2.14) and (2.15):

$$C_P = \frac{P_{mech}}{P_{air}} = \frac{\frac{1}{4}\rho\, A\,({v_1}^2 - {v_2}^2)(v_1 + v_2)}{\frac{1}{2}\rho\, v^3 A} \qquad (2.14)$$

$$C_P = \frac{P_{mech}}{P_{air}} = \frac{1}{2}\left|1 - \left(\frac{v_2}{v_1}\right)^2\right|\left|1 + \frac{v_2}{v_1}\right| \qquad (2.15)$$

By using this relationship between the power coefficient and the ratio of the air velocities, a graph can be drawn to easily determine the point at which the optimal power extraction occurs as shown in Fig.2.2 [11].

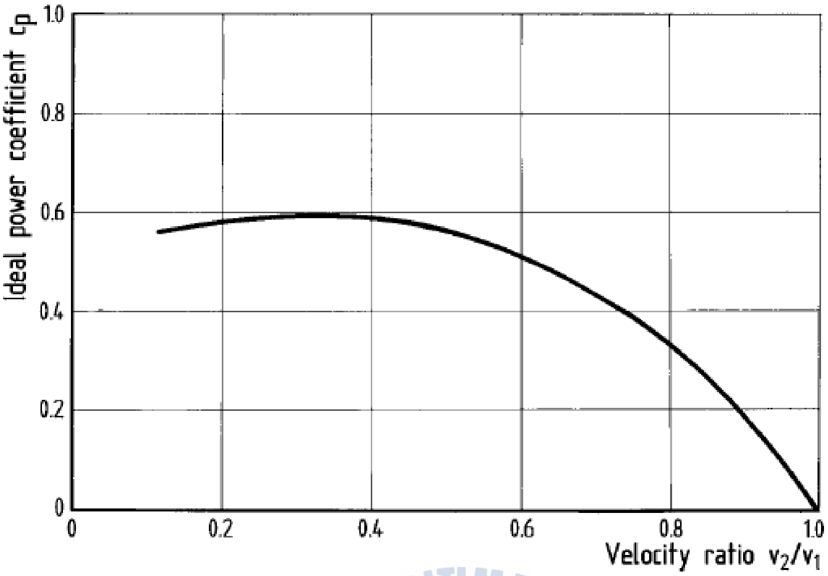

Figure 2.2: The relationship between the power coefficient and the velocity ratio

When $v_2/v_1 = 1/3$, the maximum power coefficient becomes $C_P = 16/27 = 0.593$ [10]. This is called the Betz factor.

These equations describe the conditions for optimal power extraction for an ideal airflow without any losses during conversion.

The flow just before the convertor has to reduce to two thirds of the airstream velocity and behind the convertor the velocity should be a third of the airstream velocity.

Moreover, the maximum possible extractable mechanical work is limited to 59.3% of the power available in the wind.

In reality, the amount extracted is much lower than this due to various factors such as friction and aerodynamic losses.

2.2 Blade element momentum theory

The blade element momentum theory describes the operation of the wind turbine by equating two methods; the momentum balance on a rotating annular stream passing through the turbine and the lift and drag forces generated by the airfoils along the blade.

2.2.1 The momentum theory

To develop the equations for the momentum theory, we consider Fig.2.3, a stream tube with stations 1 to 4. The disc is considered ideal, the flow is frictionless and there is no rotational component in the wake. The velocity far ahead of the disk is (V_1) and far downstream is (V_4). Between stations 2-3, a pressure difference occurs due to energy extraction.

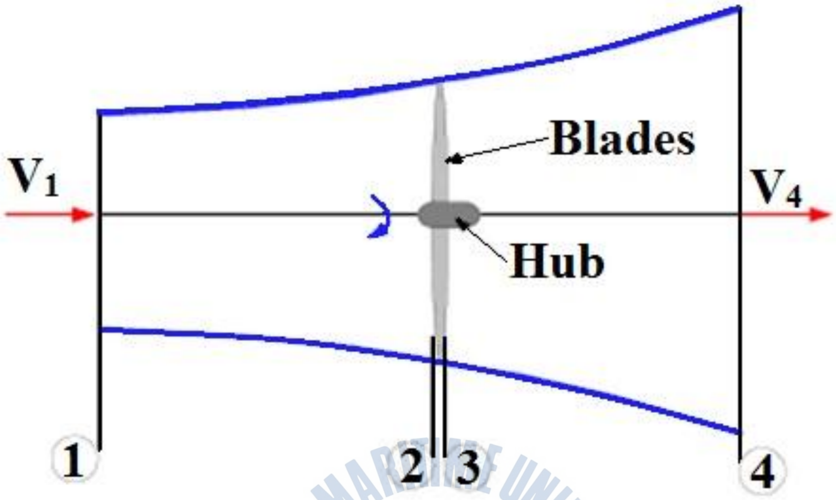

Figure 2.3: The simplified flow with several points for consideration

Applying Bernoulli’s equation:

From station 1 to station 2 yields equation (2.16):

$$P_1 + \frac{1}{2}\rho {V_1}^2 = P_2 + \frac{1}{2}\rho {V_2}^2 \qquad (2.16)$$

From station 2 to station 4 gives equation (2.17)

$$P_2 - \Delta P + \frac{1}{2}\rho\, V^2 = P_0 + \frac{1}{2}\,\rho\, {V_4}^2 \qquad (2.17)$$

Combining equations (2.16) and (2.17) gives the following equation (2.18):

$$\Delta P = \frac{1}{2}\,\rho\left({V_1}^2 - {V_4}^2\right) \qquad (2.18)$$

The thrust resulting from the pressure drop over the area of the disk (A) is shown by equations (2.19) and (2.20):

$$F_{thr} = \Delta PA \tag{2.19}$$

$$F_{thr} = \frac{1}{2}\rho\left(V_1{}^2 - V_4{}^2\right)A \tag{2.20}$$

In addition, the induction factor (a) is defined by equation (2.21):

$$a = \frac{V_1 - V_2}{V_1} \tag{2.21}$$

Using equation (2.21), the velocities V_2 and V_4 can be written as shown by equations (2.22) and (2.23):

$$V_2 = V_1(1 - a) \tag{2.22}$$

$$V_4 = V_1(1 - 2a) \tag{2.23}$$

The thrust force equation can be rewritten as equation (2.24):

$$F_{thr} = \frac{1}{2}\rho V_1{}^2[4a(1 - a)]A \tag{2.24}$$

2.2.2 Rotating wake/ Rotating annular stream tube

In the previous discussions, there was no rotation that affected the flow. In an actual flow, the rotation of the rotor imparts some rotational component to the flow and the wake rotates in the opposite direction of the rotation of the rotor.

Fig.2.4 shows the convertor with a radius of r, rotating with an angular velocity of Ω and the angular velocity of the flow is given by ω. The stream-tube thickness of a small element is dr.

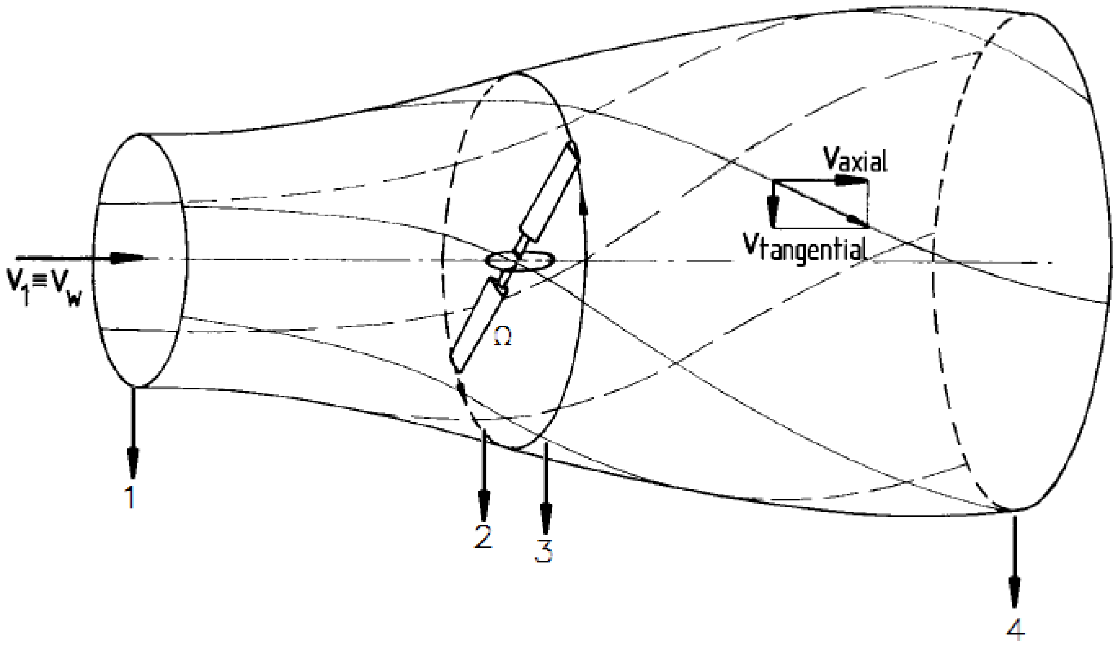

Figure 2.4: The wind turbine in the rotating wake theory

By applying the energy equation across the convertor, the expression for the pressure difference is given by equation (2.25)

$$P_2 - P_3 = \rho\left(\Omega + \frac{1}{2}\omega\right)\omega r^2 \tag{2.25}$$

On an annular element, the thrust is written as equation (2.26):

$$dThr = (P_2 - P_3)\, dA = \left[\rho\left(\Omega + \frac{1}{2}\omega\right)\omega r^2\right] 2\pi r\, dr \tag{2.26}$$

The angular induction factor, a’ written as equation (2.27):

$$a' = \frac{\omega}{2\Omega} \tag{2.27}$$

The tangential force on an annular element can be rewritten as equation (2.28):

$$dTan = 4a'(1 + a')\frac{1}{2}\rho\Omega^2 r^2 2\pi r\, dr \tag{2.28}$$

Or by using the equation (2.22) to give equation (2.29):

$$dF_{Tan} = 4a'(1-a)\rho V_1 \Omega r^3 \pi \, dr \tag{2.29}$$

There is less energy available for extraction by the convertor due to the generation of the rotational energy in the wake.

2.2.3 Blade element theory

The blade element theory analyses the forces at sections of the blade. The theory has two important assumptions that are made:

a) There is no interaction between the different blade sections
b) The lift and drag coefficients of the airfoils on the blade determine the forces on the blade

The blade is divided into N sections and each section will have slightly different flow conditions due to the different air velocities, chord lengths and twist angles as shown in Fig.2.5.

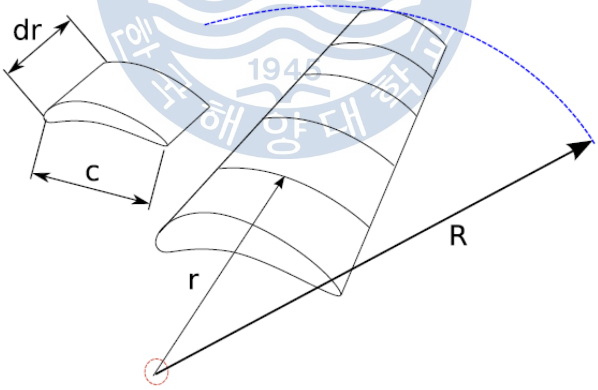

Figure 2.5: The Blade Element Theory analyses forces at N sections of the blade

Fig.2.6 below shows the variables and the relationships between the angles, velocities and forces at the blade.

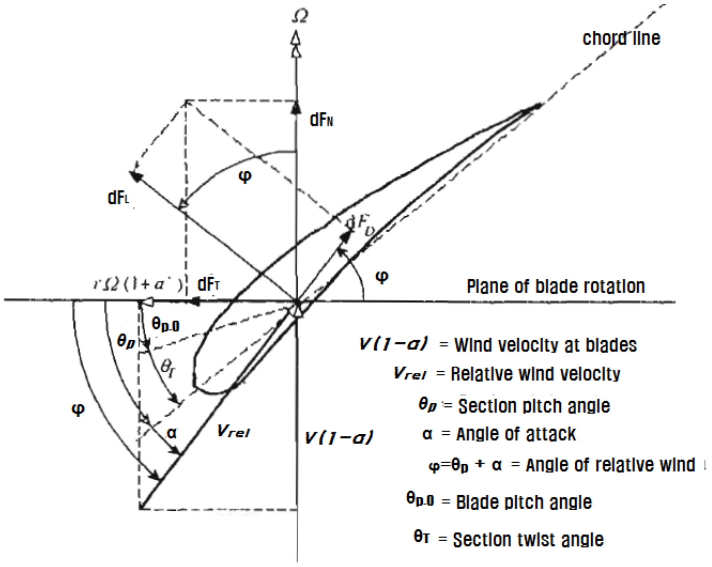

Figure 2.6: Relationships between the flow velocities and forces on an airfoil

The angle between the chord line and the relative wind is the angle of attack (α). The pitch angle of the section (θ_p) is the angle between the angle between the plane of rotation and the chord line. Generally, horizontal axis wind turbine blades are slightly twisted at various sections to ensure optimal flow conditions due to the fact that the blade tip moves faster than the root of the blade. The angle of the relative wind is the addition of the angle of attack and section pitch angle.

The incremental lift force (dF_L) acts normal to the chord and the incremental drag force (dF_D) acts in the direction. The incremental force acting normal to the plane of blade rotation (dF_N) contributes to the thrust. The incremental tangential force in the acting along the plane of blade rotation (dF_T) is the force that creates the torque.

The relative wind speed (V_{rel}) is at an angle φ to the plane of rotation. Using Fig.2.9, the following relationships can be expressed in equation (2.30):

$$\tan\varphi = \frac{V(1-a)}{\Omega r(1+a')} = \frac{1-a}{(1+a')\lambda_r} \tag{2.30}$$

Where the tip speed ratio, λ_r, is given by the equation (2.31):

$$\lambda_r = \frac{\Omega r}{V} \tag{2.31}$$

The relative wind speed relationship with the wind speed is expressed by equation (2.32):

$$V_{rel} = \frac{V(1-a)}{\sin\varphi} \qquad (2.32)$$

The incremental lift and drag forces on a chord length (c) are expressed as equations (2.33) and (2.34) respectively:

$$dF_L = C_l \frac{1}{2} \rho V_{rel}{}^2 c\, dr \qquad (2.33)$$

$$dF_D = C_d \frac{1}{2} \rho V_{rel}{}^2 c\, dr \qquad (2.34)$$

The expressions for the incremental normal and tangential force are given by the equations (2.35) and (2.36):

$$dF_N = dF_L \cos\varphi + dF_D \sin\varphi \qquad (2.35)$$

$$dF_T = dF_L \sin\varphi - dF_D \cos\varphi \qquad (2.36)$$

For a turbine with a blade number B, the incremental thrust is given by equation (2.37):

$$dF_{thr} = B \frac{1}{2} \rho V_{rel}{}^2 (C_l \cos\varphi + C_d \sin\varphi) c\, dr \qquad (2.37)$$

The incremental tangential force acting at a distance, r, from the center gives the expression for differential torque given by equation (1.38).

$$dF_{tor} = B \frac{1}{2} \rho V_{rel}{}^2 (C_l \sin\varphi - C_d \cos\varphi) c\, r\, dr \qquad (2.38)$$

The equation for local solidity is written as shown by equation (2.39):

$$\sigma' = \frac{c\,B}{2\,\pi\,r} \qquad (2.39)$$

Using the equation for relative wind velocity, equation (2.32), and the local solidity, equation (2.39), the thrust and torque at a section is given respectively as equations (2.40) and (2.41):

$$dF_{thr} = \sigma'\pi\rho\frac{V^2(1-a)^2}{\sin^2\varphi}(C_l\cos\varphi + C_d\sin\varphi)dr \tag{2.40}$$

$$dF_{tor} = \sigma'\pi\rho\frac{V^2(1-a)^2}{\sin^2\varphi}(C_l\sin\varphi - C_d\cos\varphi)\,r\,dr \tag{2.41}$$

2.3 Prandtl's tip loss factor

A correction Q is used to account for the blade losses due to blade tip vortices. The equation is written in equation (2.42):

$$Q = \frac{2}{\pi}\cos^{-1}\left(\exp^{-f}\right) \tag{2.42}$$

Where:

$$f = \frac{B}{2}\,\frac{R-r}{r\,\sin\varphi} \tag{2.43}$$

Also the results from $\cos^{-1}$ must be in radians.

Using this factor, the equations for axial and tangential force in equations (2.24) and (2.29) can be re-written into equations (2.44) and (2.45):

$$dF_{Axi} = 4\,\pi\,r\,\rho\,{V_1}^2a(1-a)F\,dr \tag{2.44}$$

$$dF_{Tan} = 4\,\pi\,r^3\rho\,V_1\omega\,(1-a)a'F\,dr \tag{2.45}$$

Using these equations, horizontal axis wind turbine blade geometry can be designed for certain flow conditions.

Using these theories, this study will look at designing a 10kW Horizontal Axis Wind turbine blade and comparing the performance with a Cross Flow type Wind Turbine.

2.4 Design of a horizontal axis wind turbine blade

In order to design a HAWT, selection of several initial design parameters are needed. Using the following formula, the radius of the blade was calculated by equation (2.46):

$$P = C_{Pd}\eta\frac{1}{2}\rho\pi R^2V^3 \tag{2.46}$$

Where P is the power output (10kW), C_{Pd} is the expected power coefficient (0.43), η is the electrical and mechanical efficiency (0.9), V is the velocity of the air (10m/s) and R is the radius of the blade. The radius was calculated to be 3.70m.

The parameters for the design of the turbine are shown in the table below.

Table 2.1: Design Parameters for the HAWT

Rated wind speed	10m/s
RPM	167.76
Rated power	10kW
Stall control type	Passive
Blades	3
Diameter	7.4m

The HAWT will be a passive stall controlled turbine. This means that the blade will undergo stall at speeds over the rated speed. Stall occurs when the flow over the surface of the blade is separated. This reduces the power output of the turbine and in addition, reduces the damage to the turbine that might occur at higher speeds [12].

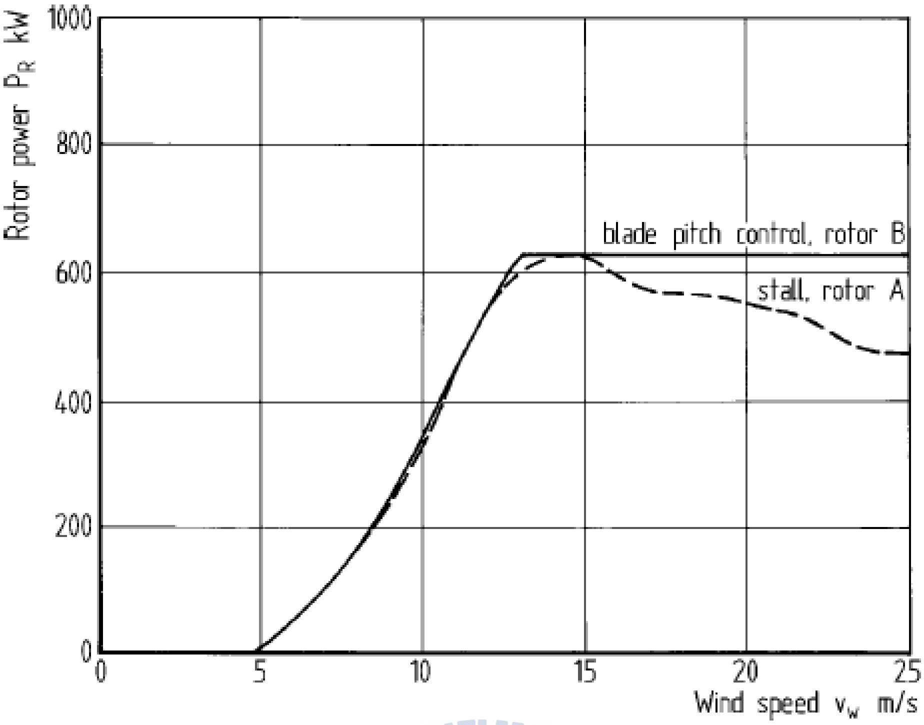

Figure 2.7: Power versus wind speed curve for two types of power control methods

Fig.2.7 shows the power output versus wind speed for two turbines using two different power control methods. The advantage that stall controlled rotors have is that they have few moving parts in the turbine which reduces maintenance.

For the blade geometry of a HAWT, the airfoil sections are important in producing the necessary forces to convert the kinetic energy of the wind into mechanical energy. There several factors to consider before selecting certain airfoils for HAWTs.

One of these is the thickness of the rotor blade. Generally, thinner rotor blades allow the use of high performance airfoils enabling more energy to be converted and increase the wind rotor power coefficient. However, thinner blades have reduced strength and stiffness. Thicker airfoils increase the thickness of the blade and provide more strength but have lower aerodynamic performance characteristics [13].

Another factor is the roughness sensitivity of an airfoil. Wind turbines get contaminated with dirt/insects/ice during operation. The contamination often reduces the aerodynamic performance of the airfoils and the turbine. The low roughness sensitivity is needed to ensure that the airfoils do not suffer a large amount of derogation in aerodynamic performance due to dirt accumulation on the blade. Using certain airfoils that have low sensitivity to the contamination is therefore important. Once the airfoils are selected, the performance of a turbine can be predicted.

In addition, since the blade of the wind turbine experiences different flow conditions over the blade geometry, airfoils that are selected to be used in blade must fulfill certain conditions ensure that gives the turbine optimum performance in most conditions.

Some of the factors that are needed to be considered depend on which section of the blade the airfoil is located.

As shown in Fig.2.8, from 12% to 40% of a turbine blade, thick airfoils of about 30-40% thickness are needed to provide more structural stability rather than aerodynamic performance [14, 15].

From 40-60% of a blade, airfoils of about 25% thickness are needed, provided that the airfoils also have low roughness sensitivity [14, 15].

At 60% to 100% of the blade geometry, the aerodynamic performance is important as most of the power produced comes from this section. Low thickness (from 18%-25%) airfoils with large lift to drag ratios are used. Also, the maximum lift coefficient (C_L) of the airfoil should around 1.2-1.4 to avoid sudden fluctuations in loading when gusts occur. Moreover, airfoils used in this region should display lift curves that do not have sharp drops in C_L value past the stall angle [14, 15].

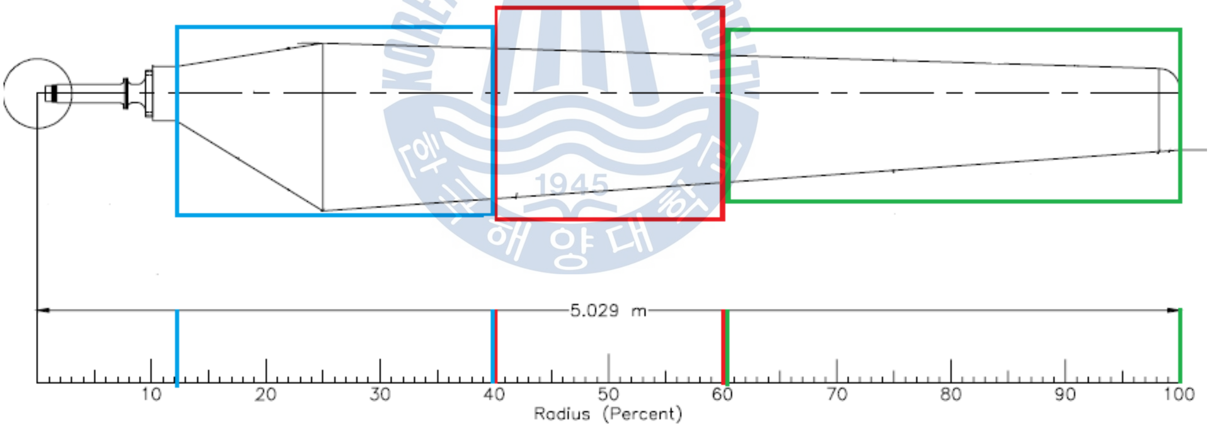

Figure 2.8: Top view of a HAWT blade span with the highlighted areas indicating the regions for various airfoils

Several airfoils were initially selected and the performance curves were taken from literature.

The selected airfoils were DU-W-300, DU 91-W2-250, S819, Risø-A1-24, SG6043_Eppler422 and DU-96-W-180.

By using the blade element and momentum theories, the 2D lift and drag coefficients of the airfoil can be used to predict the performance and power output of a wind turbine.

The BEMT-based in house code POSEIDON [16] was used to predict the performance of several geometries of the blade before selecting the most suitable one. It was found that the most suitable airfoils for design were the DU-W-300, DU 91-W2-250 and DU-96-W-180 airfoils. These 3 airfoils were placed in the 12-40%, 40-60% and 60-100% of the blade length respectively as shown in the previous figure.

The chord length and twist distribution of the turbine is given below in Fig.2.9 to Fig.2.10.

The chord length formula, shown as equation (2.47), was suggested by Grant Ingram [17]:

$$\mathrm{C} = \frac{8\pi r \cos\beta}{3B\lambda_r} \tag{2.47}$$

Where C is the chord length at a section, β relative angle of the flow to the section, B is the number of blades and λ_r is the local speed ratio of the section.

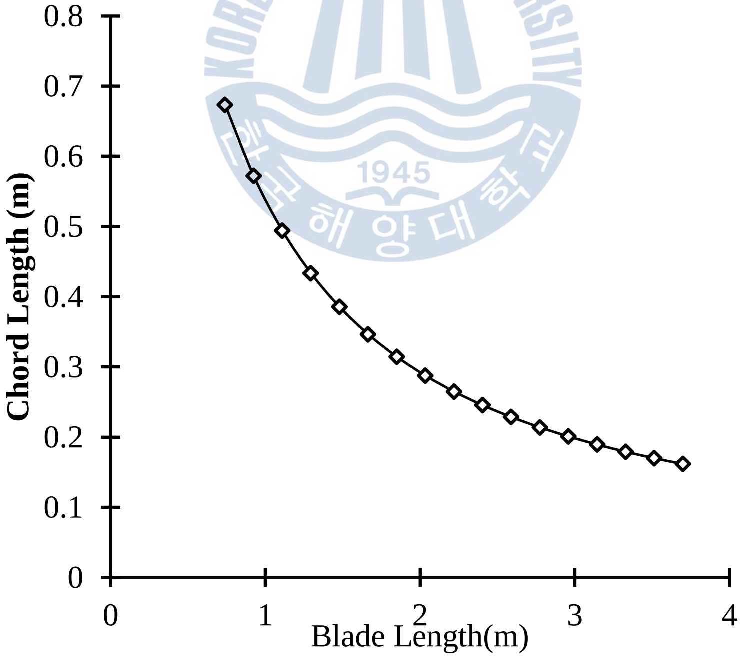

Figure 2.9: Chord distribution of the airfoil along the blade span

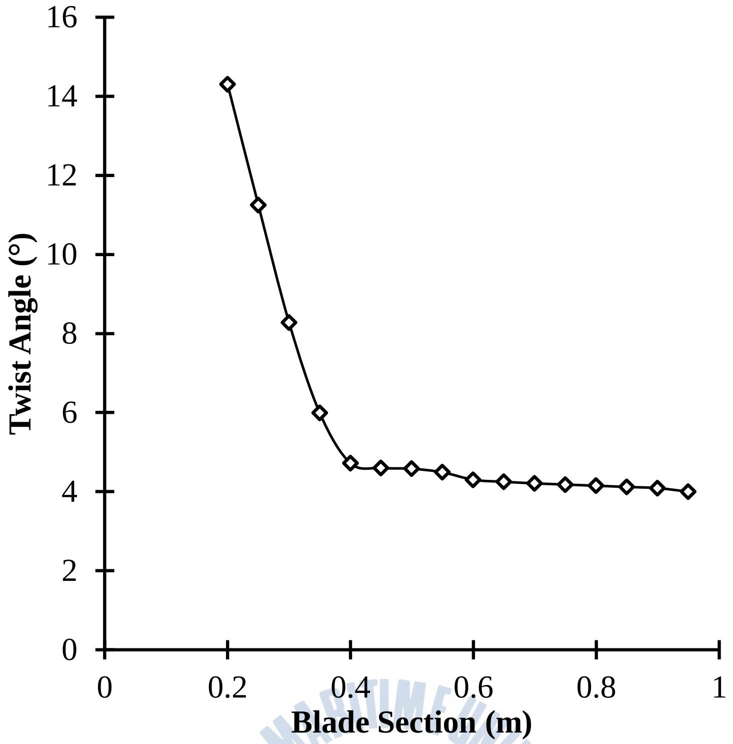

Figure 2.10: The twist distribution of the airfoils on the HAWT

The twist angle was configured in POSEIDON. The twist angles form 40% of the blade section was twisted so that the coefficient of lift produced at 10m/s was close to the maximum coefficient of lift value.

The blade was then modeled in NX 5.0 and analyzed in commercial CFD software, CFX 13.

2.5 Cross flow type wind turbine

Cross flow type turbines have been used primarily in hydropower applications. These types of turbines are simple to manufacture and can operate over a wide range of flow rates quite efficiently.

Cross flow type turbines have been studied in the past for possible applications in wind power. One advantage that the cross flow type has over the conventional type of turbines is that the noise emission is low or negligible. However, cross flow type turbines have a low efficiency compared to that of conventional turbines (C_P = 0.1 compared to 0.4 for most modern day HAWTs) and are therefore generally not economically feasible [18].

Previous studies done by Shigetmitsu et al [19] and Kishinami et al [20] looked at two different ways to increase the power output.

Shigetmitsu used symmetrical casings to influence the flow around the turbine and obtained a maximum C_P of 0.19 whereas Kishinami installed guide vanes that increased the power output up to a C_P value of 0.2.

This study will look at the effect of using a nozzle and diffuser on a cross flow type wind Turbine. The performance characteristics of the cross flow type wind turbine will compared to the HAWT.

The next chapter will describe the modeling of the two turbines and the method used to analyze them.

Chapter 3 Methodology

This section discusses the method numerical modeling, the design of the horizontal axis wind turbine and cross flow turbine and well as the various geometric configurations used for the investigation.

3.1 Numerical modeling

This study involves the use of Computational Fluid Dynamics (CFD) which is a computer-based tool that is widely used for analysis and design purposes. By utilizing the advances in computing power and graphics, creation and analysis of a certain model is much less labor intensive and cheaper than experimental methods.

ANSYS CFX solves the unsteady Navier-Stokes equations in their conservation form [20]. The instantaneous equation of mass (continuity) in the stationary frame is expressed as equation (3.1):

$$\frac{\partial \rho}{\delta t} + \nabla \cdot (\rho U) = 0 \qquad (3.1)$$

And the instantaneous equation for momentum is expressed as shown in equation (3.2):

$$\frac{\partial \rho}{\delta t} + \nabla \cdot (\rho \boldsymbol{U} \otimes \boldsymbol{U}) = -\nabla p + \nabla \cdot \tau + S_M \qquad (3.2)$$

Where τ is the stress tensor.

These instantaneous equations are averaged for turbulent flows leading to additional terms that need to be solved. While the Navier-Stokes equations describe both laminar and turbulent flows without addition terms, realistic flows involve length scales much smaller than the smallest finite volume mesh. A Direct Numerical Simulation of these flows would require significantly more computing power than what is available now or in the future.

Therefore, much research has been done to predict the effects of turbulence by using turbulence models. These models account for the effects of turbulence without the use of a very fine mesh or direct numerical simulation.

These turbulence models modify the transport equations by adding averaged and fluctuating components. The transport equations are changed to equations (3.3) and (3.4):

$$\frac{\partial \rho}{\delta t} + \nabla \cdot (\rho U) = 0 \qquad (3.3)$$

$$\frac{\partial \rho U}{\partial t} + \nabla \cdot \{\rho\, \boldsymbol{U} \otimes \boldsymbol{U}\} = -\nabla p + \nabla \cdot \left\{\tau - \rho \overline{\boldsymbol{u} \otimes \boldsymbol{u}}\right\} + \boldsymbol{S}_M \qquad (3.4)$$

The mass equation is not changed but the momentum equation contains extra terms which are the Reynolds stresses, ρ $\overline{\boldsymbol{u} \otimes \boldsymbol{u}}$ and the Reynolds flux, ρ $\overline{\boldsymbol{u}\, \phi}$. These Reynolds stresses need to be modeled by additional equations to obtain closure. Obtaining closure implies that there are a sufficient number of equations to solve for all the unknowns including the Reynolds stresses and Reynolds fluxes.

Various turbulence models provide various ways to obtain closure. In this investigation, the model utilized was the Shear Stress Transport (SST) model. The advantage of using this model is that combines the advantages of other turbulence models (the k-ε, Wilcox k-ω and BSL k-ω). In order to understand the advantage the SST model gives, the 3 other turbulence models will be discussed briefly.

3.2 Turbulence models

3.2.1 Two equation turbulence models

Two-equation turbulence models are widely used in CFD as they give a good compromise between computational power needed and accuracy. The term ‘two equation’ refers to the fact that these models solve for the velocity and length scales using separate transport equations. The turbulence velocity scale is obtained by solving the transport equation. The turbulent length scale is estimated from two properties of the turbulence field, namely the turbulent kinetic energy and the dissipation rate. The dissipation rate of the kinetic energy is obtained from its transport equation. The most widely used are the the k-ε and k-ω two equation models. In the next section, the k-ε, Wilcox k-ω, BSL k-ω and SST models will be briefly discussed. More details on the models are in reference [22].

3.2.1.1 k-ε Turbulence model

The k-ε model introduces k (m^2/s^2) as the turbulence kinetic energy and ε (m^2/s^3) as the turbulence eddy dissipation. The continuity equation remains the same:

$$\frac{\partial \rho}{\partial t} + \nabla \cdot (\rho\, \boldsymbol{U}) = 0 \qquad (3.4)$$

The momentum equation changes, as shown by equation (3.5):

$$\frac{\delta \rho \boldsymbol{U}}{\delta t} + \nabla \cdot (\rho \boldsymbol{U} \otimes \boldsymbol{U}) = -\nabla p' + \nabla \cdot \left(\mu_{eff}(\nabla \boldsymbol{U} + (\nabla \boldsymbol{U})^T)\right) + S_M \qquad (3.5)$$

Where S_M is the sum of body forces, μ_{eff} is the effective viscosity accounting for turbulence and p’ is the modified pressure. The k-ε model uses the concept of eddy viscosity giving the equation for effective viscosity as shown by equation (3.6):

$$\mu_{eff} = \mu + \mu_t \qquad (3.6)$$

μ_t is the turbulence viscosity is linked to the turbulence kinetic energy and dissipation by the equation (3.7):

$$\mu_t = C_\mu \rho \frac{k^2}{\varepsilon} \tag{3.7}$$

Where C_μ is a constant.

The values for k and ε come from the differential transport equations for the turbulence kinetic energy and the turbulence dissipation rate.

The turbulence kinetic energy equation is given as equation (3.8):

$$\frac{\partial(\rho k)}{\partial t} + \nabla \cdot (\rho \boldsymbol{U} k) = \nabla \cdot \left[\left(\mu + \frac{\mu_t}{\sigma_k}\right) \nabla k\right] + P_k + P_{kb} - \rho\varepsilon \tag{3.8}$$

The turbulence dissipation rate is given by equation (3.9):

$$\frac{\partial(\rho \varepsilon)}{\partial t} + \nabla \cdot (\rho \boldsymbol{U} \varepsilon) = \nabla \cdot \left[\left(\mu + \frac{\mu_t}{\sigma_\varepsilon}\right) \nabla \varepsilon\right] + \frac{\varepsilon}{k}(C_{\varepsilon 1}(P_k + P_{\varepsilon b}) - C_{\varepsilon 2}\rho\varepsilon) \tag{3.9}$$

Where $C_{\varepsilon 1}$, $C_{\varepsilon 2}$, σ_k, σ_ε are constants.

Pk is the turbulence production due to viscous forces and is modeled by the equation (3.10):

$$P_k = \mu_t \nabla \boldsymbol{U} \cdot (\nabla \boldsymbol{U} + \nabla \boldsymbol{U}^T) - \frac{2}{3} \nabla \cdot \boldsymbol{U}(3\mu_t \nabla \cdot \boldsymbol{U} + \rho k) \tag{3.10}$$

A buoyancy term may be added to the previous equation if the full buoyancy model is used. However, it this option is not used in this study.

3.2.1.2 Wilcox k-ω turbulence model

This model has an advantage over the k-ε model, where it does not involve complex linear damping functions for near wall calculations at low Reynolds numbers.

The k-ω model assumes that the turbulence viscosity is related to the turbulence kinetic energy, k, and the turbulent frequency, ω, by the equation (3.11):

$$\mu_t = \rho \frac{k}{\omega} \tag{3.11}$$

The transport equation for k is given by the equation (3.12):

$$\frac{\partial(\rho k)}{\partial t} + \nabla \cdot (\rho \boldsymbol{U} k) = \nabla \cdot \left[\left(\mu + \frac{\mu_t}{\sigma_k}\right) \nabla k\right] + P_k + P_{kb} - \beta' \rho\, k\, \omega \tag{3.12}$$

The transport equation for ω is shown as equation (3.13):

$$\frac{\partial(\rho \omega)}{\delta t} + \nabla \cdot (\rho\, \boldsymbol{U}\, \omega) = \nabla \cdot \left[\left(\mu + \frac{\mu_t}{\mu_\omega}\right) \nabla \omega\right] + \alpha \frac{\omega}{k} P_k + P_{\omega b} - \beta\, \rho\, \omega^2 \tag{3.13}$$

The production rate of turbulence (P_k) is calculated as shown previously in the k-ε section.

The model constants are given by equations (3.14) to (3.19):

$$\beta' = 0.09 \tag{3.14}$$

$$\alpha = {}^{5}/_{9} \tag{3.15}$$

$$\beta = 0.075 \tag{3.16}$$

$$\sigma_k = 2 \tag{3.17}$$

$$\sigma_\omega = 2 \tag{3.18}$$

The Reynolds stress tensor, ρ $\overline{\boldsymbol{u} \otimes \boldsymbol{u}}$, is calculated by:

$$-\rho\, \overline{\boldsymbol{u} \otimes \boldsymbol{u}} = \mu_t(\nabla \boldsymbol{U} + (\nabla \boldsymbol{U})^T) - \frac{2}{3}\partial(\rho k + \mu_t \nabla \cdot \boldsymbol{U}) \tag{3.19}$$

3.2.1.3 Shear stress transport model

The disadvantage of the Wilcox model is the strong sensitivity to free-stream conditions. Therefore a blending of the k-ω model near the surface and the k-ε in the outer region was made by Menter [23] which resulted in the formulation of the BSL k-ω turbulence model. It consists of a transformation of the k-ε model to a k-ω formulation and subsequently adding the resulting equations. The Wilcox model is multiplied by a blending function F_1 and the transformed k-ε by another function $1\text{-}F_1$. F_1 is a function of wall distance (being the value of one near the surface and zero outside the boundary layer). Outside the boundary and on the edge of the boundary layer, the standard k-ε model is used [22].

However, while the BSL k-ω model combines the advantages of both the k-ε and Wilcox k-ω turbulence models, it fails to properly predict the onset and amount of flow separation from smooth surfaces. The k-ε and Wilcox k-ω turbulence models do not account for the transport of the turbulent shear stress resulting in an over-prediction of eddy-viscosity. A limiter on the formulation can be used to obtain the proper results. These limiters are given by equation (3.20):

$$v_t = \frac{a_1 k}{\max(a_1 \omega, S\, F_2)} \tag{3.20}$$

Where

$$v_t = \frac{\mu_t}{\rho} \tag{3.21}$$

F_2 is a blending function which restricts the limiter to the wall boundary and S is the invariant measure of the strain rate.

The blending functions are given by the equations (3.22) to (3.23):

$$F_1 = \tanh({arg_1}^4) \tag{3.22}$$

$$arg_1 = min\left(max\left(\frac{\sqrt{k}}{\beta' \omega y}, \frac{500\, v}{y^2 \omega}\right), \frac{4\rho k}{C\, D_{kw} \sigma_{\omega 2} y^2}\right) \tag{3.23}$$

y is the distance to the nearest wall and v is the kinematic viscosity. In addition:

$$\mathrm{C}\,D_{k\omega} = max\left(2\rho\frac{1}{\sigma_{\omega 2}\omega}\nabla k\nabla\omega, 1.0\times 10^{-10}\right) \tag{3.24}$$

$$F_2 = \tanh(arg_2{}^2) \tag{3.25}$$

$$arg_2 = max\left(\frac{2\sqrt{k}}{\beta'\omega\, y}, \frac{500v}{y^2\omega}\right) \tag{3.26}$$

To perform a simulation using CFD, the primary steps taken are:

a) Creation of the geometry
b) Generating the mesh of the geometry
c) Define the physics of the model
d) Solving the model
e) Process and Analyse the results of the simulation

These steps will be further discussed in the sections below.

3.3 Creating the geometry

The three dimensional models of the geometry for the horizontal axis wind turbine and cross flow turbine were made using the commercial computer aided drawing software, Uni-graphics NX 5.0.

3.3.1 Model of horizontal axis wind turbine (HAWT)

The geometry of the blade in Fig.3.1 was made using NX 5.0 software using the information previously calculated in Fig.1.12 to Fig.1.13.

Figure 3.1: Cross sections of the horizontal axis wind turbine

Near the trailing edge of the airfoils (approx. 0.99C), the sharp trailing edge was modified into a blunt trailing edge in order to avoid bad mesh generation near this area.

3.3.2 Model of the cross flow turbine

The cross flow turbine geometry was constructed in NX 5.0. The dimensions of the turbine blade were taken from a study done by Kipyoung et el [24]. The turbine has 30 blades and had an inlet angle of 30° and blade outlet angle of 90°. The model of this turbine is shown in Fig.3.2.

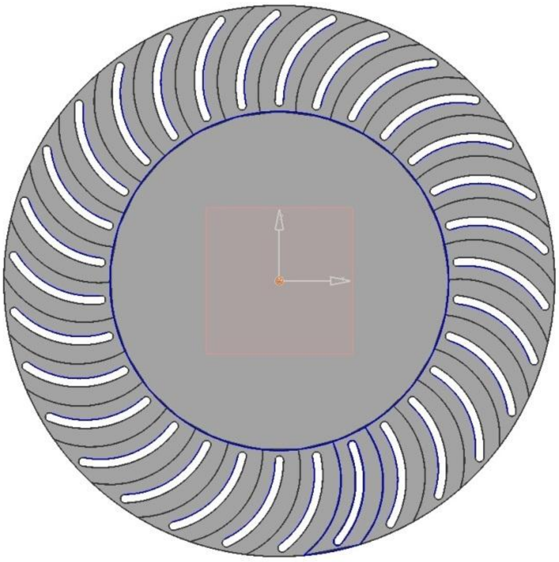

Figure 3.2: Cross flow turbine

For comparison purposes, the swept area of the HAWT is made equal to the inlet area of the nozzle for the cross flow type turbine to ensure the power to area ratio was the same for both turbines. The cross flow turbine inlet dimensions are shown in Fig.3.3 below.

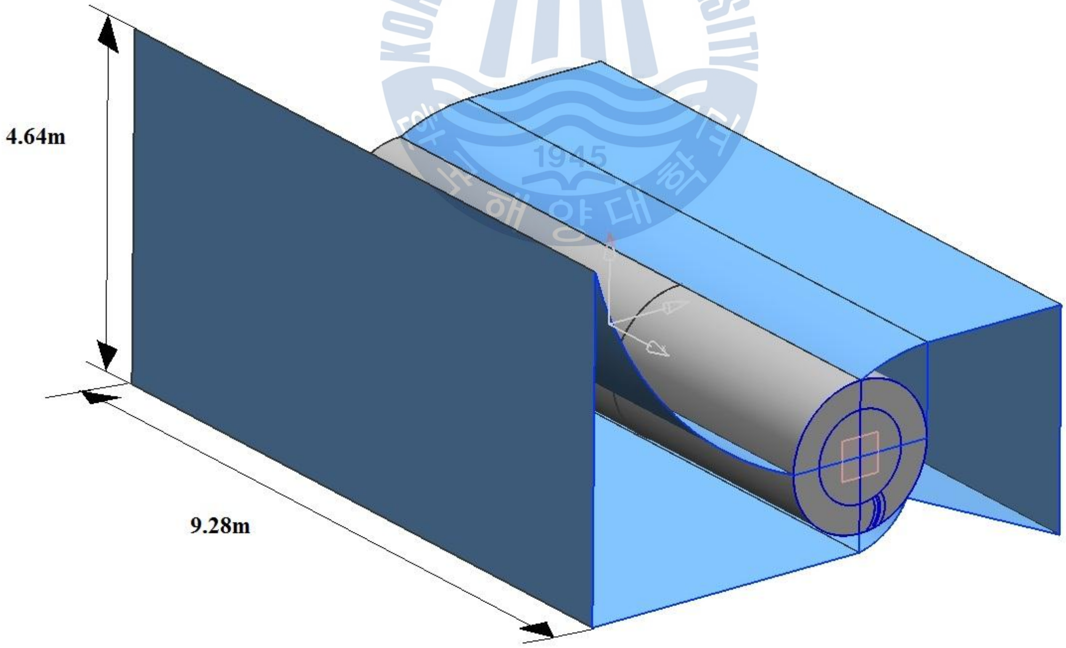

Figure 3.3: Overall geometry of the cross flow turbine with the nozzle and turbine

The blade length spanned the entire width of the turbine and the outer radius of the turbine was 1m while the inner radius was 0.615m. The distance from the inlet to the center of the turbine was 4m.

3.3.2.1 Cross flow turbine nozzle analysis: Method and geometry

To analyze the effect of the nozzle on the performance of the cross flow turbine, two geometric factors were looked at. These two factors were the entry arc angle and the shape of the nozzle walls.

3.3.2.1.1 Analysis by turbine entry arc angle

The entry arc is the angle of the arc made by the intersection top and bottom walls of the nozzle with the outer diameter of the turbine as shown by the angle δ in Fig.345 below.

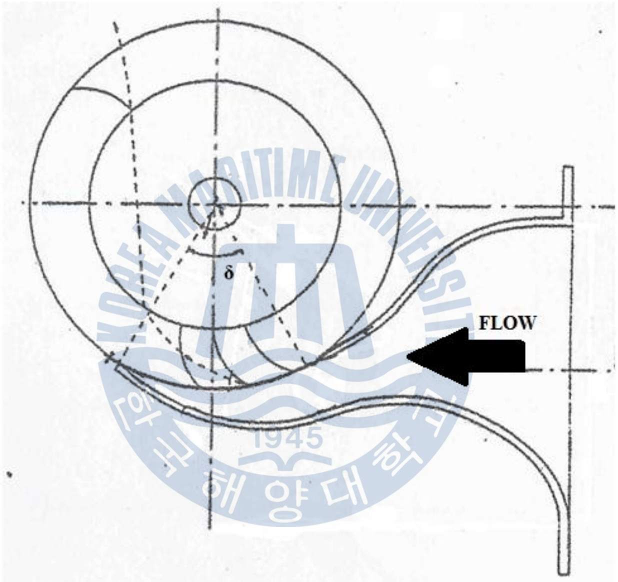

Figure 3.4: The Turbine Entry Arc angle δ

This angle was varied from 30° to 135° and the geometry of the 4 cases is presented from Fig.3.5 to Fig.3.8 below.

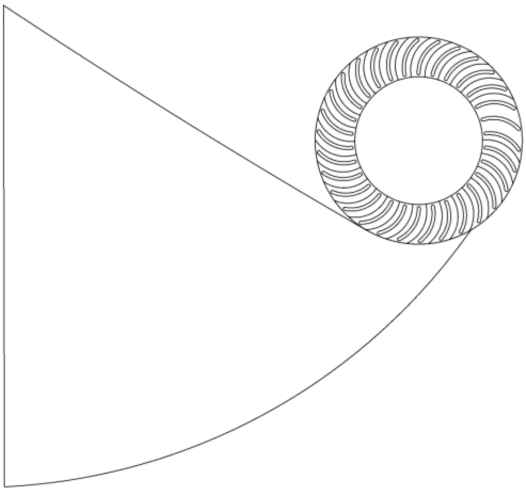

Figure 3.5: Entry arc angle 30° case

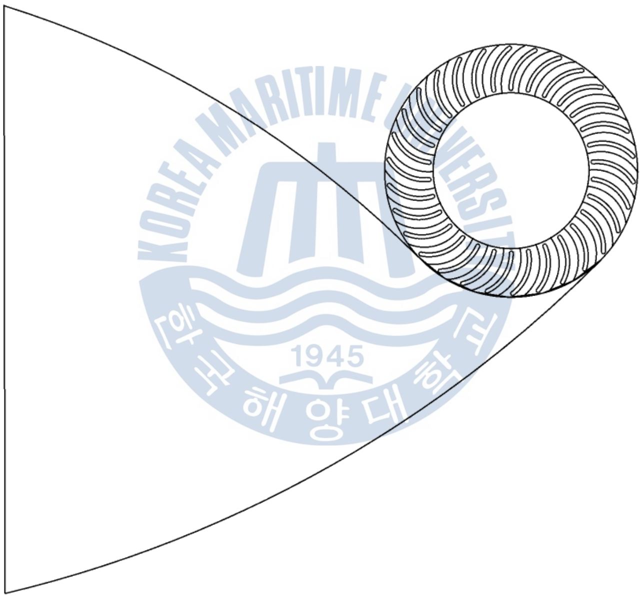

Figure 3.6: Entry arc angle 90°

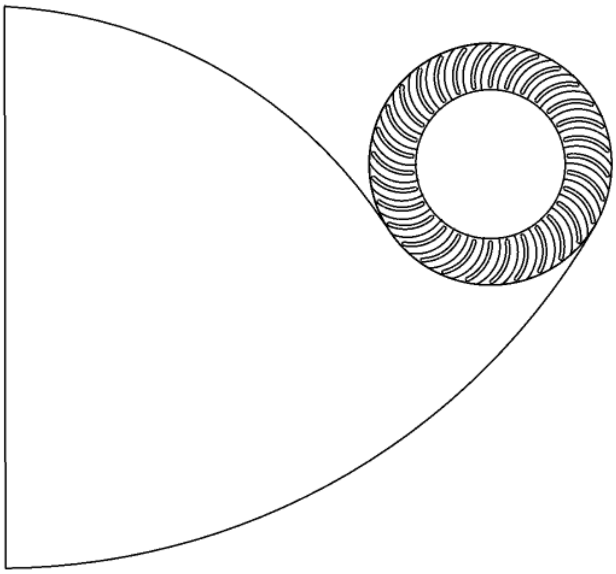

Figure 3.7: Entry arc angle 120°

Figure 3.8: Entry arc angle 135°

After the analysis on the entry arc angle was done, the shape of the nozzle wall was investigated.

3.3.2.1.2 Analysis by Nozzle shape

For this analysis the walls of the nozzle was varied as shown from Fig.3.9 to Fig.3.14. There were a total of six nozzle shapes used for analysis. All dimensions shown are in millimeters (mm).

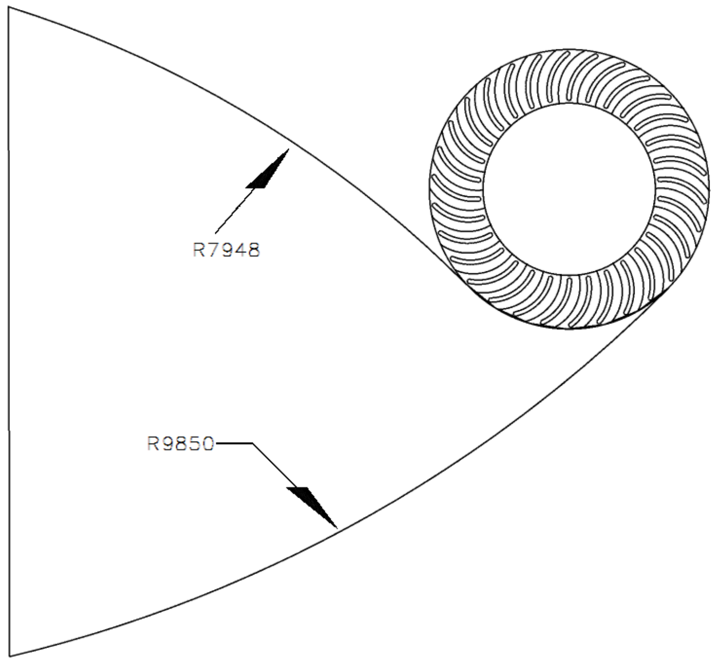

Figure 3.9: Nozzle analysis: Case 1

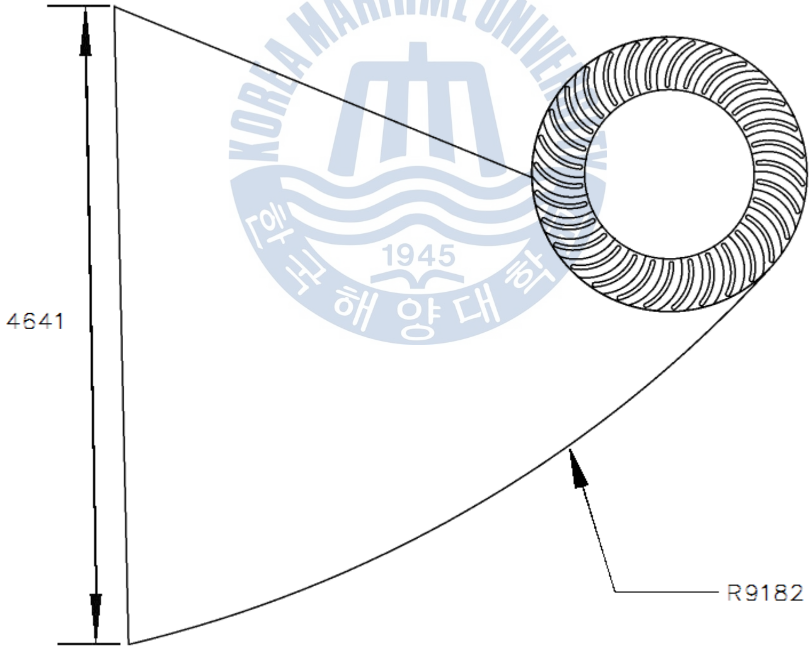

Figure 3.10: Nozzle analysis: Case 2

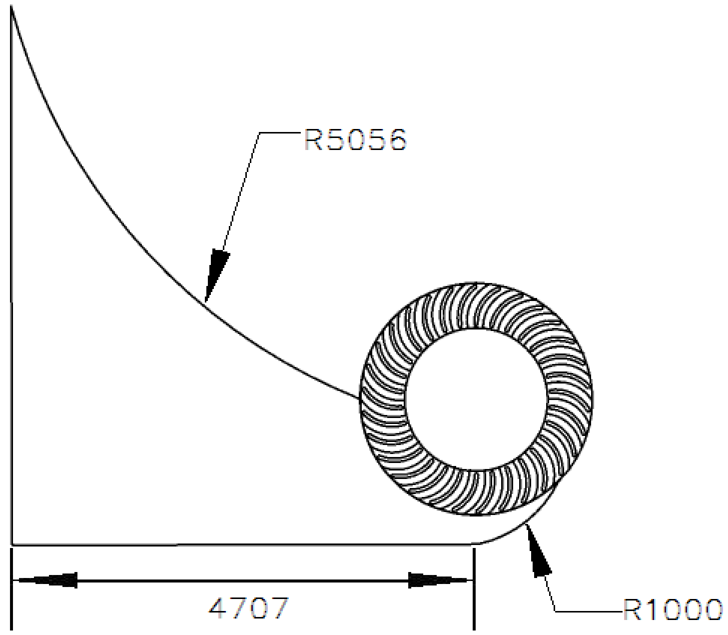

Figure 3.11: Nozzle analysis: Case 3

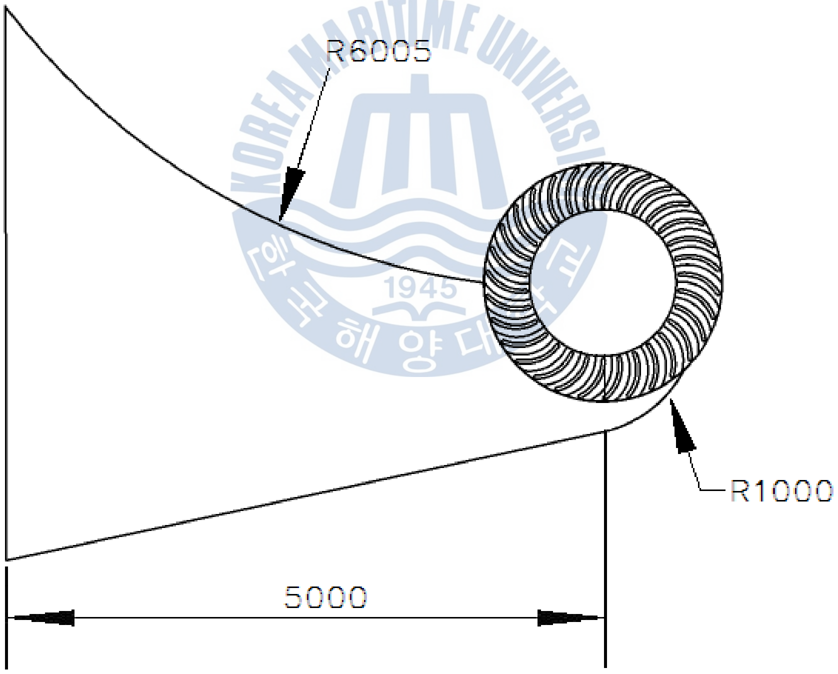

Figure 3.12: Nozzle analysis: Case 4

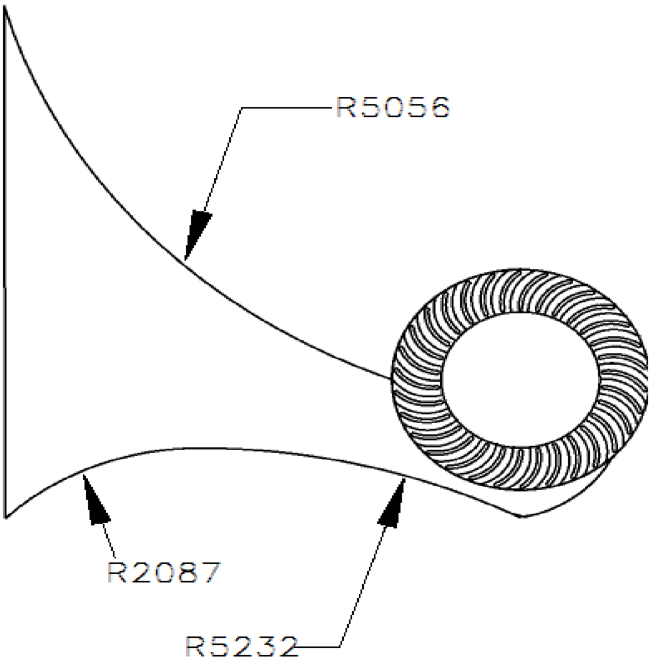

Figure 3.13: Nozzle analysis: Case 5

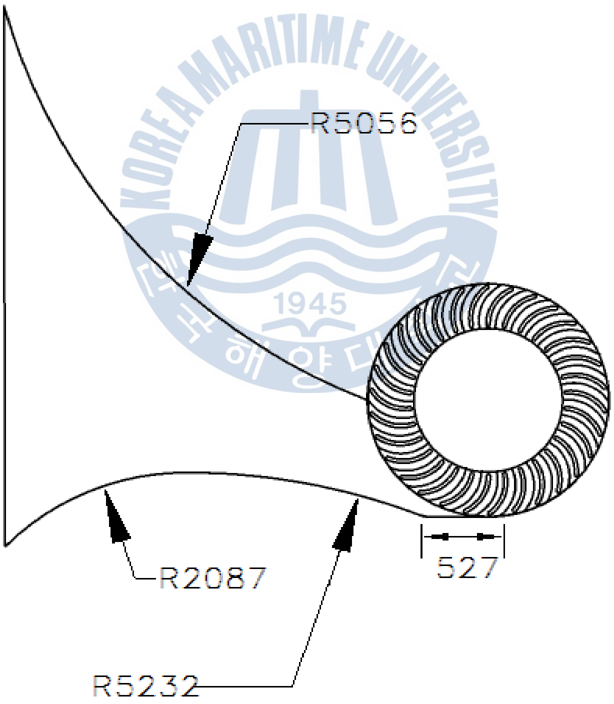

Figure 3.14: Nozzle analysis: Case 6

After the conclusion of the analysis of the nozzle geometries, the nozzle that gave the highest power output utilizing the results of the previous analysis was selected and was used as the default nozzle for subsequent simulations of the effect of the diffuser. The effect of the diffuser geometry was studied in two parts. The first analysis was the effect of the diffuser entry arc followed by a second analysis which investigated the effect of different diffuser shapes on the performance characteristics of the turbine.

3.3.2.1.3 Diffuser Entry Arc

In similar manner to the turbine entry arc angle, the diffuser arc angle is the angle of the arc made by the intersection of the top and bottom walls of the diffuser with the outer diameter of the turbine shown in Fig.3.15 as δ_2.

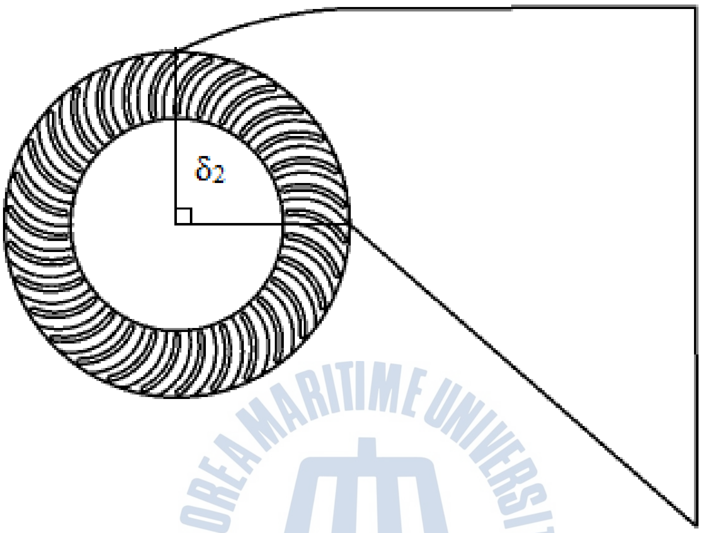

Figure 3.15: Diffuser entry angle 90°

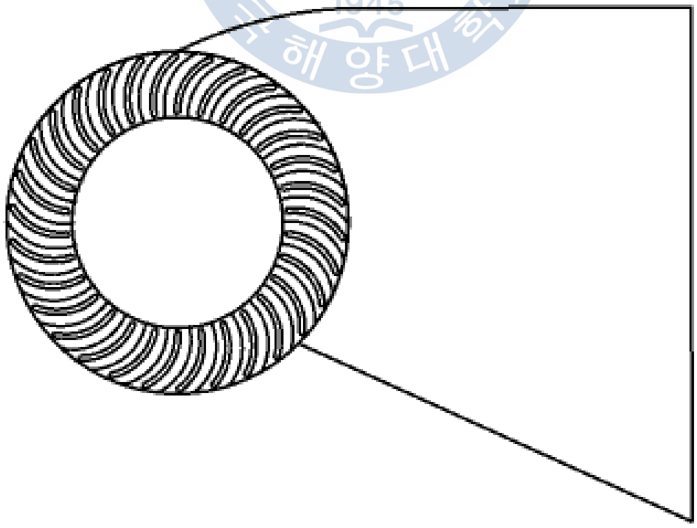

Figure 3.16: Diffuser entry arc Angle 135°

Once this investigation was completed, the effect of the geometry of the shape of the diffuser on the performance of the turbine was investigated.

3.3.2.1.4 Diffuser shape analysis

For this analysis, the geometry of the diffuser was varied. The 4 different cases are shown below in Fig.3.17 to Fig.3.20.

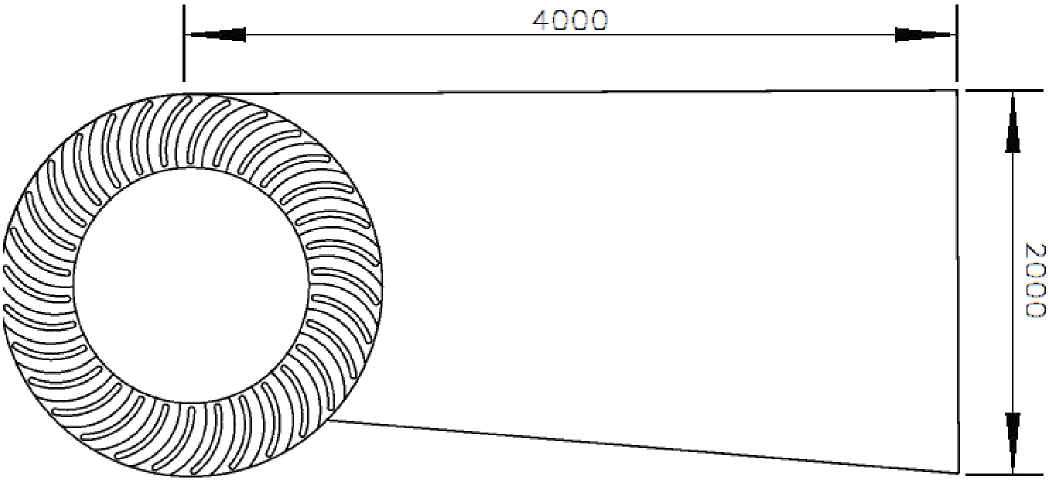

Figure 3.17: Diffuser analysis: Case 1

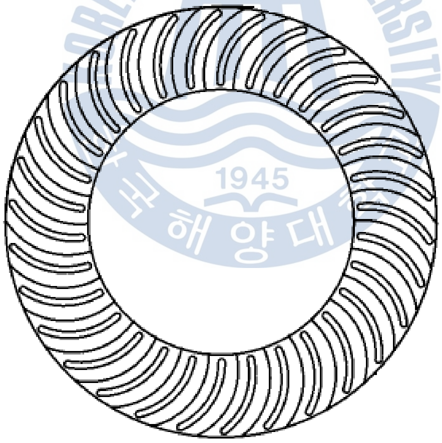

Figure 3.18: Diffuser analysis: Case 2

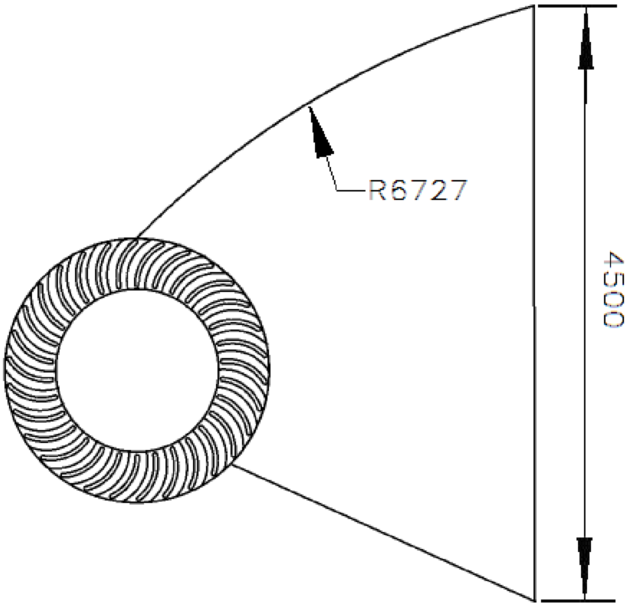

Figure 3.19: Diffuser analysis: Case 3

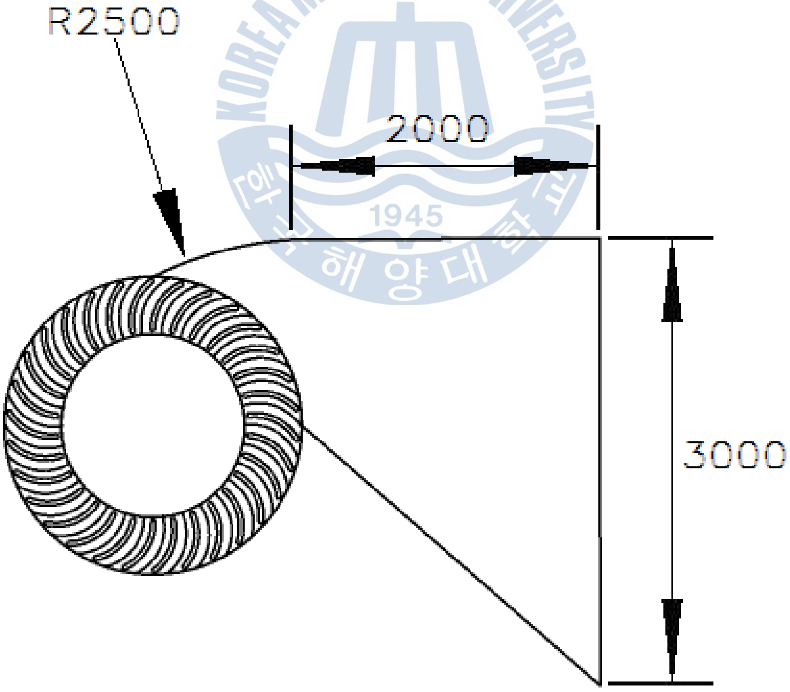

Figure 3.20: Diffuser analysis: Case 4

After the geometries were all created, the mesh of the geometries for numerical modeling was generated.

3.4 Mesh generation

Mesh generation refers to the creation of a numerical domain over a certain geometry in which the computer can use to solve the required equations. After the completion of the geometry, a number of computer based software may be used to generate the numerical domain. In this study, ICEM CFD was used to generate the mesh of the two wind turbines and output the required file for the solver.

ICEM CFD allows for the generation of several types of meshes including tetrahedral, hexahedral or even hybrid meshes. Tetrahedral meshes are generally less time consuming to build whereas hexahedral meshes provide more accurate results provided that the mesh quality is high.

In addition to this, ICEM CFD allows for the generation of structured or unstructured meshes. Structured meshes have cells that are regular in shape and each grid point is uniquely identified by indices and coordinates. Unstructured meshes contain cells that are not necessarily regular in shape and have grid points in no particular ordering. The main advantage of unstructured meshes is the flexibility it provides in the generation of a computational grid in complex geometries.

The computational grid of all the geometries in this investigation was made of unstructured hexahedral volumes to ensure accurate results.

3.4.1 Horizontal axis wind turbine mesh

The mesh of the HAWT blade is given in Fig.3.21. Only one blade is modeled in a 120° angled domain. The remaining blades are accounted for by using periodic conditions. This method saves computational power by reducing the complexity of the mesh and retains accuracy of the simulation. The distance from the inlet to the blade is about 29.6m and the distance from the blade to the outlet is 37m. The domain is 14.8m in width.

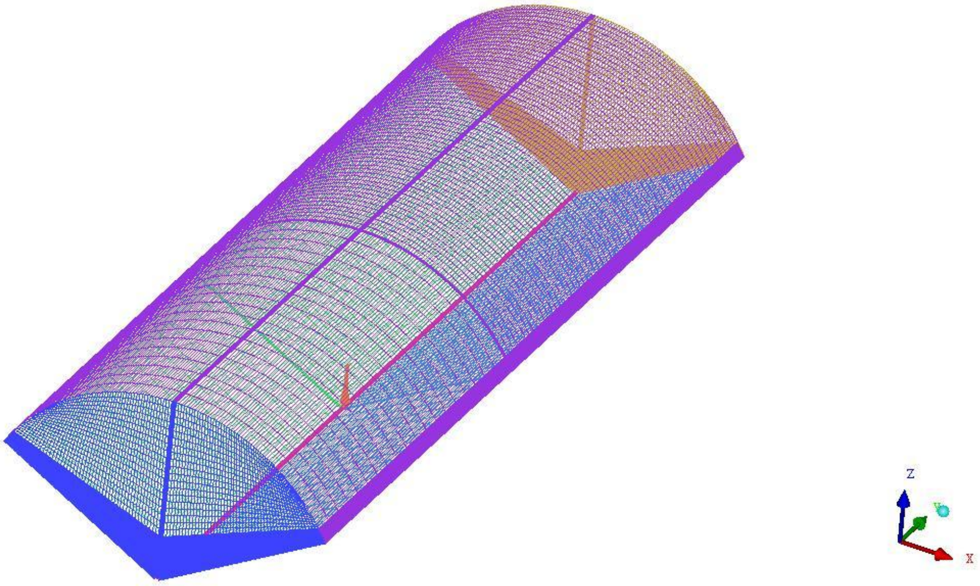

Figure 3.21: Computational Grid of the domain for the wind turbine

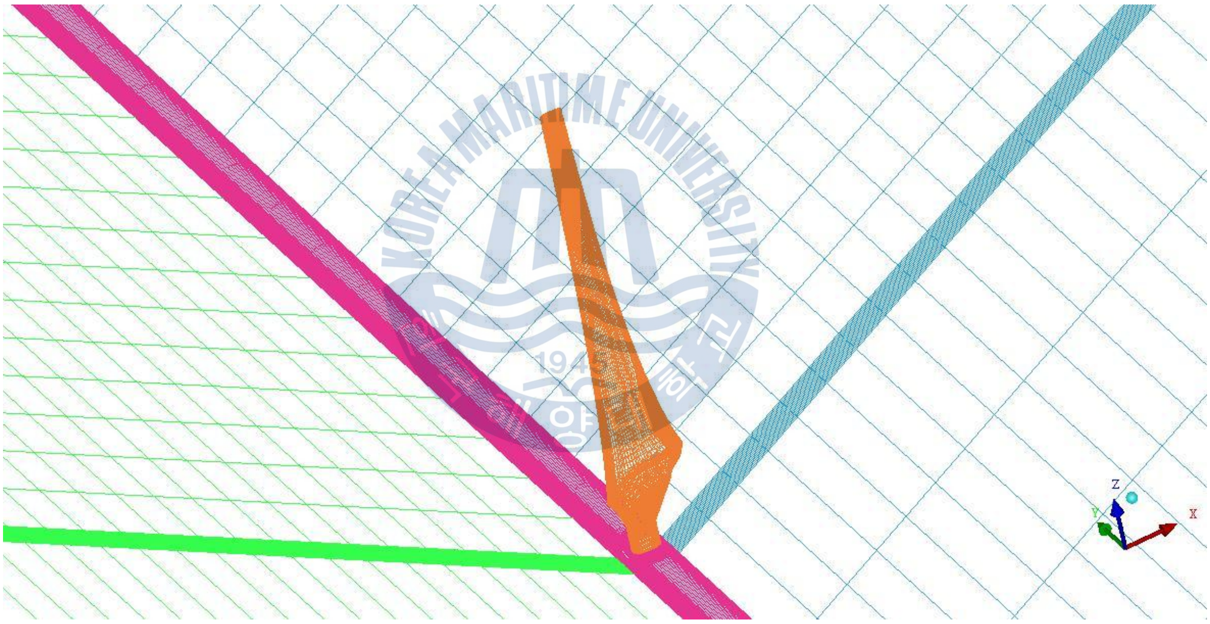

Figure 3.22: Meshing near the Blade

Near the blade of the HAWT, the detail of the flow is very important. Therefore the distance of the first node from the surface of the blade (or Y-Plus) must be taken into consideration. For the simulation of the HAWT, the average Y-Plus around the blade was around 6-8.

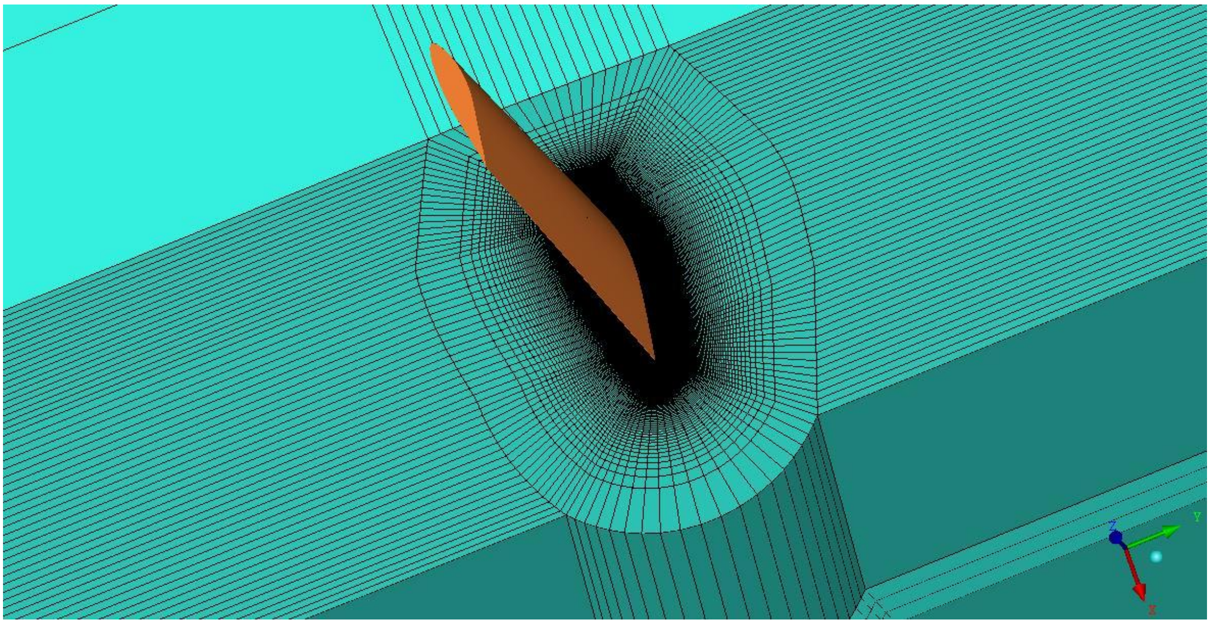

Figure 3.23: Mesh volumes Surrounding the blade

The total number of nodes for mesh of the HAWT is approximately 3.1 million nodes.

3.4.2 Cross flow turbine mesh

Unlike the HAWT blade, the cross flow turbine simulation required several meshes which were generated independently before combining the several meshes together. The parts were named as The Main Domain, Nozzle domain, Turbine domain, Internal Fluid domain, Top Strip/Lower Strip domain and the Diffuser domain. For all analysis involving the cross flow turbine, approximately the same number of nodes for the various domains were used.

The mesh of the various parts is shown in Fig.3.24.

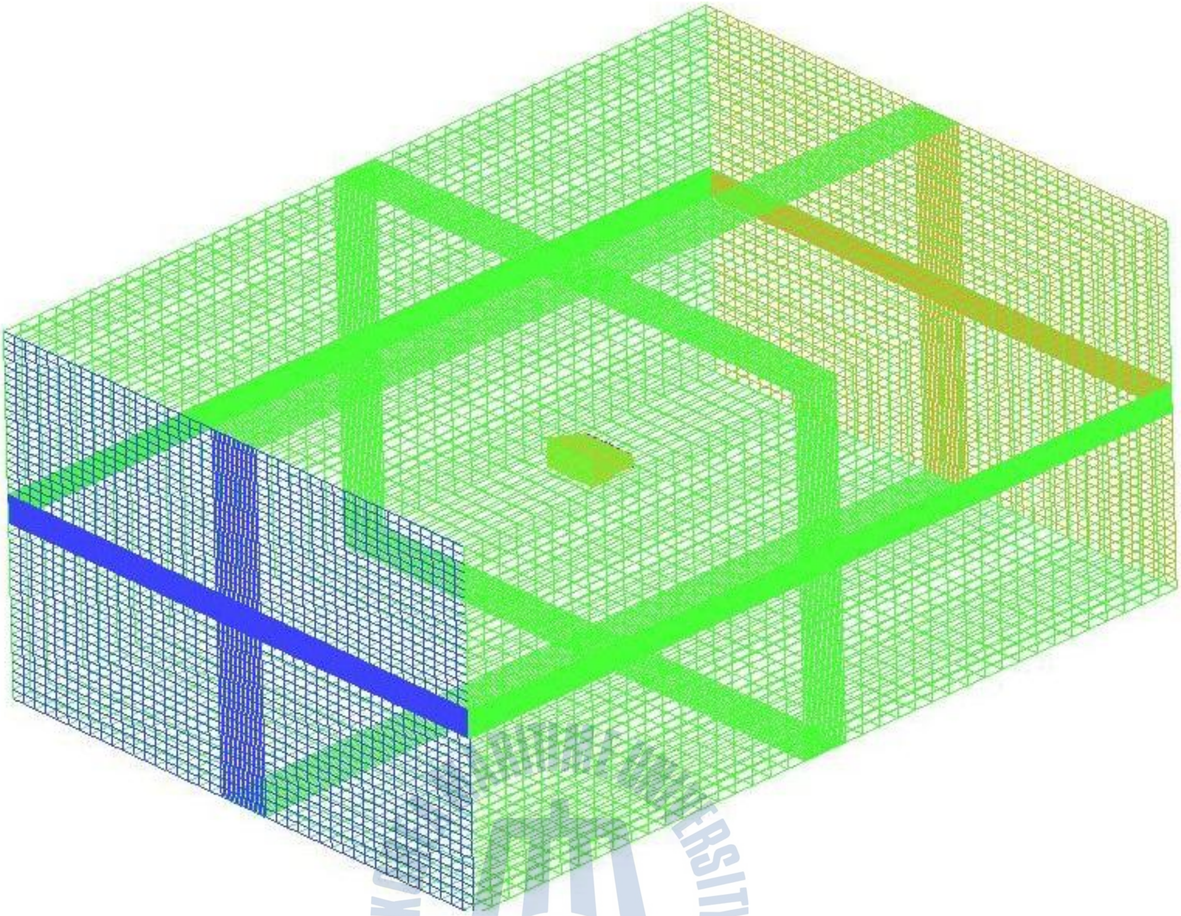

Figure 3.24: Computational grid of the domain for the cross flow turbine

The inlet and outlet is 100m from the turbine. A large domain is used to ensure convergence in the simulations. In addition, a casing is surrounding the nozzle, top strip, internal fluid, turbine and diffuser domains. This is done to make a higher quality mesh around the regions and simplify the mesh generation.

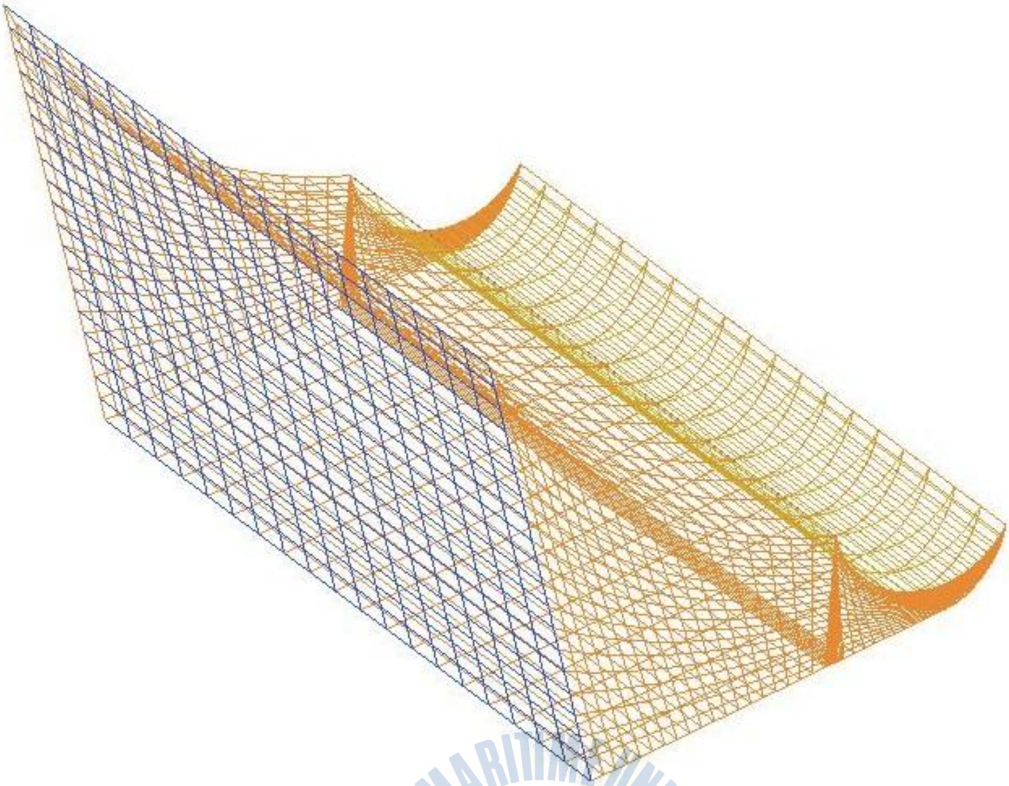

Figure 3.25: Mesh of the nozzle

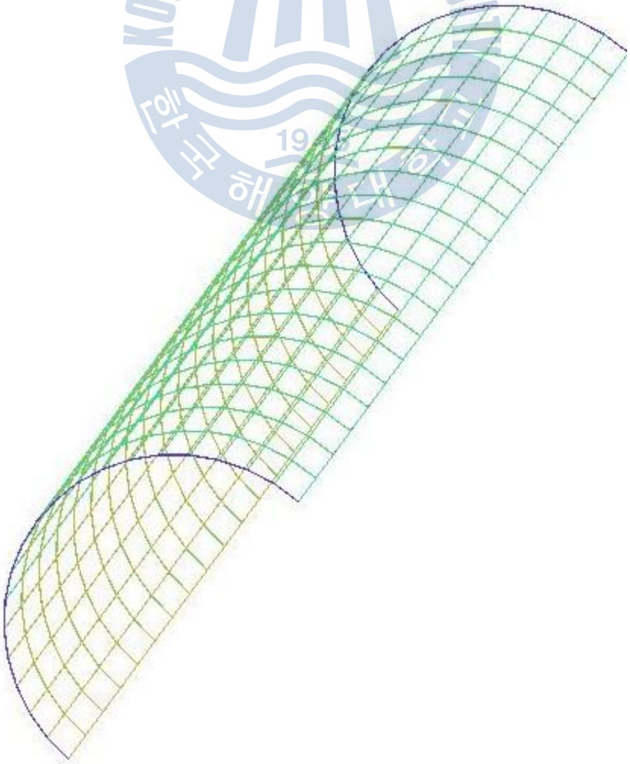

Figure 3.26: Mesh of the top strip part of the turbine

The top and lower strip meshes were similar except for their location in the geometry. The lower strip mesh was only used in Case 6 of the nozzle shape analysis and the 90° diffuser entry arc angle case.

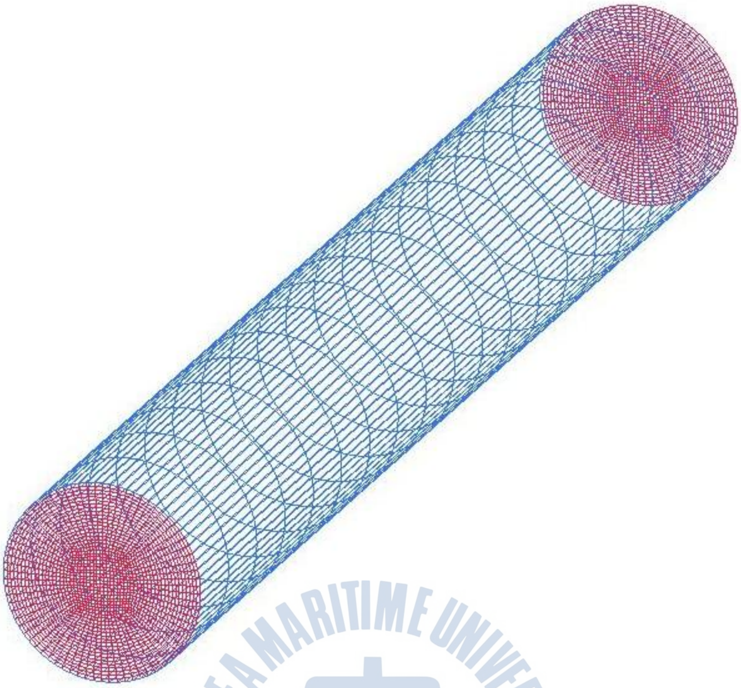

Figure 3.27: Mesh of the internal fluid domain

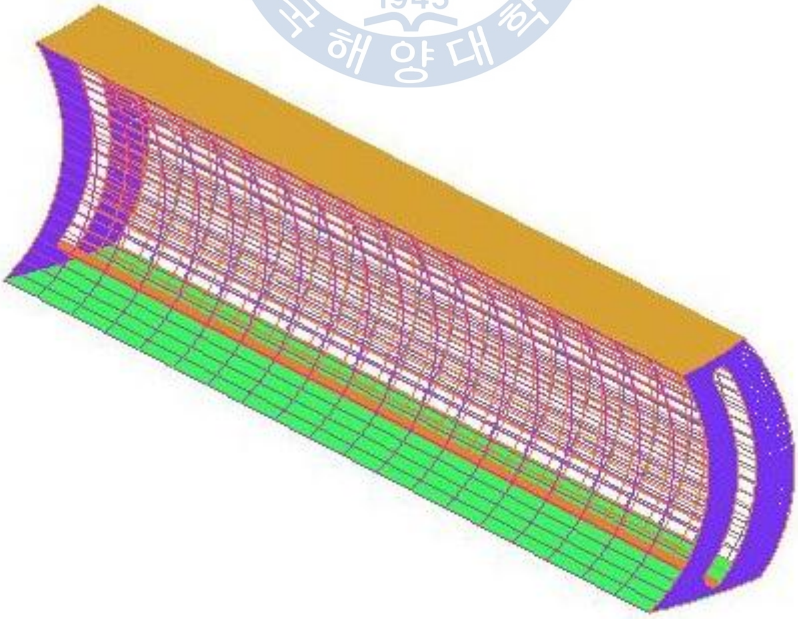

Figure 3.28: Mesh for the turbine blade

The mesh of the blade of the turbine is shown in Fig.3.28. Only one blade was meshed and the remaining 29 blades were added in CFX-Pre by mesh transformation. This method made the blade mesh generation much more simple.

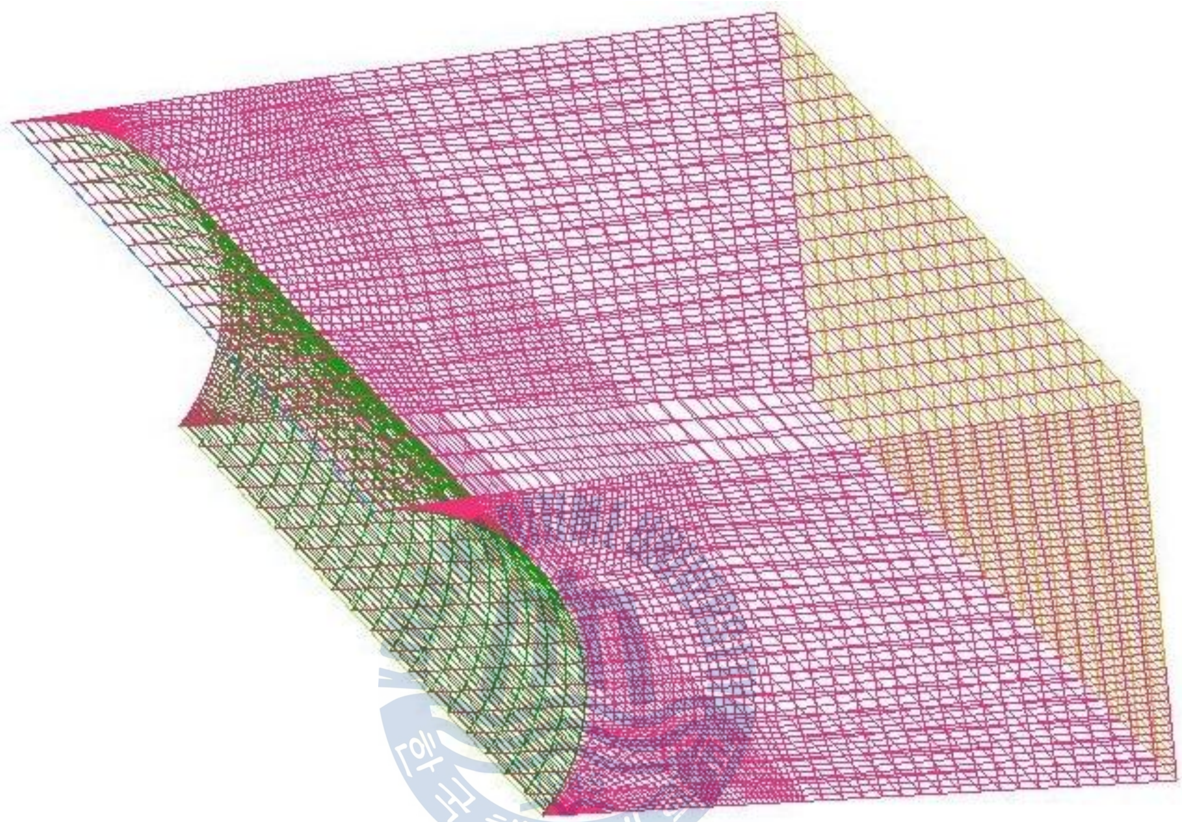

Figure 3.29: Mesh for the diffuser

A summary of the number of nodes is given in the following table.

Table 3.1: Number of nodes in various domains

Domain name	**Number of nodes**
MAIN	≈189280
NOZZLE	≈19200
TURBINE	≈1776000
TOP STRIP/LOWER STRIP	≈4000
INTERNAL FLUID	≈36880
DIFFUSER	≈37440

The next step after mesh generation is to define the necessary boundary conditions, fluid velocities and rotational speeds for analysis.

3.5 Simulation setup

In order to simulate the physical conditions of the two turbines, the conditions of the flow must be defined. In this study, the boundary conditions, fluid speeds and other variables are set using CFX Pre.

CFX Pre allows for specifications of fluid properties, various conditions at specified boundary regions and as well as the creation of user created expressions for monitoring during the solver process. Both simulations were analyzed as steady state simulations.

3.5.1 HAWT setup in CFX Pre

The setup for the HAWT is shown in Fg.3.30 below.

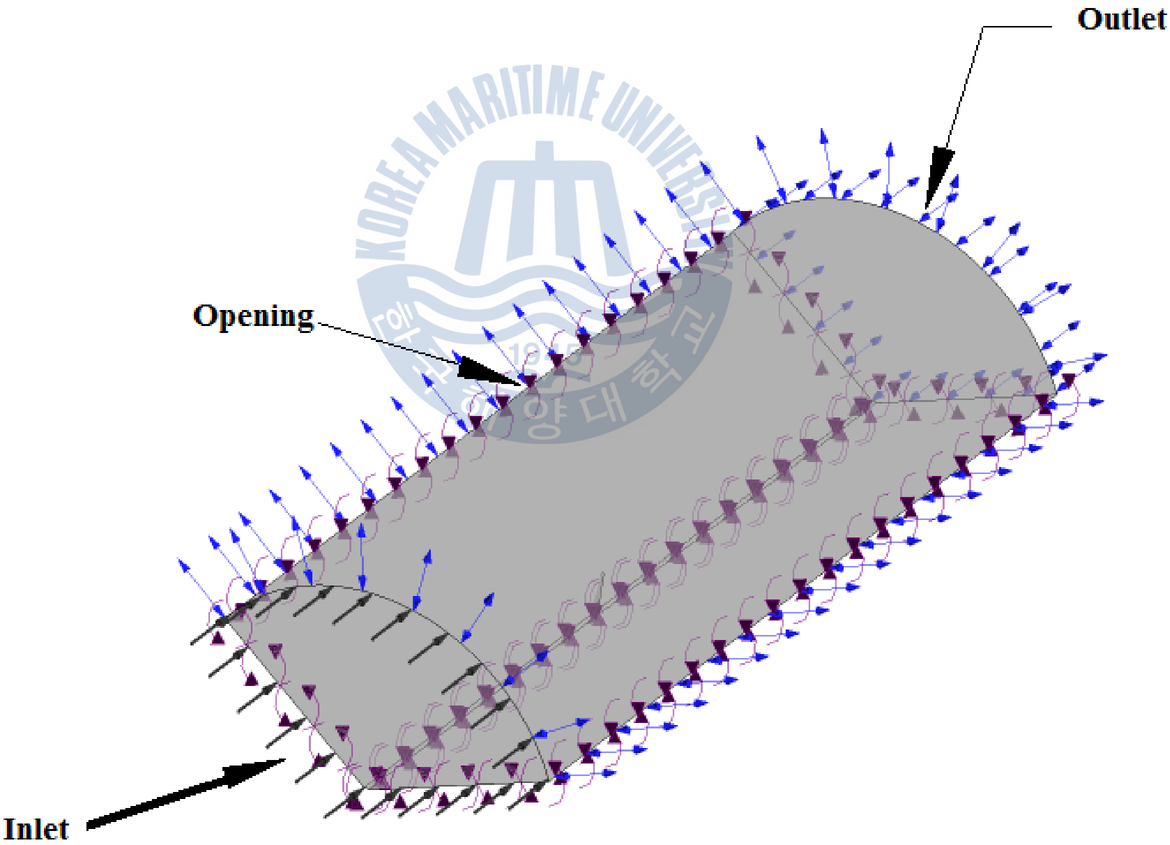

Figure 3.30: The setup of the HAWT simulation

For the simulation, the HAWT had to be tested over a range of wind speeds. For this project the wind speed range was from 7m/s to 20m/s. At the outlet and opening boundary above the blade, the relative pressure was set at 0 Pascal.

Since only one blade was modeled, the other two blades had to be accounted for using periodic conditions. Fig.3.31 shows the interface boundary where the rotational periodicity was selected as the interface model. Table 3.2 shows the summary of the conditions specified in CFX Pre.

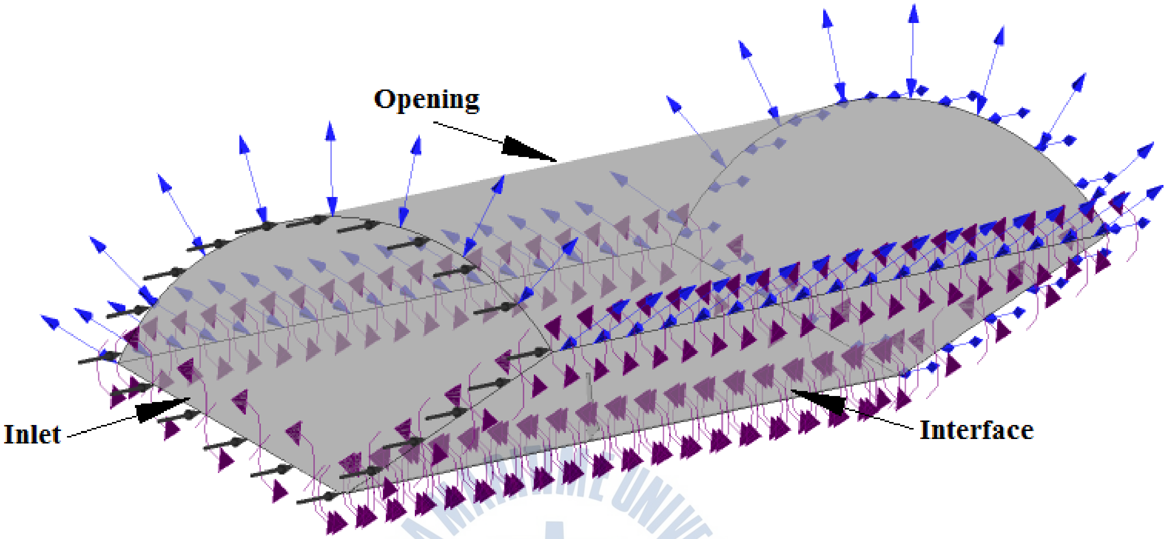

Figure 3.31: Setup of the HAWT simulation indicating the interface region

Table 3.2: Summary of the conditions in CFX Pre for the HAWT simulation

Simulation type	Steady State
Nodes	3,172,544
Turbulence model	Shear Stress Transport (SST)
Yplus (average)	6-8
Wind speed cases (m/s)	7, 10, 13, 15, 20
Rotational speed (RPM)	167.14

3.5.2 Cross flow turbine setup in CFX Pre

Fig.3.32 below shows setup for the cross flow turbine of the analysis in CFX-Pre.

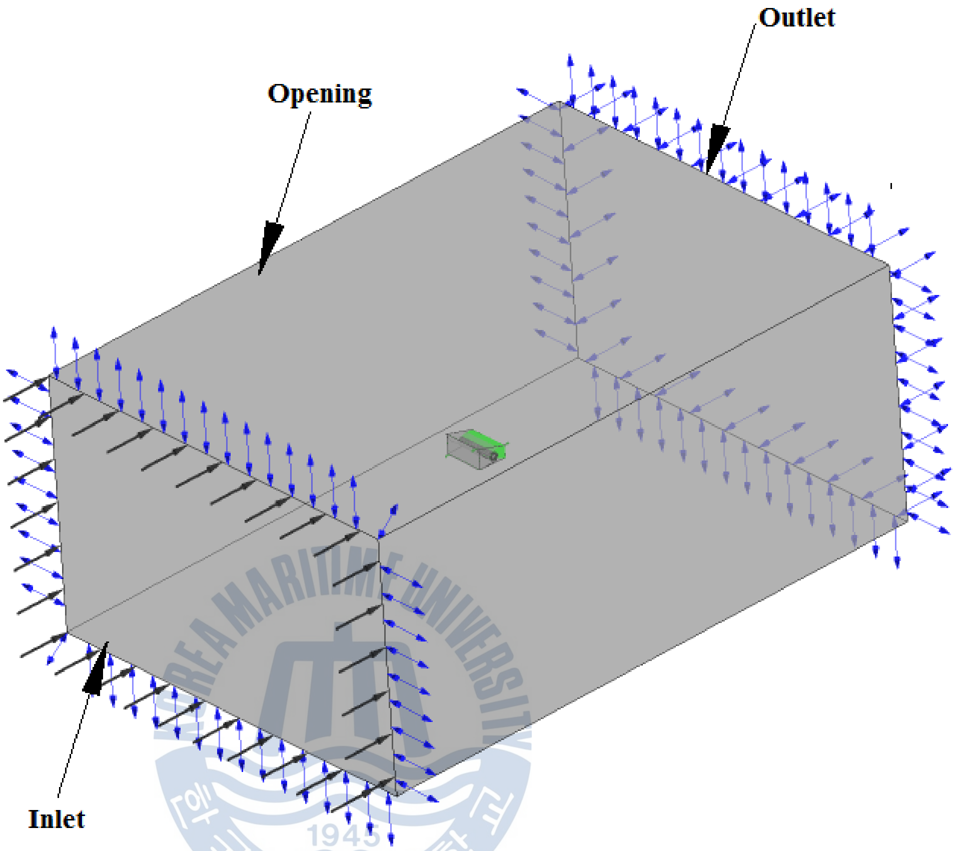

Figure 3.32: Overview of the whole domain with the various boundary conditions shown

Fig.3.33 shows a casing that surrounds the various parts of the turbine. This casing was added to simplify the meshing of the various parts.

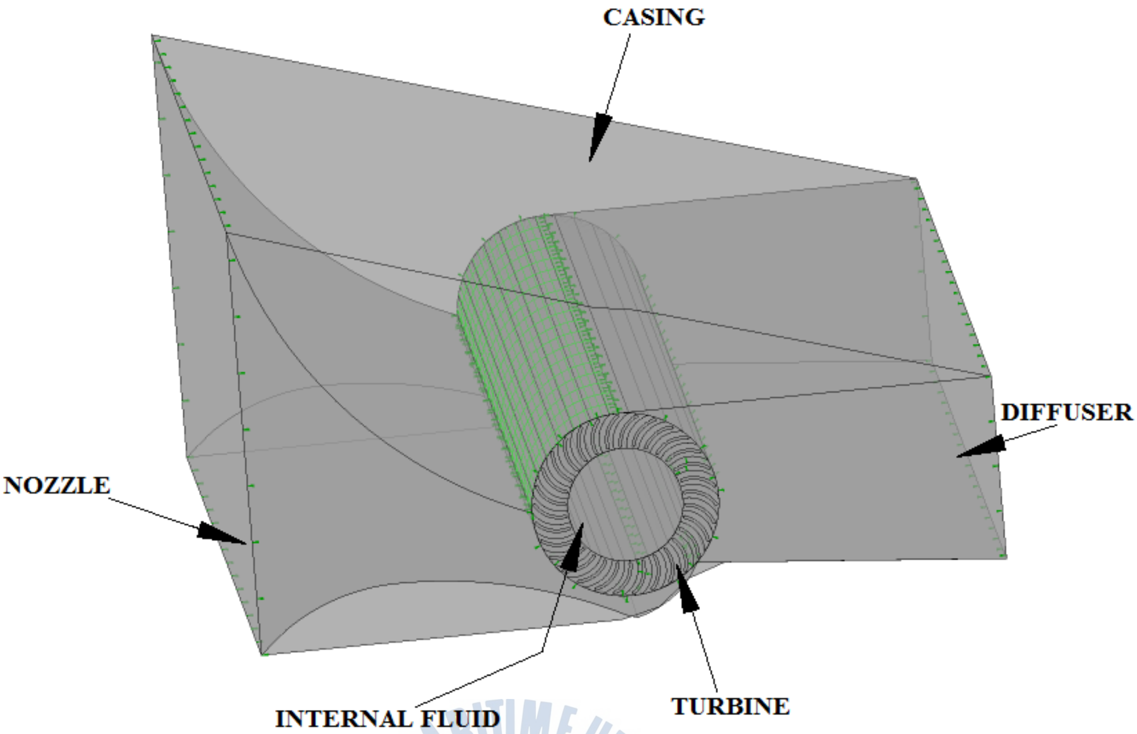

Figure 3.33: The setup of the cross flow turbine parts. A case surrounds the turbine parts.

The rotational speed of the turbine was varied for various tip speed ratios. The formula used to calculate the tip speed ratio and the angular rotational speed was given by equation (3.42):

$$\text{Tip Speed Ratio} = \frac{\omega\, r}{V_{inlet}} \qquad (3.27)$$

Where ω is the angular speed (rads/sec), r is the radius of the turbine (m) and V_{inlet} is the velocity at the inlet (m/s) which was set at 10m/s for all the simulations.

Table 3.3 shows the summary of the conditions that were selected in CFX Pre.

Table 3.3: Summary of the conditions for the cross flow turbine

Simulation Type	Steady state
Inlet Velocity (m/s)	10
Turbulence Model	Shear stress transport model

Rotational Speed (rads/sec)	2,4,6,8

3.6 Solving the simulation

Once the models have had the various variables and boundary conditions specified, the following step is to solve for the solutions using a solver. This study used the CFX-Solver 13.0 software as the solver.

There are several techniques that can be used to solve the governing equations that were described earlier. CFX uses the Finite Volume Method (FVM) approach to solve the required equations. This approach divides a region of interest into smaller control volumes where the required properties are calculated at the centroid of the volume [21] shown by Fig.3.34.

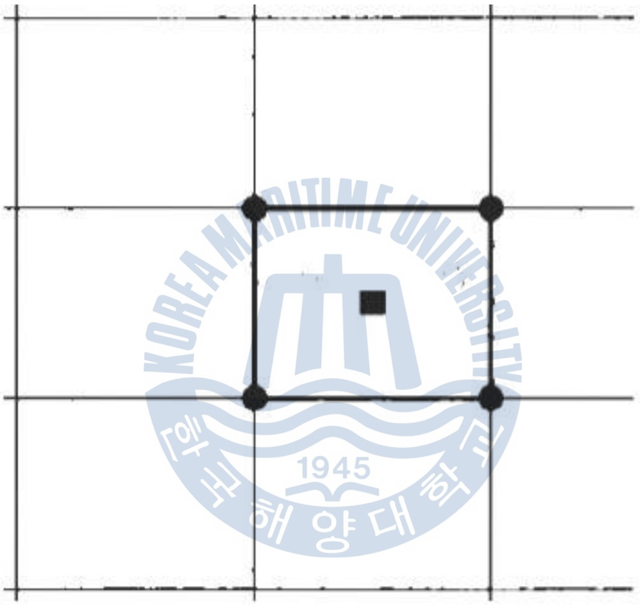

Figure 3.34: A cell centered FVM approach

The next step requires the integration of the differential form of the governing equations for each of the control volumes. To describe the variation of the said property, interpolation profiles are assumed resulting in the discretization equation. The discretization equation describes the conservation principle for a property inside of the control volume.

At the completion of the simulation using the solver, the final step for analysis is the post-processing step.

3.7 Post processing

The post processing takes place after the required simulation is completed. Post Processing refers to processing the result of the simulation by a number of ways:

- Generating a visual representation of various flow variables over the geometry
- Generating animations of flow vectors
- Analyzing flow variable distributions
- Processing of results for output onto a chart

The ANSYS software provides CFX-Post as a Post processor function. The results obtained from the simulations of the two turbines were analyzed in CFX-Post and the results will be discussed in the next chapter.

Chapter 4 Results and Discussion

The results of the two simulations are presented in this chapter. This chapter will first analyze the results of the horizontal axis wind turbine simulation. The power output, the efficiency and as well the flow over the blade will be discussed.

The analysis of the results of the cross flow turbine will then be discussed. In a similar manner, the output power, efficiency and flow characteristics will be looked at.

After the two turbines have been analyzed, the final section will compare the performances of the two turbines.

4.1 Horizontal axis wind turbine analysis

4.1.1 Power output

The power output of the HAWT versus the wind speed is given by Fig.4.1.

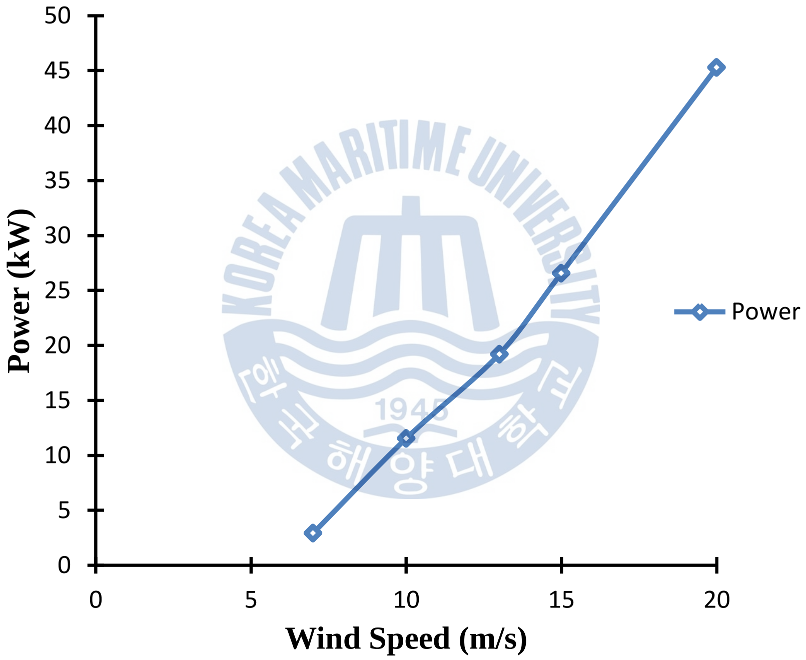

Figure 4.1: HAWT power output (kW) at various wind speeds (m/s)

The graph shows a linear increasing trend for the power output as the wind speed increases. At the design wind speed of 10m/s, the power output is 11.54kW. While this was slightly over the design target of 10kW, the objective of 10kW design was achieved given the initial design parameters.

However, from the graph it is clear that the turbine power control method is not that effective. The power output increases as the wind speed increases. This could lead to damage on the wind turbine [12].

Since the blade was fixed at 0° pitch angle for this simulation, the blade pitch angle can be changed to improve the passive stall power control on the turbine. In addition, the twist and chord length distribution can also be changed to ensure that the blade output power is only reduced at wind speeds that can be damaging to the turbine.

This graph showed that the blade could achieve the required power output and in the following section, the blade efficiency in power production will be discussed.

Fig.4.2 shows the power coefficient (C_P) at the various wind speeds tested. The power coefficient is the ratio of the output power of the wind turbine to the available kinetic power of the wind, essentially the efficiency of the turbine at a certain wind speed.

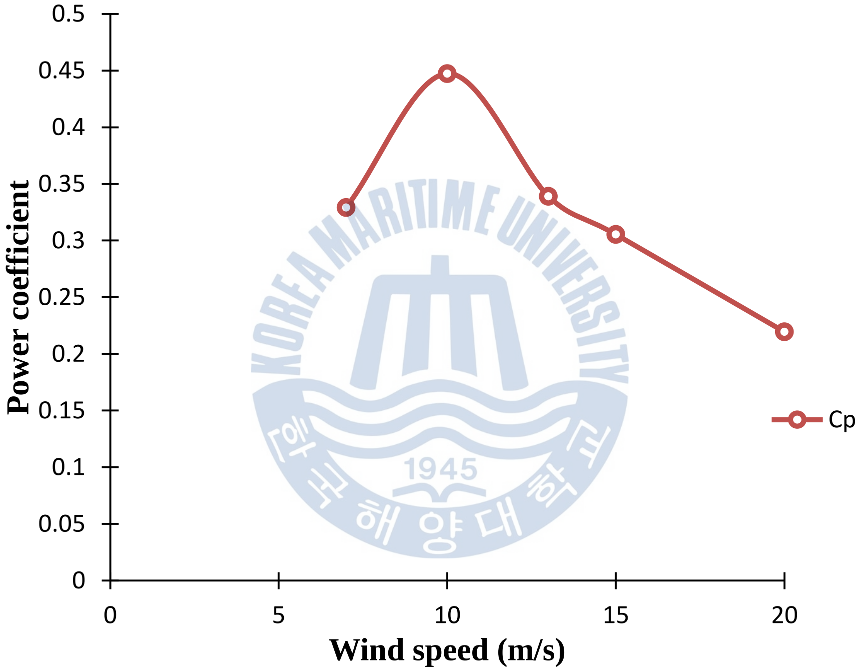

Figure 4.2: Power coefficient at various wind speeds

At 7m/s, the C_P value is 0.33 and as the wind speed is increased to 10m/s, the C_P increases to a maximum of 0.45. After this wind speed, the C_P graph shows a declining trend until it reduces to a minimum of 0.22 at 20m/s.

The design C_P of the blade was 0.43 at 10m/s was surpassed and the blade achieved a higher C_P value.

To further investigate the flow field over the wind turbine, the streamlines of the flow over the blade was analyzed.

4.1.2 Streamlines

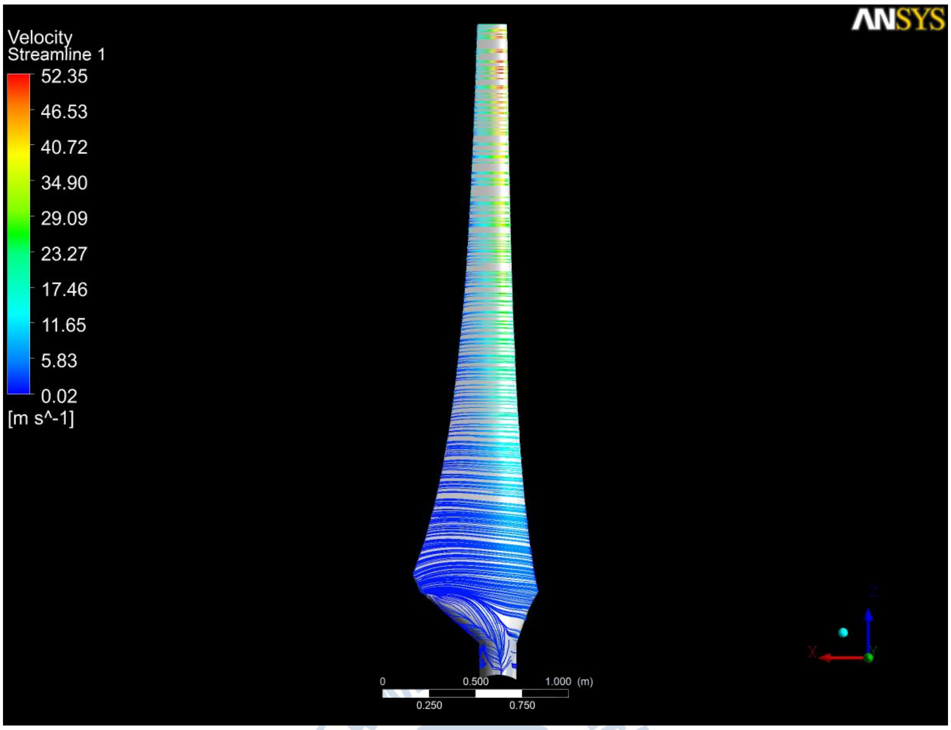

Figure 4.3: Streamlines over the suction side of the blade at 7m/s

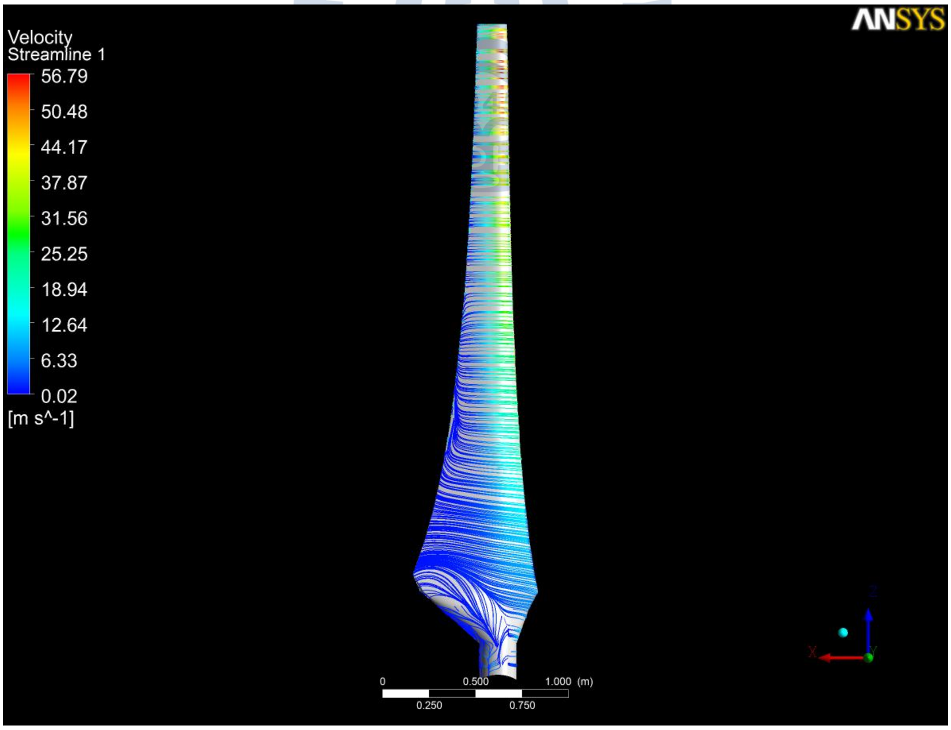

Figure 4.4: Streamlines over the suction side of the blade at 10m/s

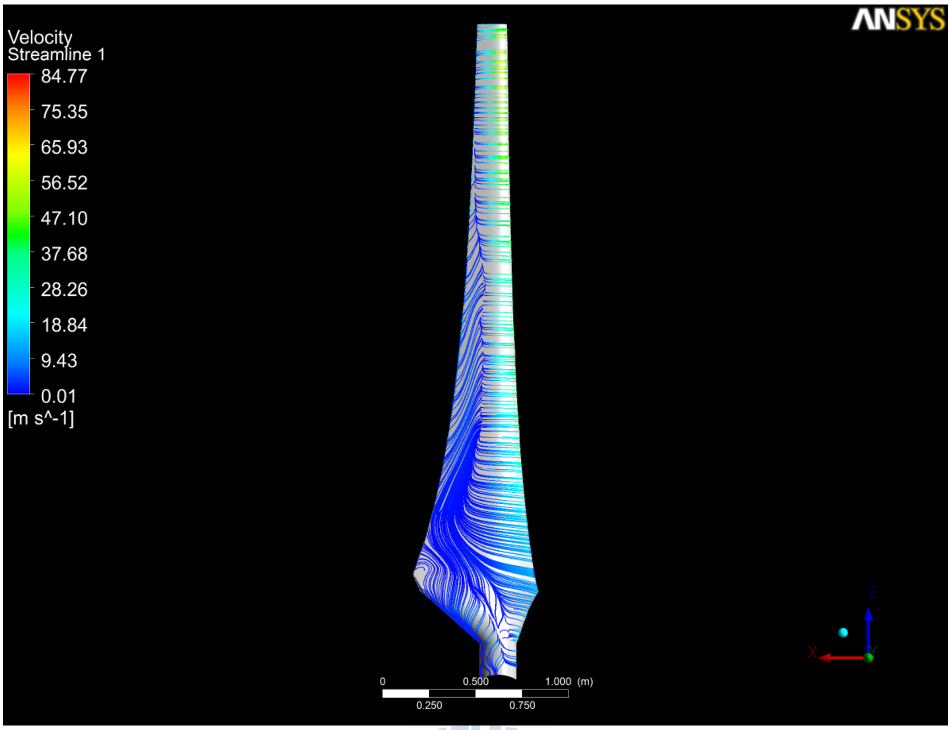

Figure 4.5: Streamlines over the suction side of the blade at 15m/s

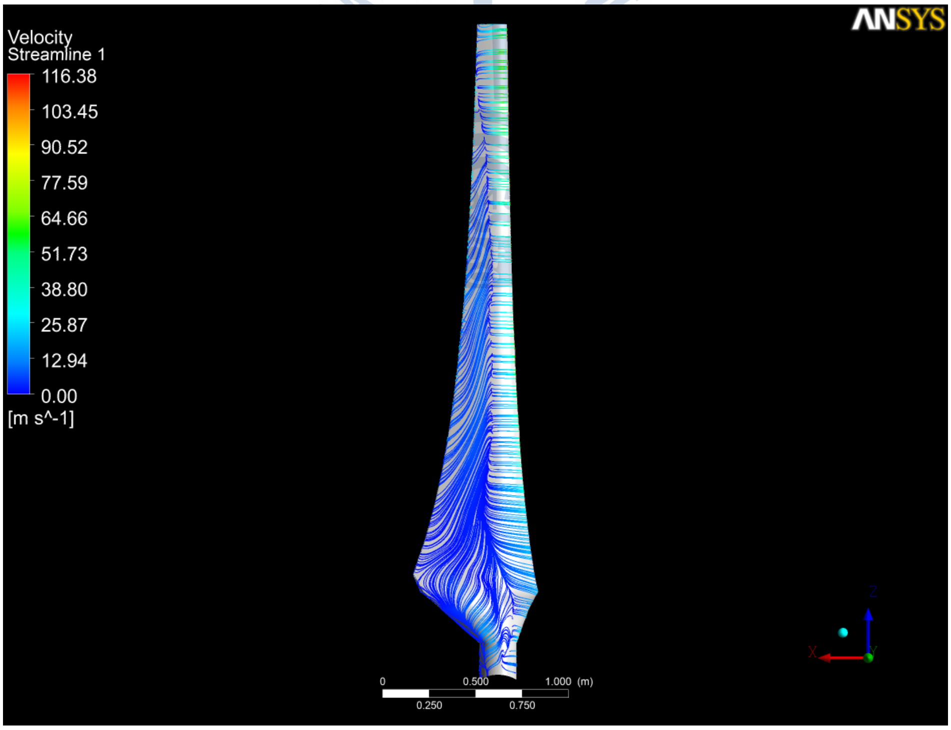

Figure 4.6: Streamlines over the Suction side of the blade at 20m/s

The streamlines of the flow are given in Fig.4.3 to Fig.4.6. At 7m/s, the streamlines show the flow remains attached over majority of the blade with slight stall occurring near the root of the blade. This stall is primarily due to the high angle of attack on the blade at this section. As the wind speed increases to 10m/s, more stall occurs near the root of the blade but most of the flow elsewhere on the blade remains attached. It can also be seen that the separated flow at the root moves toward the tip of the blade.

This movement toward the tip can be more clearly seen at 15m/s where most of the blade, especially near the trailing edge, is under stall. This movement of the stalled flow is due to the centrifugal force [25, 26]. Most of the flow at the leading edge remains attached. This effect is attributed to the Coriolis force, which acts toward the trailing and can be considered as a favorable pressure gradient [25, 26]. The increase in the amount of stall at this wind speed also corresponds to the decrease in C_P value shown in the previous graph of the coefficient against wind speed. Stall decreases the lift force on wind turbine blade and greatly increases drag force [12]. Passive stall controlled turbines utilize this fact to control the output of the turbine. However, as it was seen beforehand in the Fig.4.1, the power continued to increase as the wind speed increased. Therefore, to improve the power control at wind speeds past 10m/s, the blade may be fixed at different pitch angle to increase the amount of stall at higher wind speeds.

Finally at 20m/s, most of the blade is under stall although the flow still remains attached from the leading edge of the blade to approximately the middle point on the suction side of the blade.

4.2 Cross flow wind turbine analysis

4.2.1 Turbine entry arc analysis results

The power coefficient (C_P) versus the tip speed ratio (TSR) is presented in Figure 4.7. The cases have some similarities in between them. All cases have produce low power at low tip speed ranges and peak at a TSR of 0.4 before decreasing as the TSR increases.

The 90° case shows the lowest C_P at TSR of 0.4 with 0.05. The next highest C_P occurs in the 30° case, where the maximum power coefficient is about 0.07. As the angle increases to 120°, the max C_P is increased up to 0.072. At 135°, the maximum C_P is about 0.087

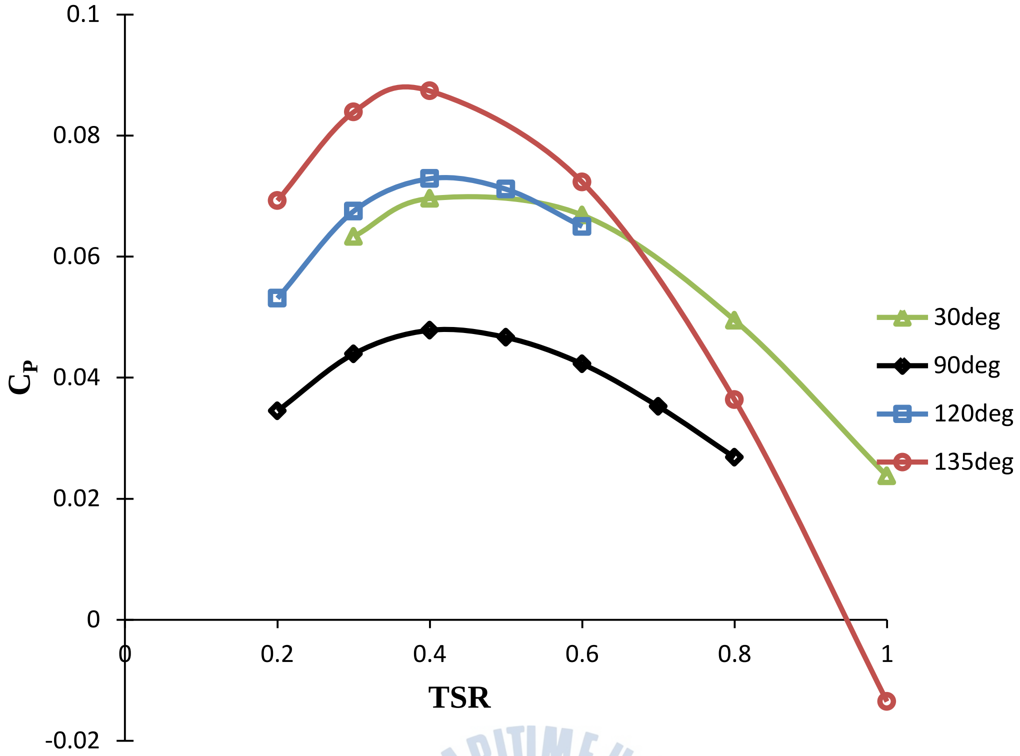

Figure 4.7: Power coefficient versus tip speed ratio for turbine entry arc analysis

To further analyze the shapes, the velocity and pressure contours for all the cases at a TSR of 0.4 are shown from Fig.4.8 to Fig.4.15.

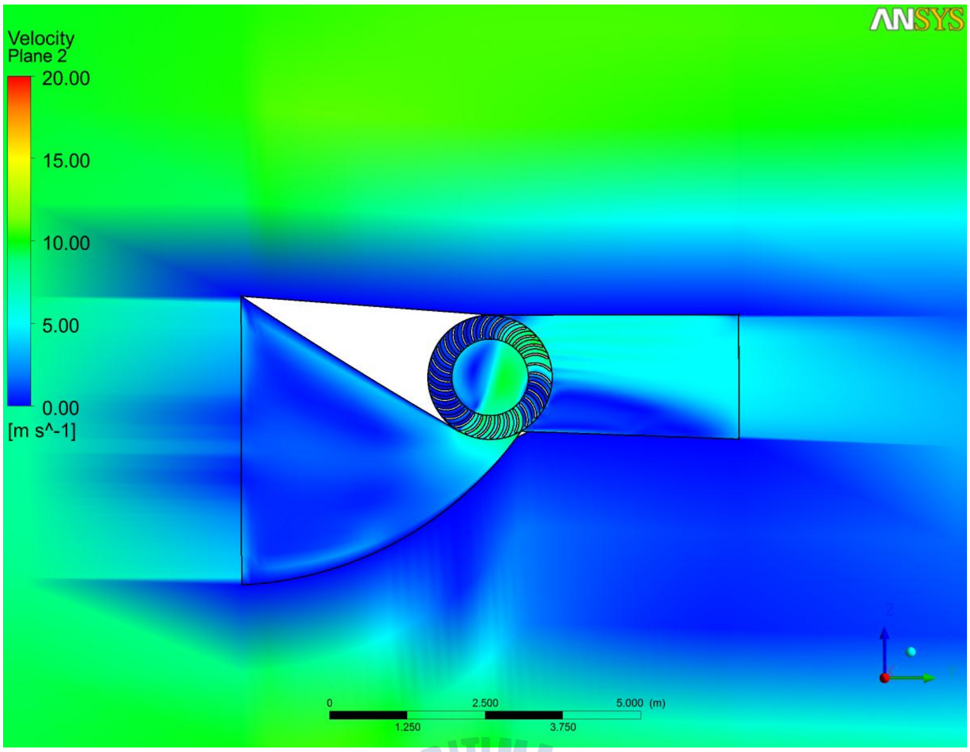

Figure 4.8: Velocity contours at turbine entry arc at 30°

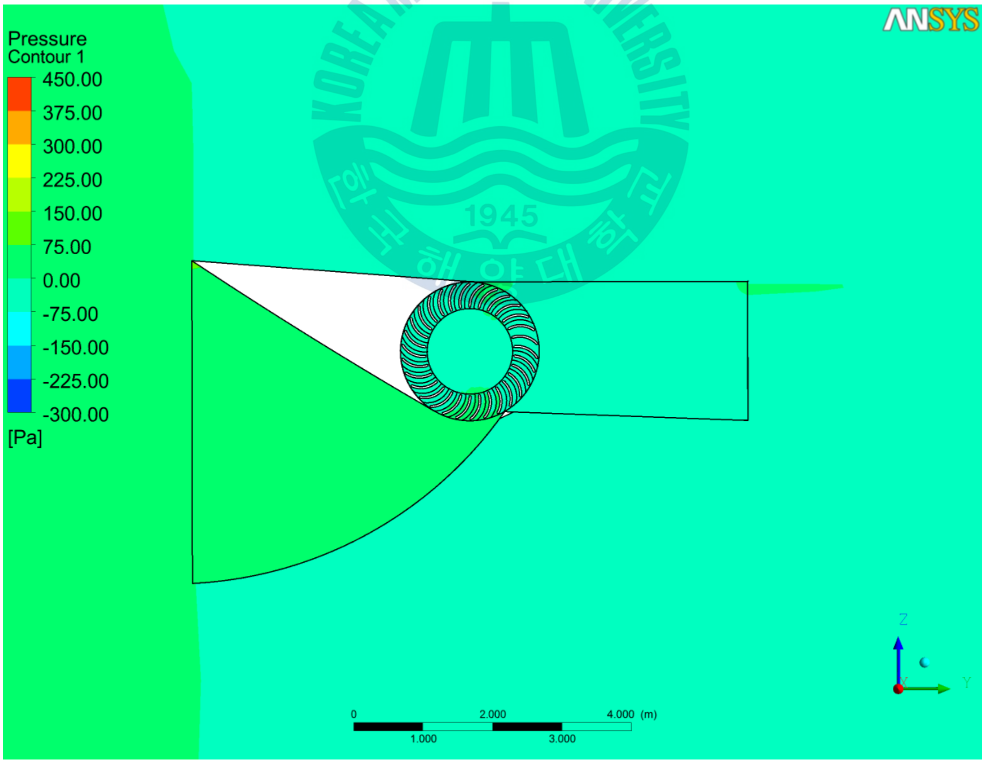

Figure 4.9: Pressure contours at the turbine entry arc at 30°

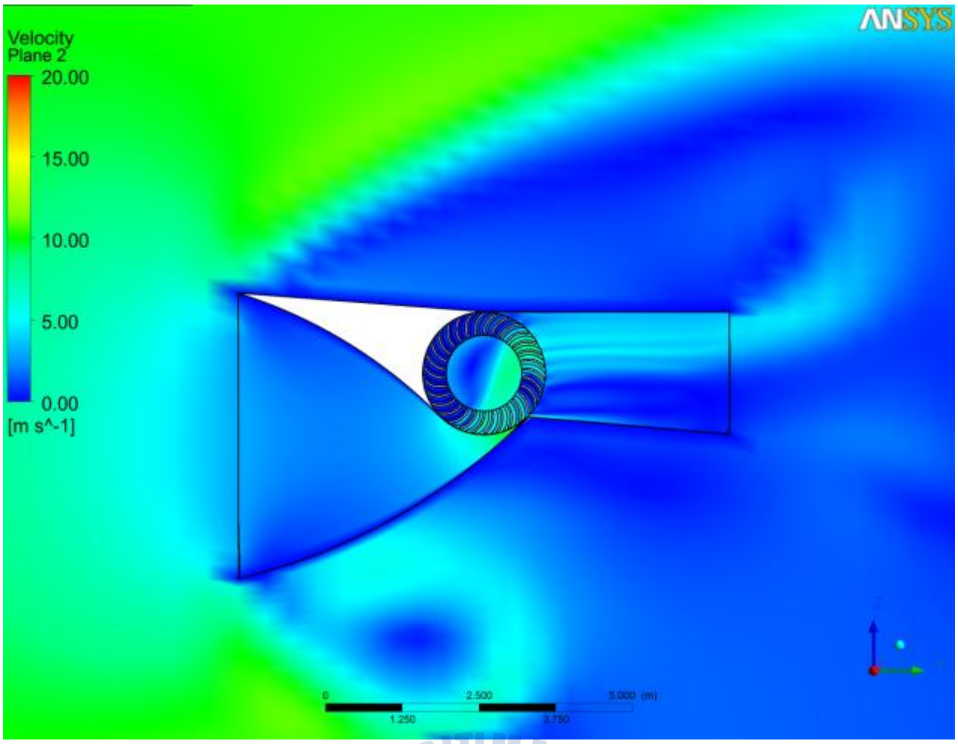

Figure 4.10: Velocity contours at the turbine entry arc at 90°

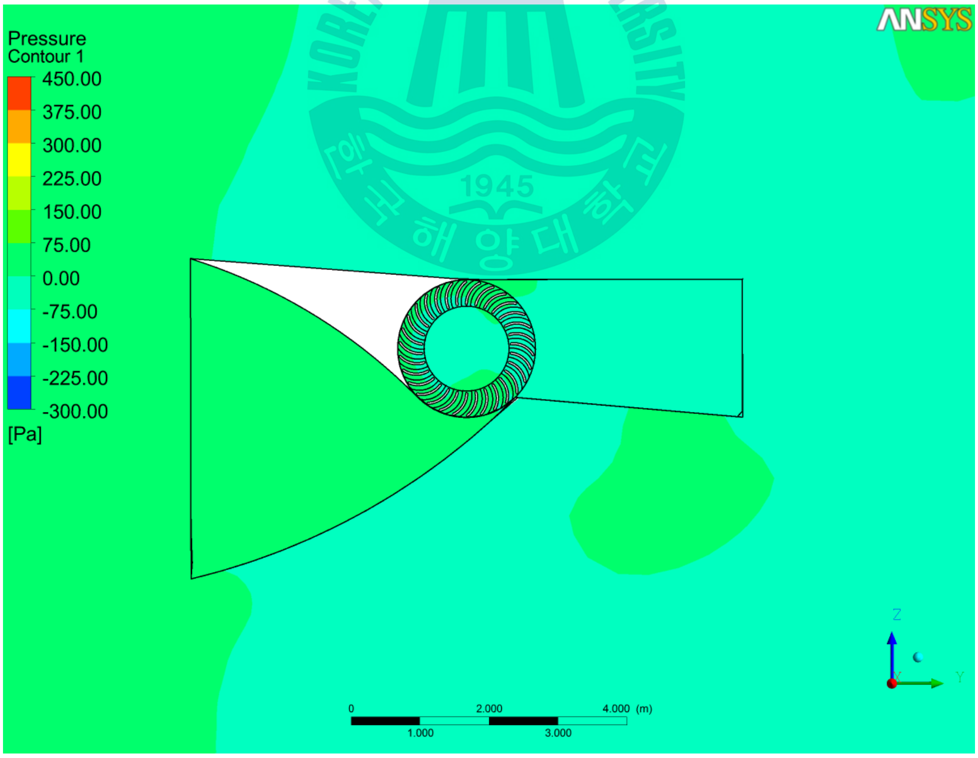

Figure 4.11: Pressure contours at the turbine entry arc at 90°

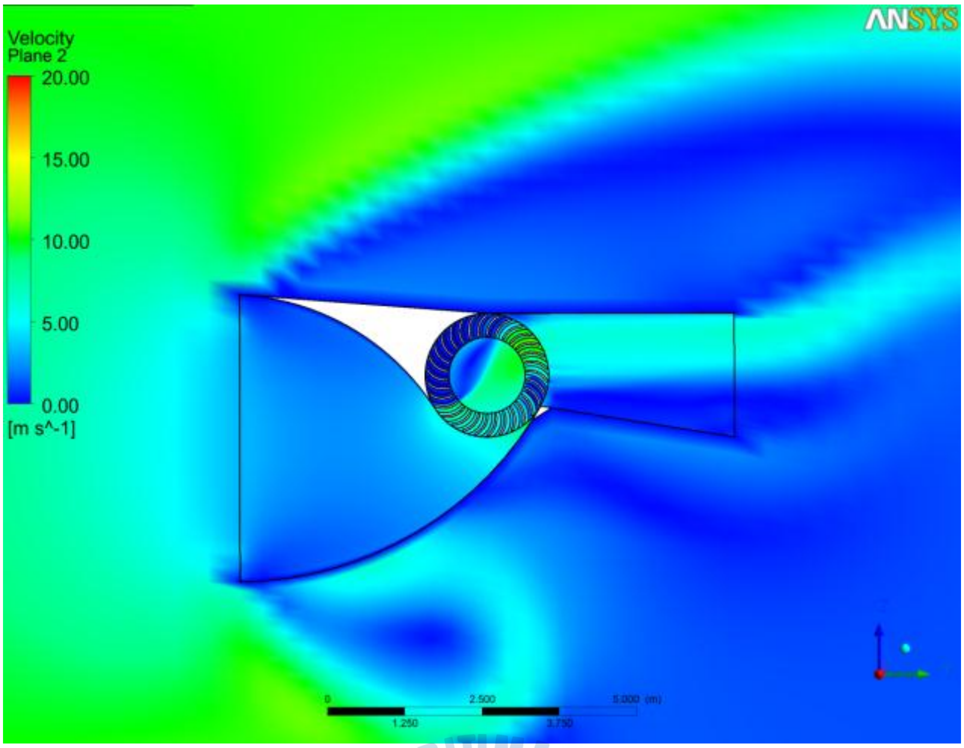

Figure 4.12: Velocity contours at the turbine entry arc at 120°

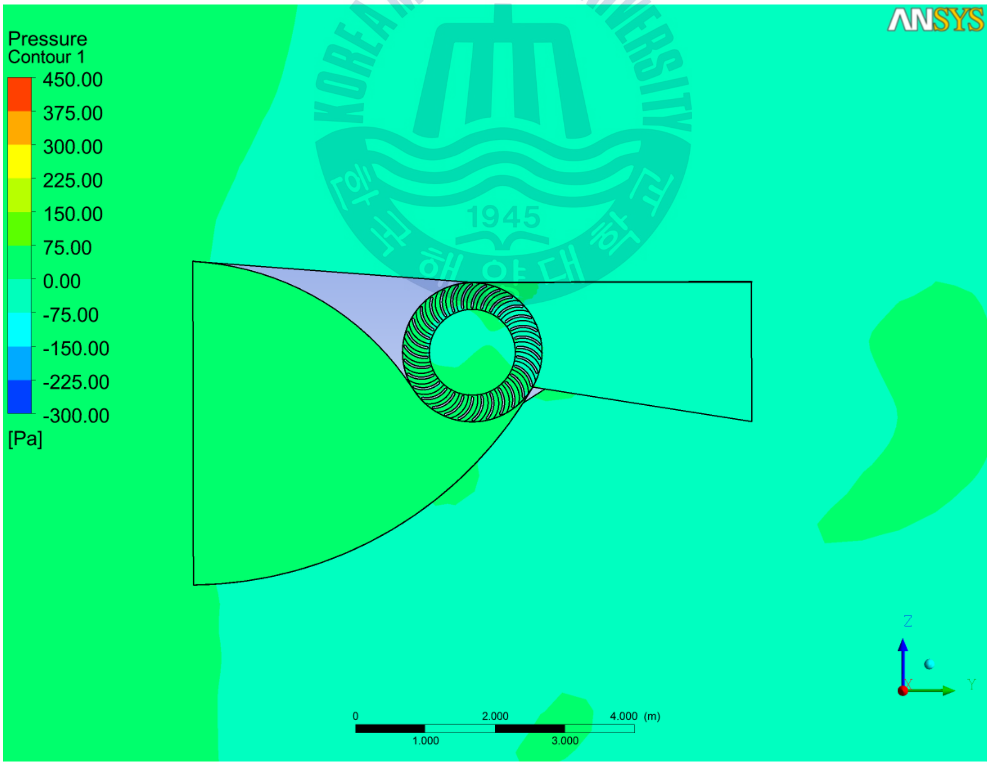

Figure 4.13: Pressure contours at the turbine entry arc at 120°

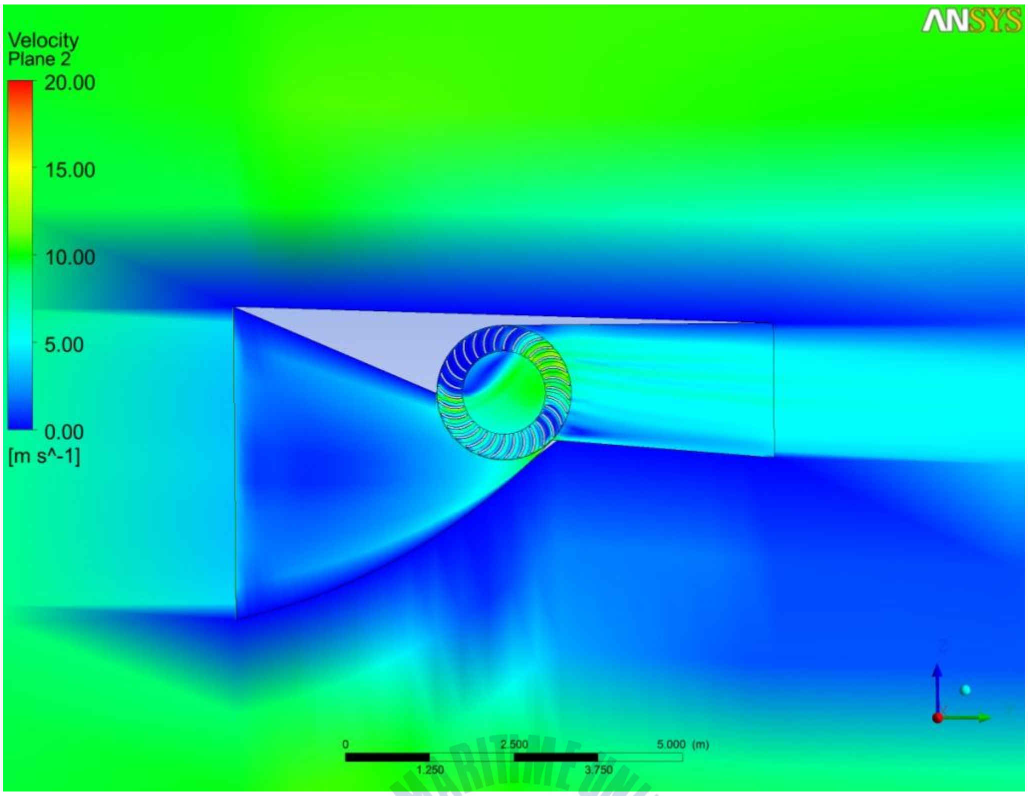

Figure 4.14: Velocity contours at the Turbine Entry Arc at 135°

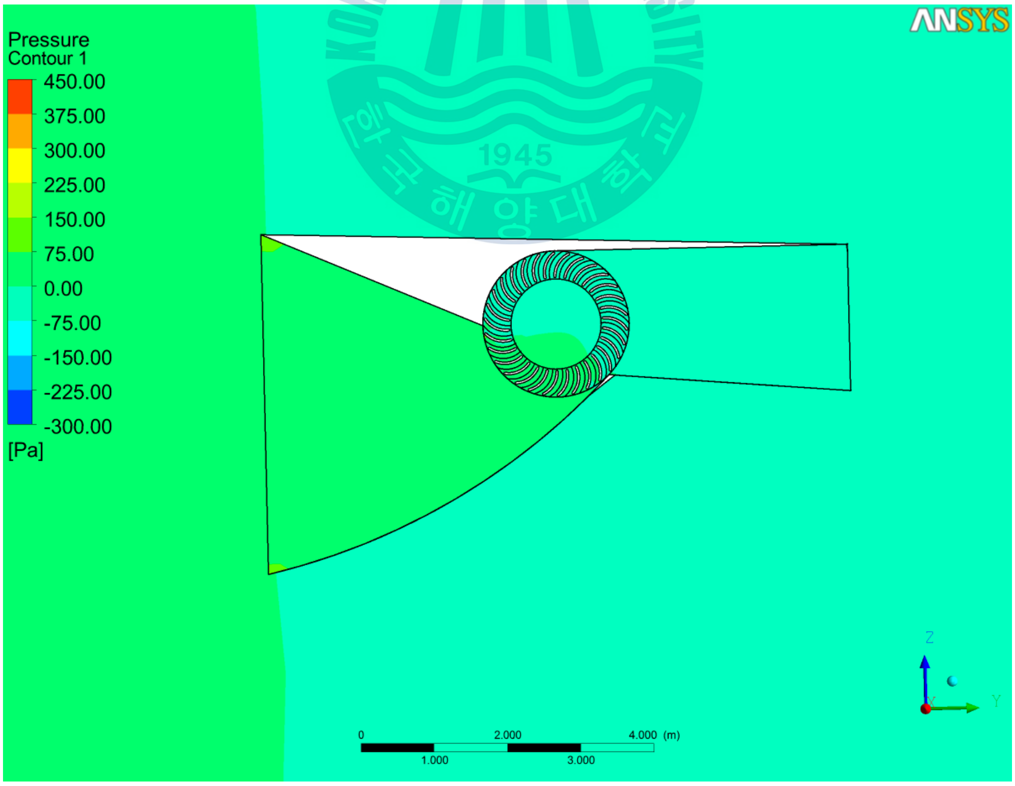

Figure 4.15: Pressure Contours at the Turbine Entry Arc at 135°

The pressure contours show that a high pressure region at the inlet and within the nozzle. At the turbine the pressure reduces and a region of lower pressure is seen at the turbine and diffuser area.

The velocity contours show the flow slowing down from the inlet speed of 10m/s to below 5m/s before the flow enters the turbine. The flow accelerates and increases on the wall of the nozzle whereas the flow within the middle of the nozzle remains low. The best case (135°) showed larger volume of air accelerating through the entry arc and exiting the turbine than all the other cases as shown by the velocity contours. This larger volume flow rate can be plotted and seen in the volume flow rate of the air just before entering the turbine at the different tip speeds is given in Fig.4.16. The figure shows that at 135° entry arc angle the flow rate is remains the highest out of the all the cases. As the tip speed ratio increases, the flow rate also decreases for all cases.

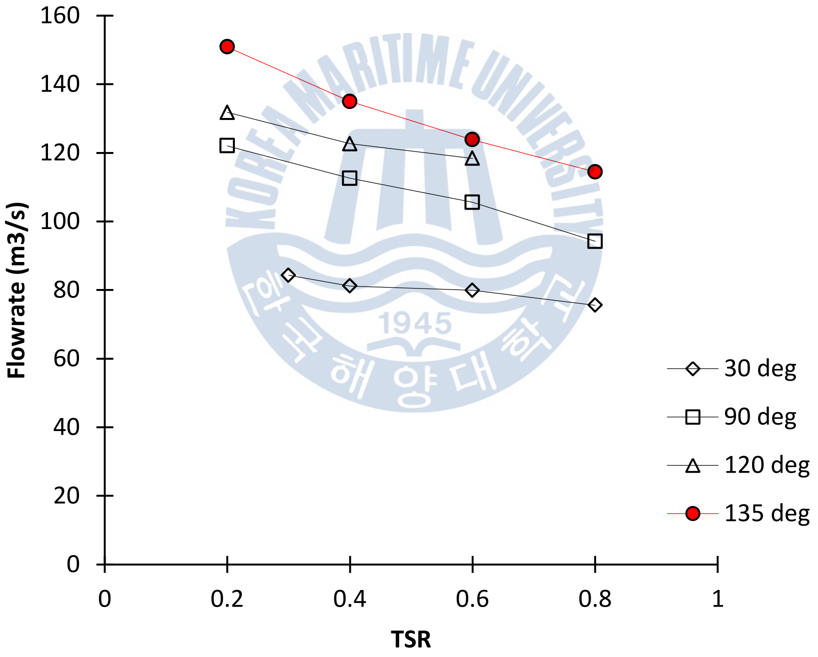

Figure 4.16: Flow rate at the turbine entry arc for the arc angle analysis

As arc angle increases, the area for the air to enter the turbine also increases. This increase in area allows for a larger volume of air to go enter the turbine, providing more kinetic energy for extraction. In addition, the area increase reduces the flow resistance near the nozzle inlet allowing a higher velocity air into the turbine as shown in the next figure. Here u/V is a non-dimensionalised number which is the ratio of the velocity at a given point to the velocity at the inlet (10m/s).

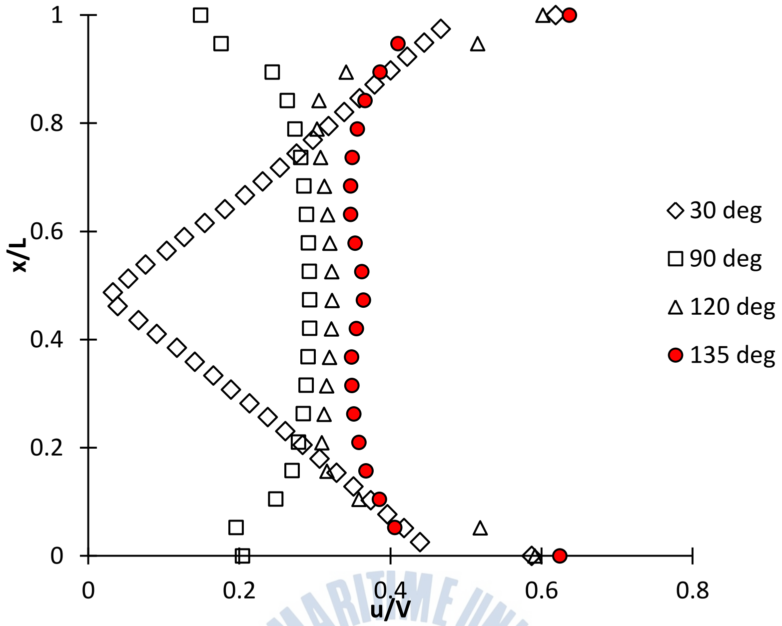

Figure 4.17: Velocity profile over the inlet of the nozzle

Fig.4.17 shows the velocity profile of the flow at the inlet of the nozzle. As the arc angle increased, the velocity profile improves and the magnitude of the flow into the turbine also increases.

For the next analysis of nozzle shapes, all cases (except for case 6) had an entry arc of 135°.

4.2.2 Nozzle shape analysis

The graph of C_P against TSR is shown in Fig.4.18. The case with the highest output is case 3 with a maximum C_P of approximately 0.105 which increased by 20% compared to the previous analysis. With cases 2, 4, 5 and 6, there was not much difference in C_P yielding a maximum of 0.087, 0.092, 0.089 and 0.093 respectively.

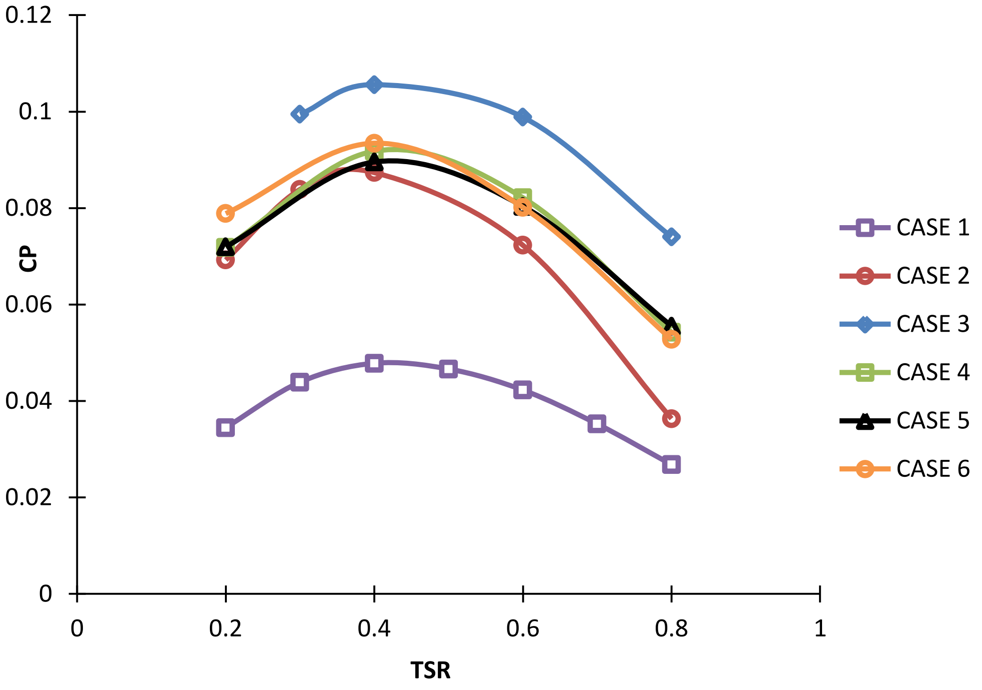

Figure 4.18: Power coefficient versus TSR for the nozzle shape analysis

The flow rate at the entry arc into the turbine for the various cases was studied and this is presented in Fig.4.19, where the flow rate of the air at the various tip speed ratios is compared.

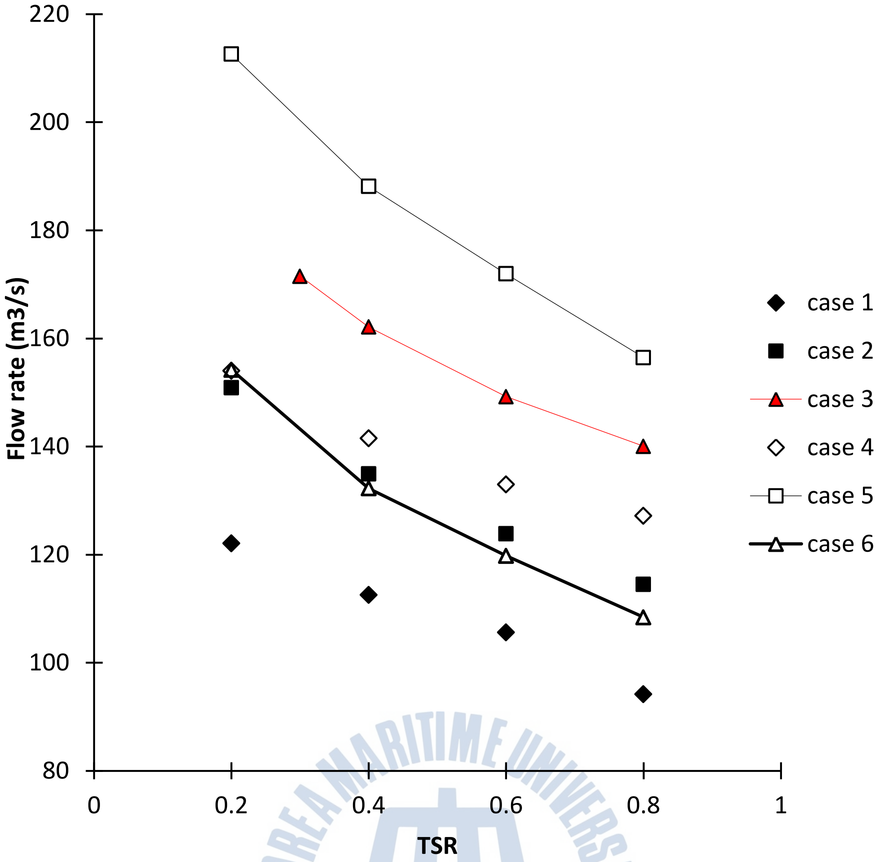

Figure 4.19: Flow rate at the entry arc for the nozzle case analysis

The case with highest C_P (case 3) shows higher flow rate into the turbine than all other cases except for case 5. However, case 5 had a lower C_P of 0.089. The lower performance despite the higher flow rate can be attributed to the geometry of the lower nozzle wall near the turbine entrance. This effect can be seen in Fig.4.20 which shows the magnitude of velocity at the entry arc angle. The sharp drop in velocity corresponds to the area in which the drop occurs in the geometry of the bottom wall in case 5.

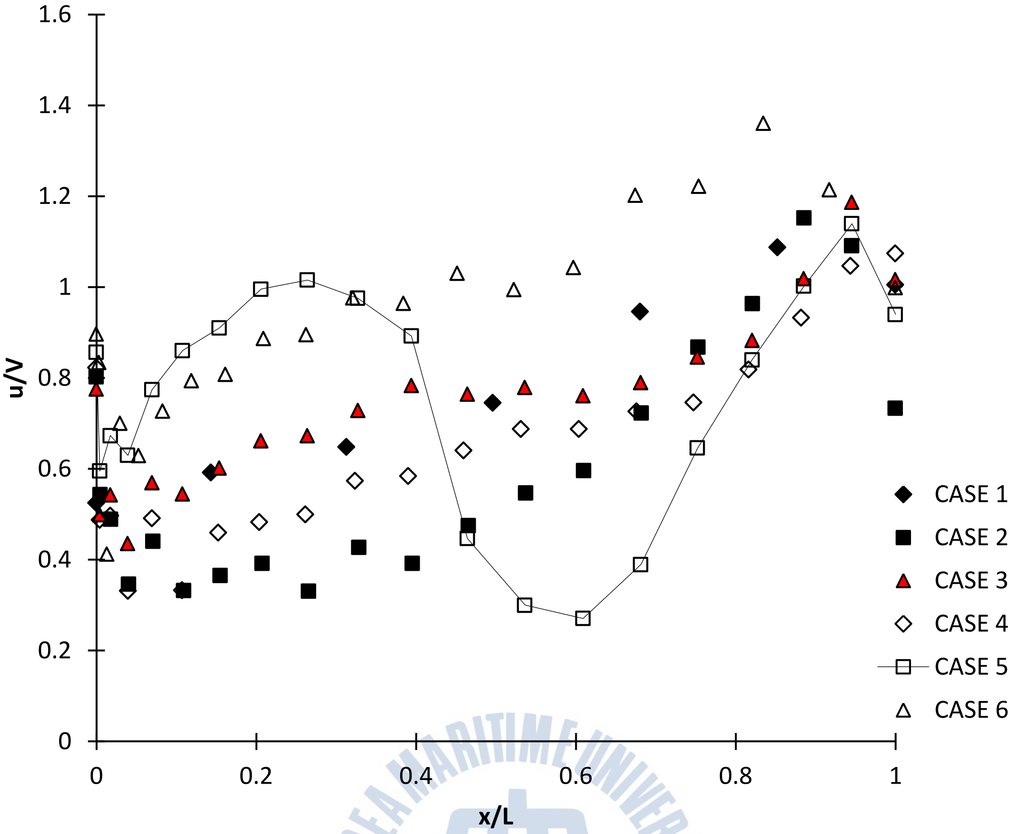

Figure 4.20: Velocity profile at the turbine entry arc

The velocity vectors with the corresponding velocity contours are shown in Fig.4.21 to Fig.4.32.

In a similar manner as discussed in the previous section, the figures show how the fluid velocity slows down at the inlet of the nozzle. The velocity vectors also show how the approaching flow near the top and bottom of the nozzle tend to flow around the nozzle instead of into the nozzle.

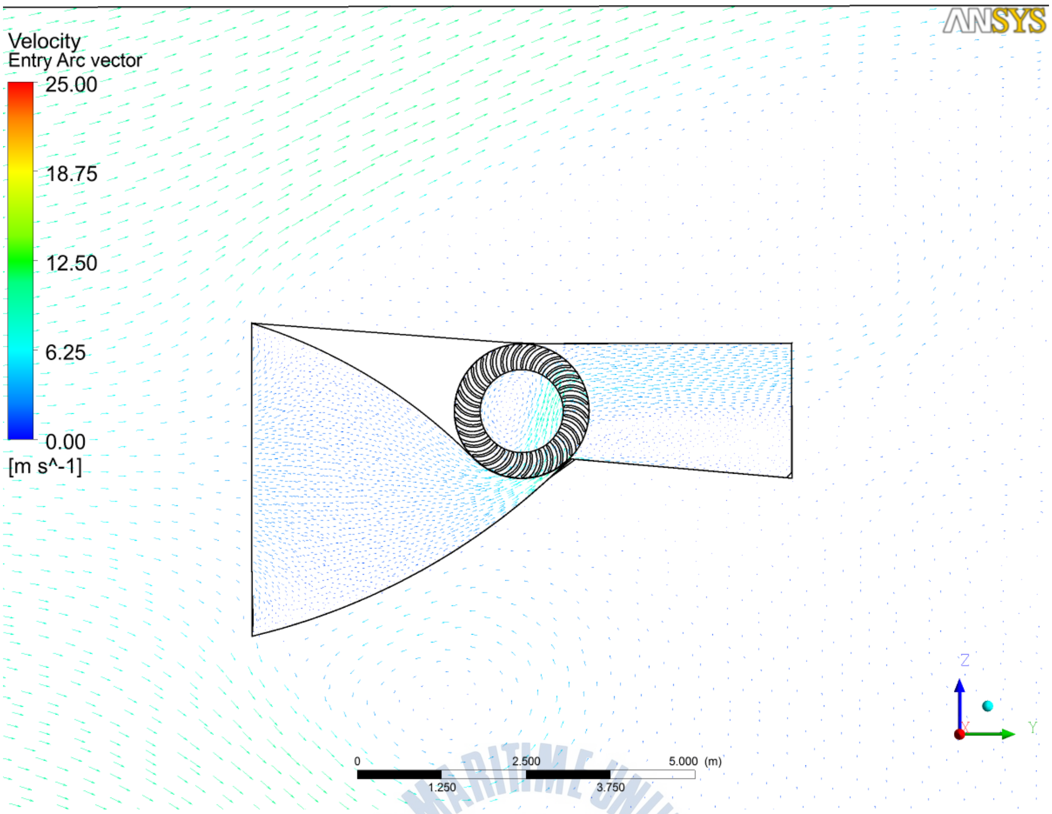

Figure 4.21: Velocity vectors of case 1 of the nozzle analysis

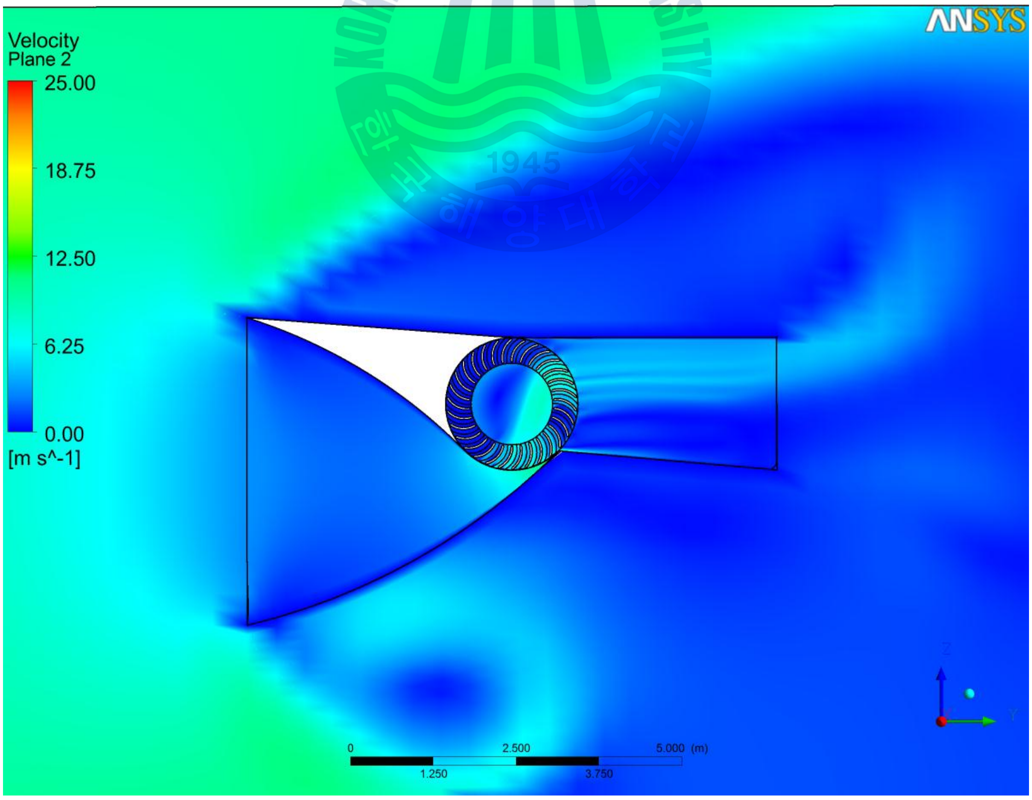

Figure 4.22: Velocity contours of case 1 of the analysis

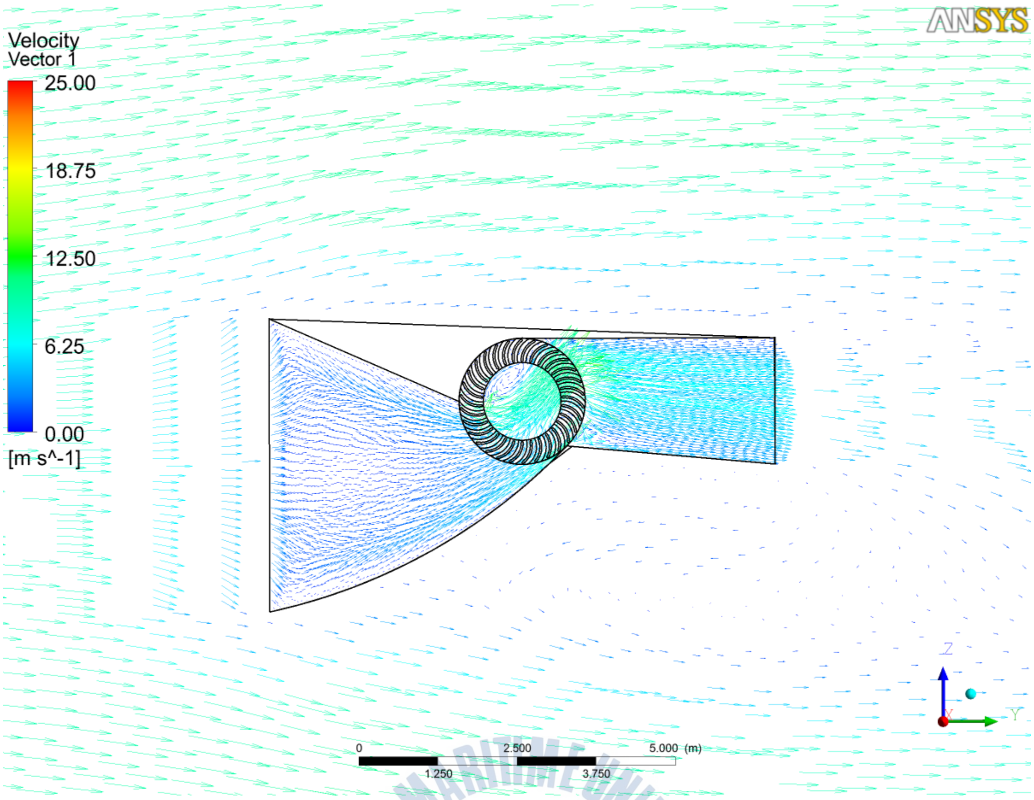

Figure 4.23: Velocity vectors of case 2 of the nozzle analysis

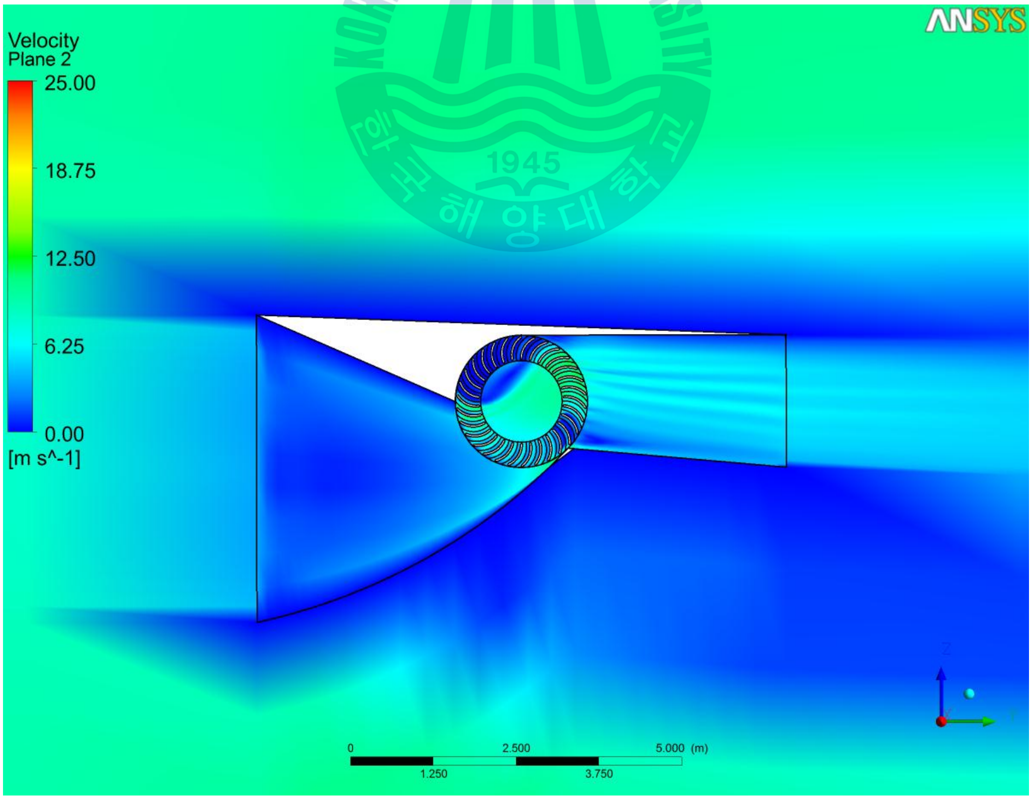

Figure 4.24: Velocity contours of case 2 of the nozzle analysis

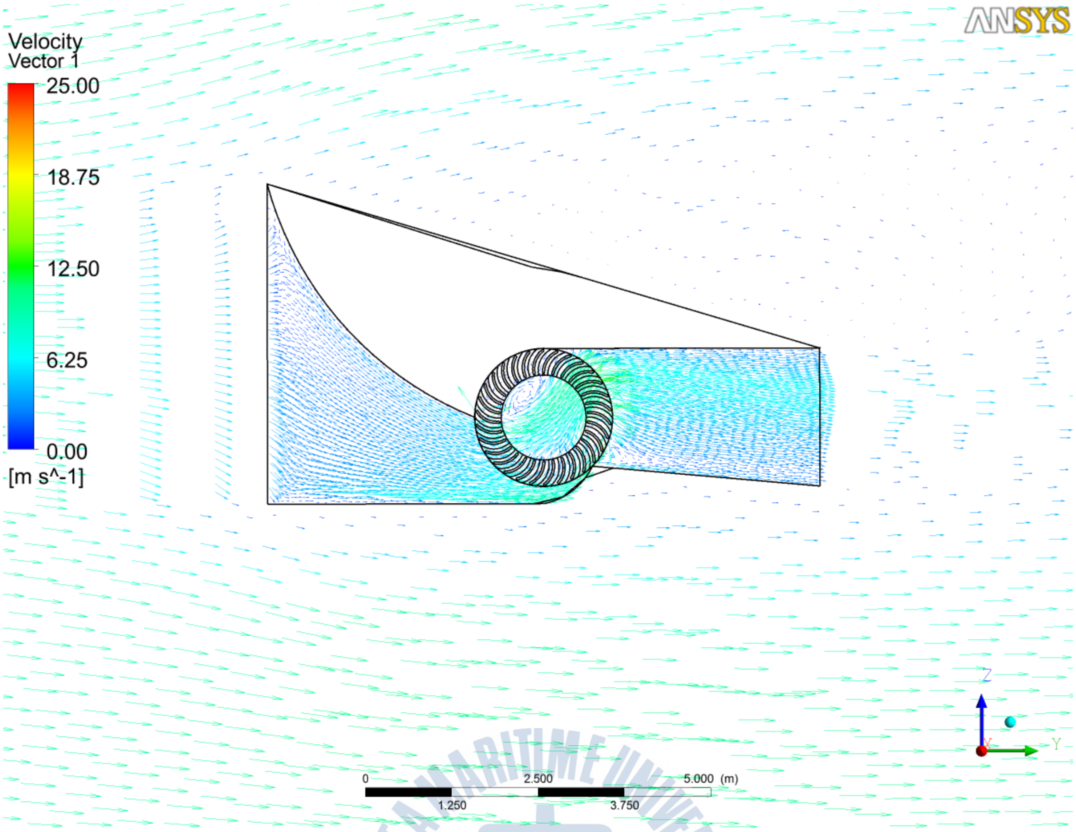

Figure 4.25: Velocity vectors of case 3 of the nozzle analysis

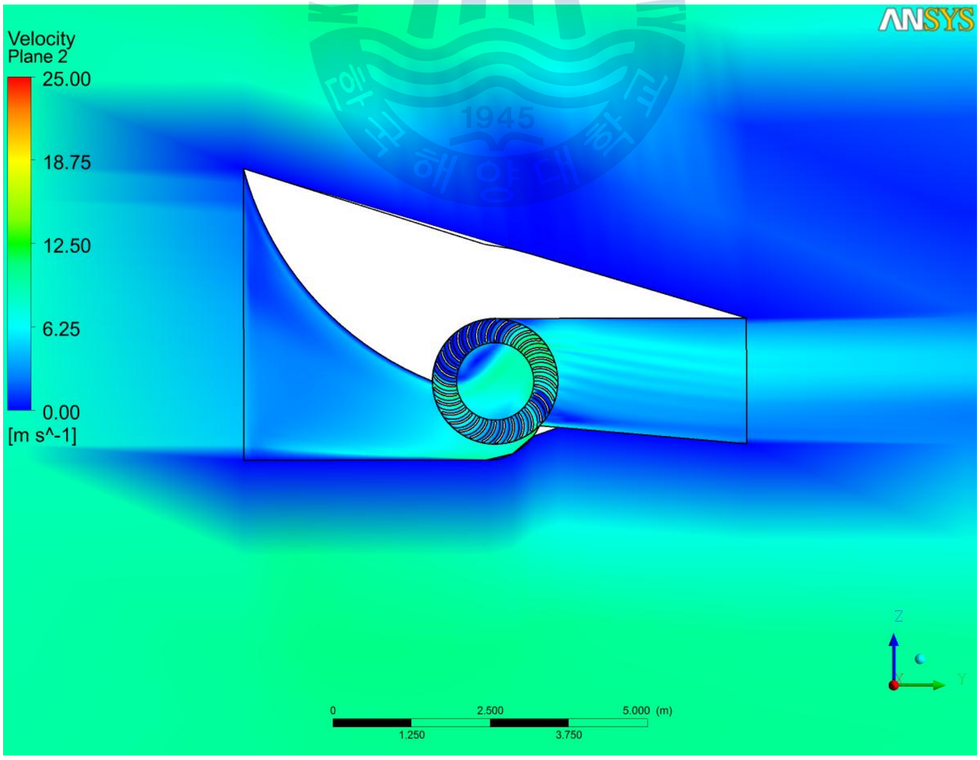

Figure 4.26: Velocity contours of case 3 of the nozzle analysis

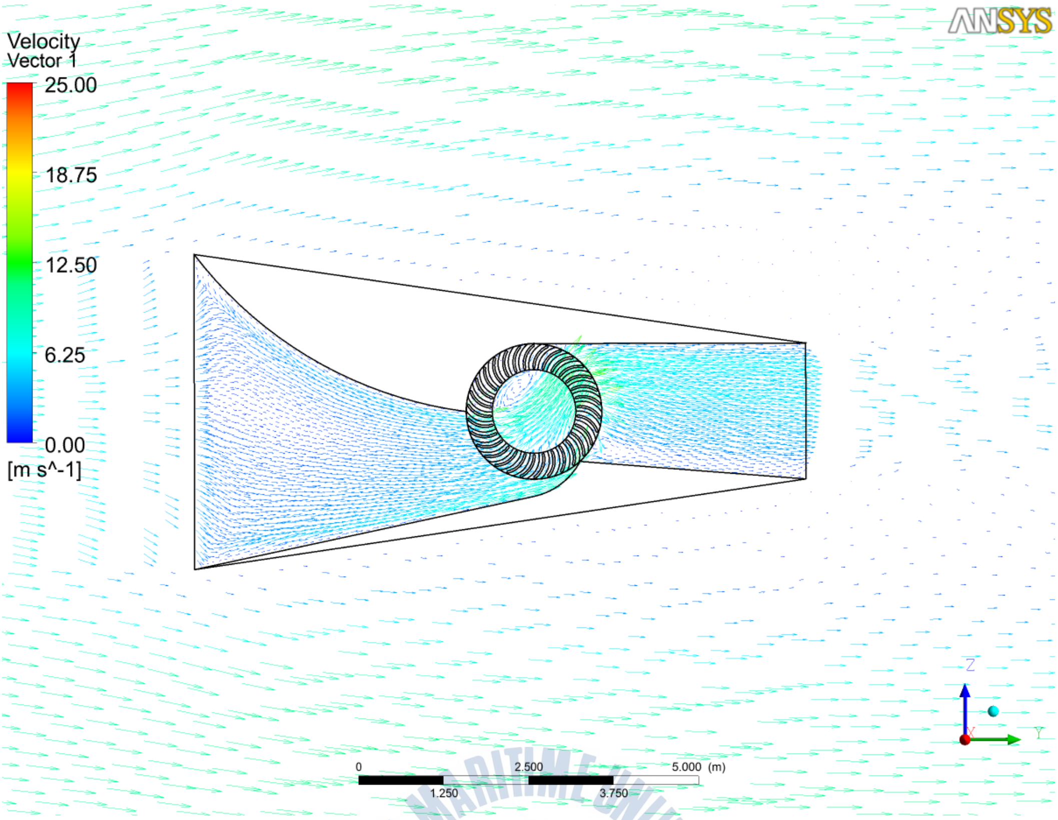

Figure 4.27: Velocity vectors of case 4 of the nozzle analysis

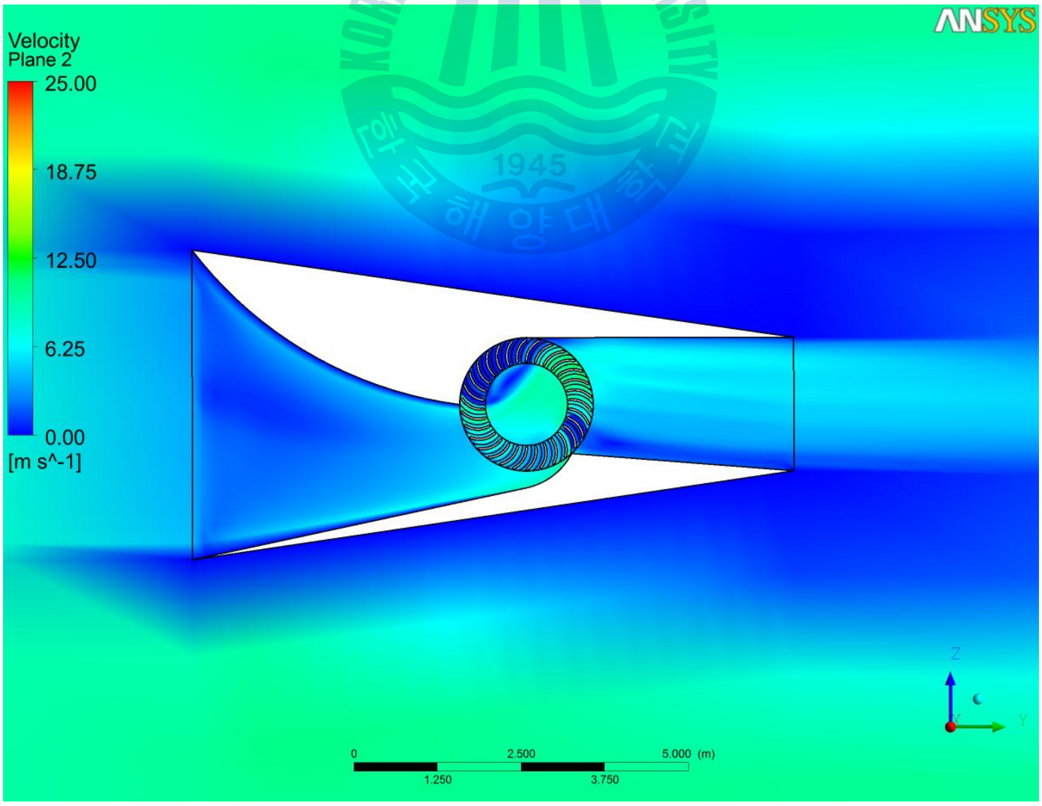

Figure 4.28: Velocity contours of case 4 of the nozzle analysis

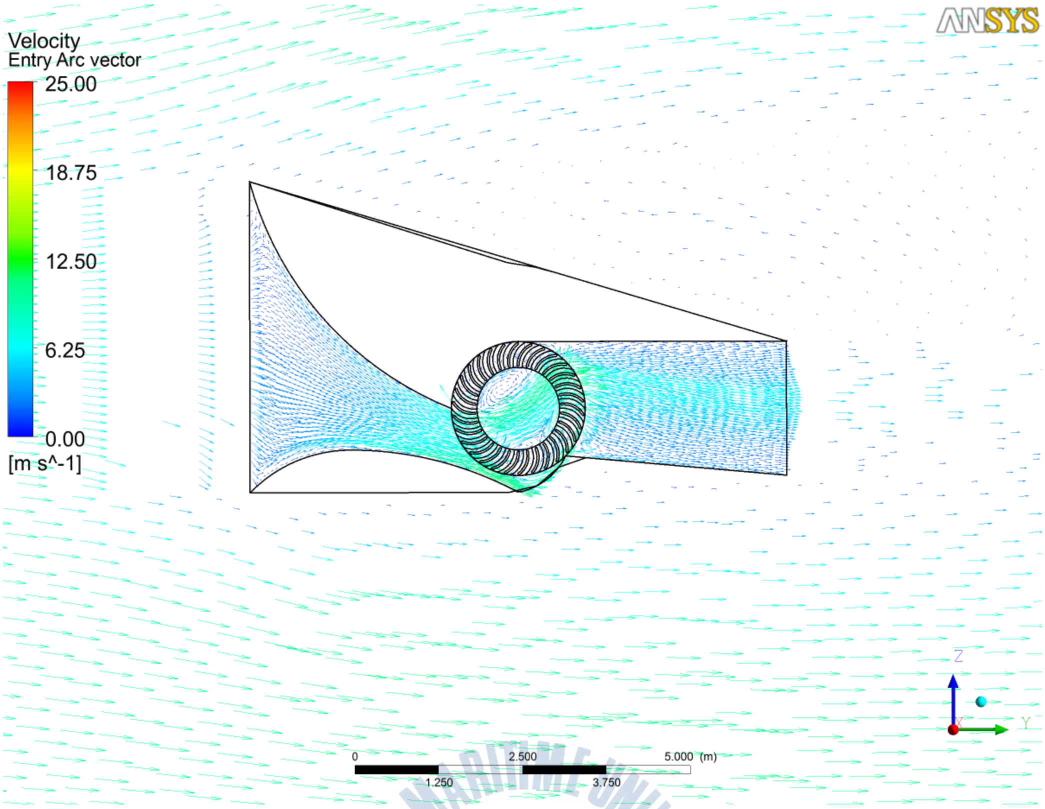

Figure 4.29: Velocity vectors of case 5 of the nozzle analysis

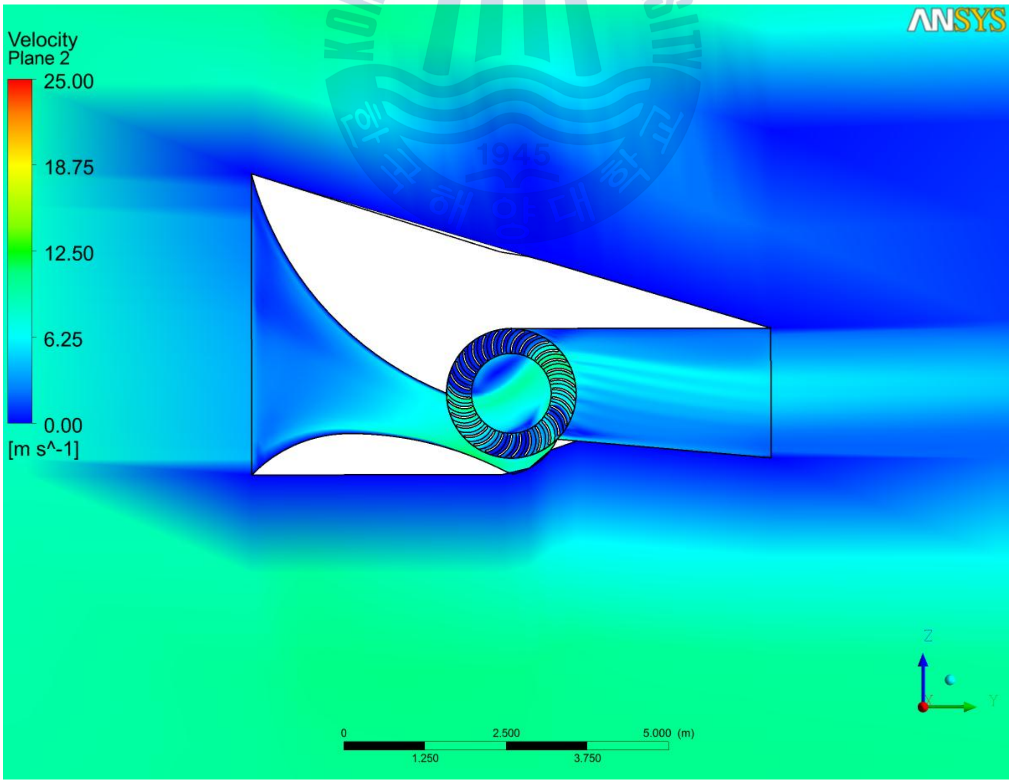

Figure 4.30: Velocity contours of case 5 of the nozzle analysis

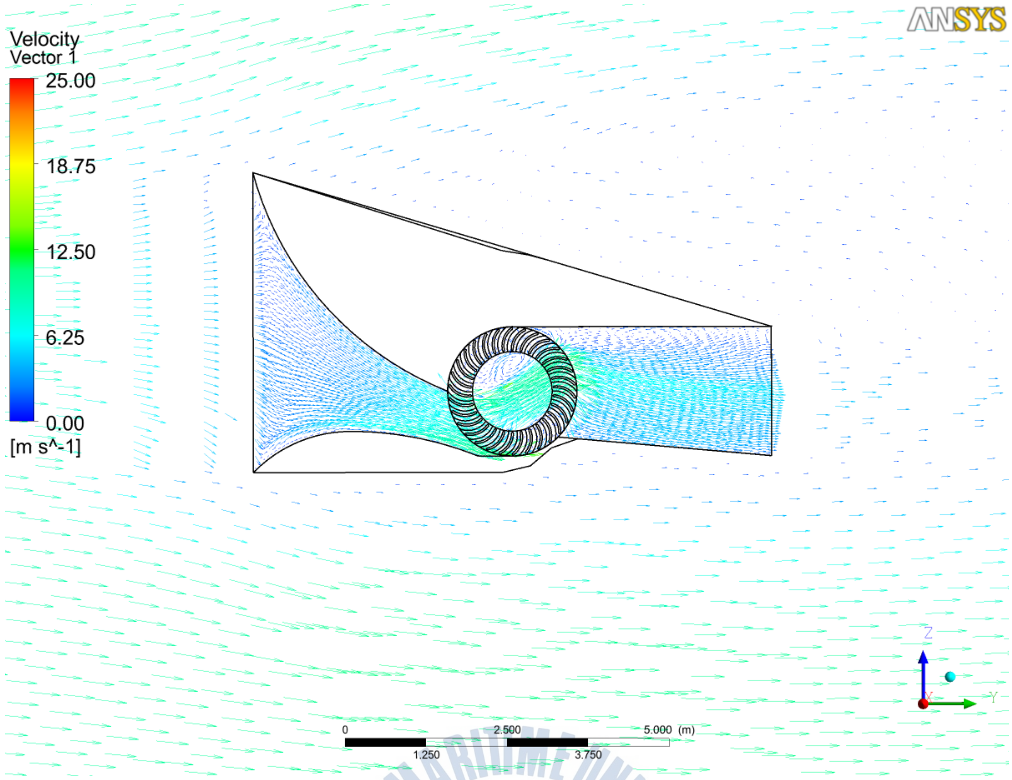

Figure 4.31: Velocity vectors of case 6 of the nozzle analysis

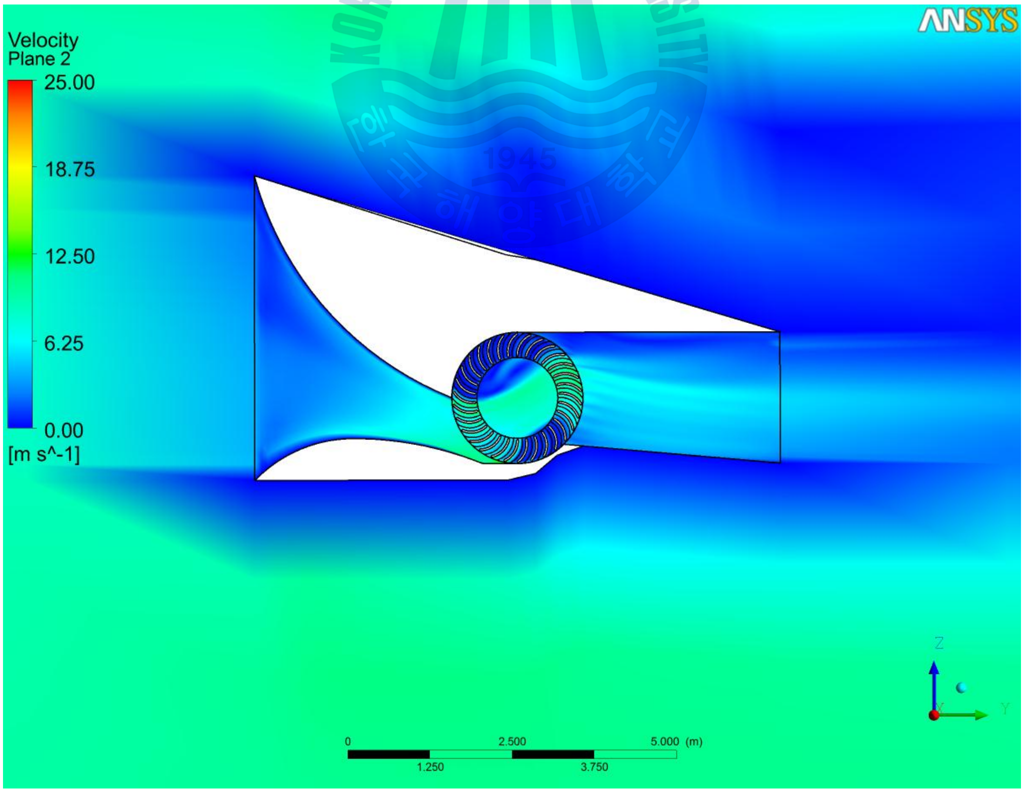

Figure 4.32: Velocity contours of case 6 of the nozzle analysis

Case 3 nozzle shapes were then selected to be used in the subsequent analysis of the effects of the diffuser geometry.

4.2.3 Diffuser entry arc analysis

The results of the diffuser entry arc analysis are shown in Fig.4.33. The C_P versus the TSR for both cases show that the 135° diffuser arc angle with the highest C_P of 0.11 at TSR. This was an improvement by 4.76%. In the next step of analysis, the diffuser arc was set 135° for all cases.

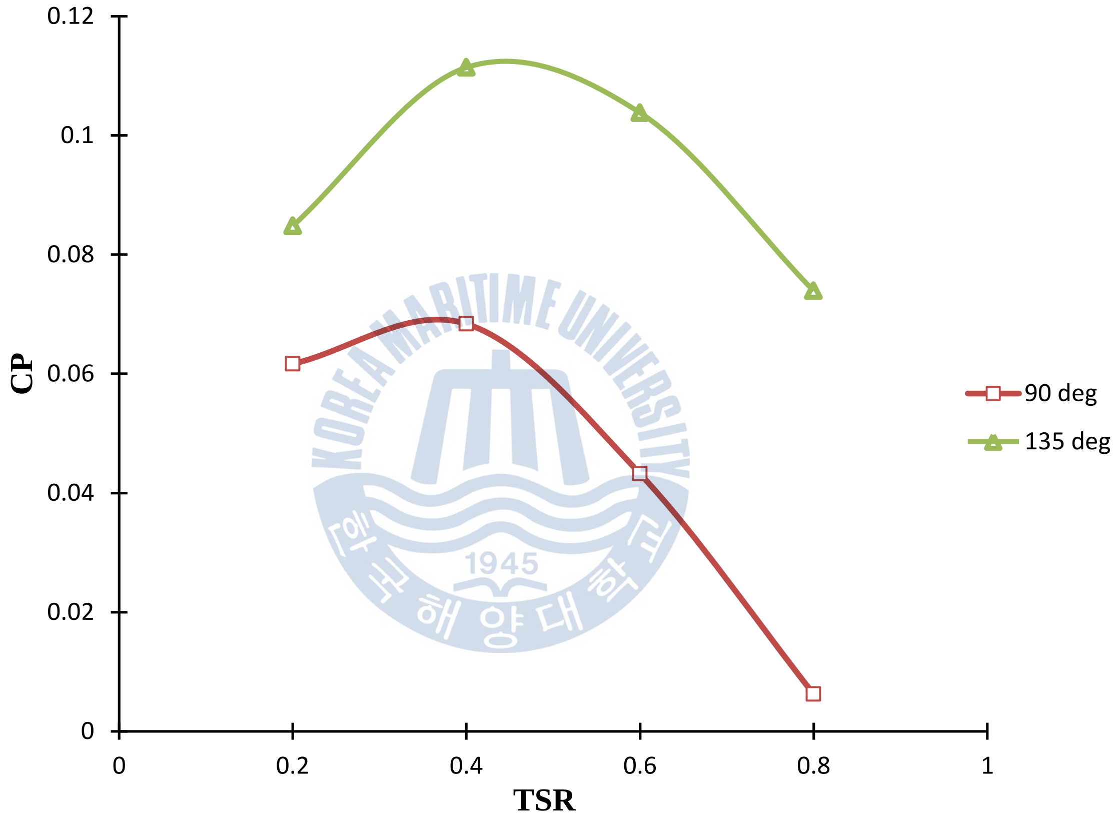

Figure 4.33: Coefficient of power over various tip speed ratios for diffuser entry arc analysis

The flow rate at the turbine entry arc and the flow rate at the diffuser entry arc areas are compared for the two cases in Fig.4.34 over the range of tip speed ratios tested. This figure shows that the 135° diffuser entry arc case has a higher flow rate into and out of the turbine than the 90° case. This significant difference between flow rates for these 2 cases can affect the efficiency of the turbine.

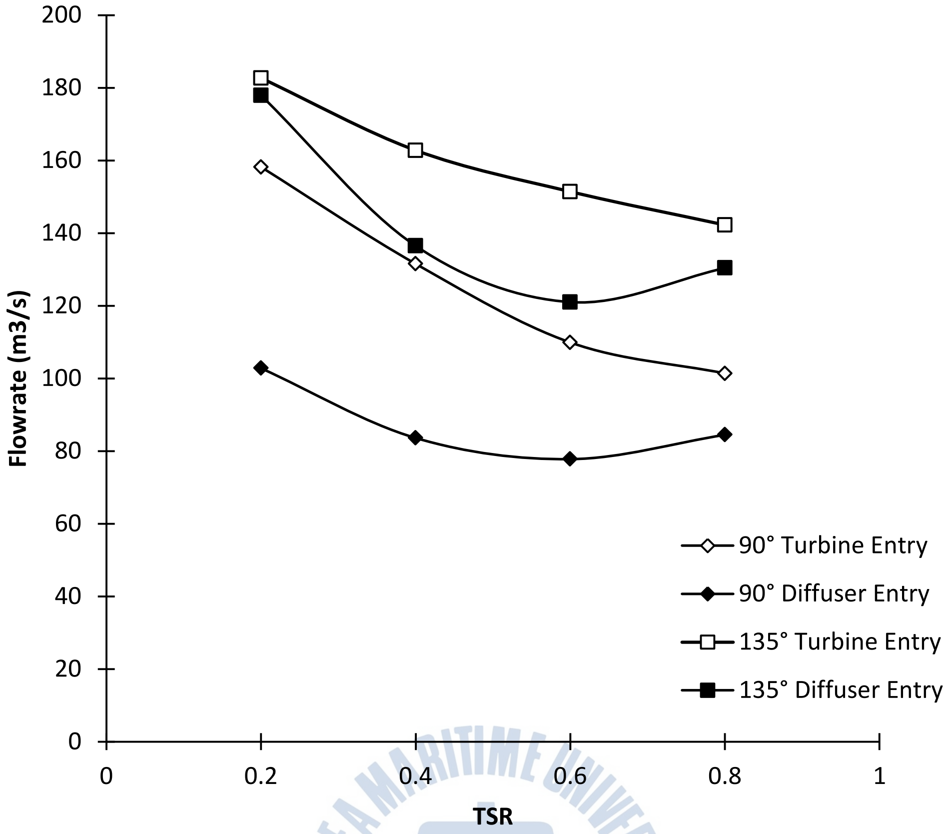

Figure 4.34: Flow rate for both cases at the turbine and diffuser entry arc areas

4.2.4 Diffuser shape analysis

The C_P vs TSR graph for all 4 cases of diffuser shapes is presented in Fig.4.35. All the cases showed very little differences in maximum C_P value. Case 4 had the highest with 0.11 and cases 1, 2 and 3 had 0.098, 0.106 and 0.106 respectively. It should be noted that the case without a diffuser (case 2) provided almost the same amount of power output as the other cases. Therefore, it can be interpreted that the effect of the diffuser is minimal compared to the effect that the diffuser entry arc angle and nozzle.

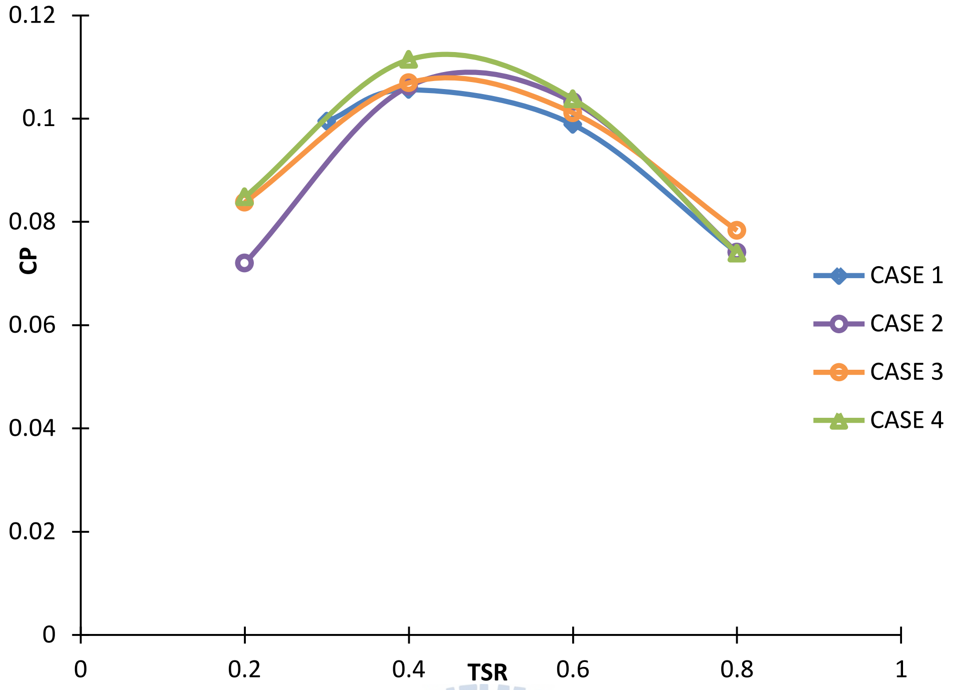

Figure 4.35: Coefficient of power at different tip speed ratios for the diffuser shape analysis

In Fig.4.36, the flow rate at the turbine entry arc region is compared for all 4 cases. Case 1, 3 and 4 is seen to have similar flow rates over the various speed ranges except for Case 2 which has a slightly higher flow rate into the turbine section.

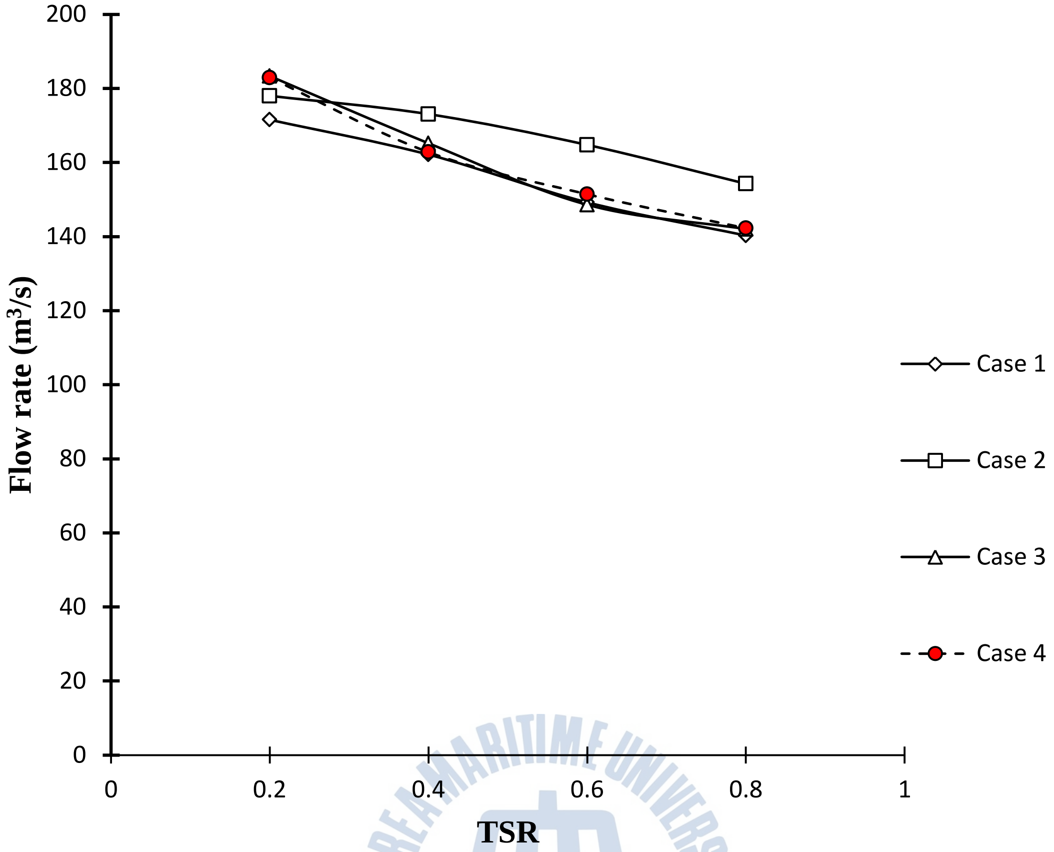

Figure 4.36: The flow rate of the 4 cases at the turbine entry arc region

The following figure, Fig.4.37, shows that Cases 1, 3 and 4 have similar flow rates over the various tip speeds. However, case 2 shows a much lower flow rate out of the turbine.

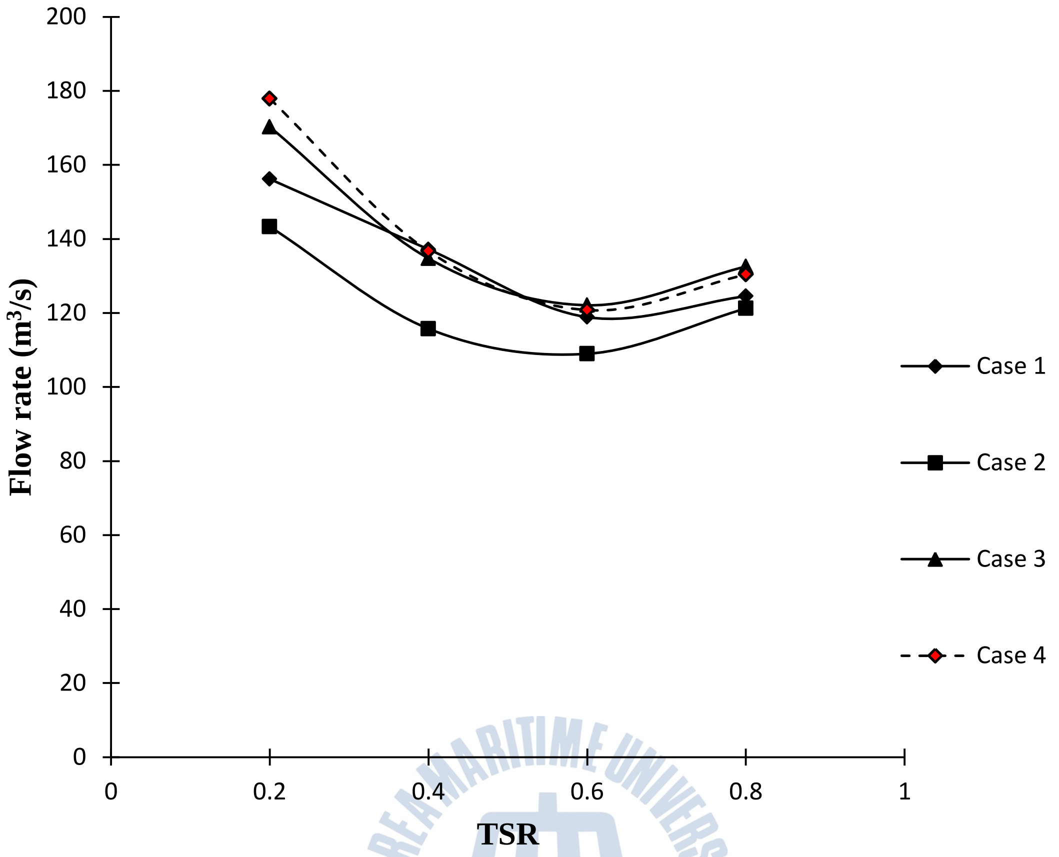

Figure 4.37: Flow for the 4 cases at the diffuser entry arc region

The minimum effect that the diffuser shapes had can be attributed to the two figures, Fig.4.36 and Fig.4.37, showing that cases did not affect the flow rates into the turbine as significantly as the nozzle shapes.

4.3 Comparison of the HAWT and cross flow turbine

Both turbines simulated had the same power to area ratio which meant that the available wind power for both turbines was the same for the area the turbines had to extract the turbine. It was seen that the HAWT had a maximum C_P of 0.45 and a power output of 11.54kW compared to the highest C_P of 0.11 and output power of 2.89kW.

This difference in power output and efficiency is due to the way the turbines extract energy. The HAWT extracts energy by lift forces while the cross flow type turbine uses the drag force. The lift type turbine was able to produce more power per surface area than the drag type turbine.

In addition, in the case of the cross flow turbine, the incoming velocity of the wind slowed down considerably before entering the nozzle. This resulted in a lower kinetic energy available for extraction compared to the HAWT.

Also, it was seen that that if the nozzle shapes improved the flow rate into the turbine, the efficiency of the cross flow turbine improved.

Chapter 5 Conclusion

This study looked at two designs of wind turbines, a conventional horizontal axis wind turbine (HAWT) and a cross flow turbine. The study then analyzed both turbines ensuring that the power to area ratio for the turbines were identical to provide a fair comparison. The study used a finite volume based commercial CFD code ANSYS CFX 13.0 to simulate the performance and analyze the results of the simulation. It was found that:

a) The HAWT produced 11.54kW and had a power coefficient (C_P) of 0.45 at the rated speed of 10m/s.

While the HAWT achieved some design goals, the power versus wind speed curve showed that the turbine required more power control at higher speeds. Possible improvements to the turbine included changing the fixed pitch angle or changing the twist and chord distribution of the turbine.

The streamlines show how the flow behaved over the turbine blades at various wind speeds. At higher speeds, stall occurred and this corresponded to the drop in efficiency of the HAWT but it was suggested to improve the power control method (stall) at higher wind speeds to prevent damage to the turbine.

b) A cross flow turbine for wind applications had been simulated and through various steps the most effective turbine using a nozzle and diffuser was found.

The turbine entry arc analysis found that the 135° case gave the best C_P value of 0.089. The increase in the entry arc angle before the turbine was seen to increase the flow rate in to the turbine allowing more wind power for extraction. In addition, the increase in angle reduced the flow resistance of the turbine and improved the velocity profile at the inlet resulting in a higher entry velocity.

The nozzle shape analysis showed that the best case nozzle improved the C_P by 20% to 0.105. The flow rate graph showed this case had the second highest flow rate into the turbine.

In analyzing the diffuser arc angle, the 135° case gave the higher C_P of about 0.11 with an improvement of 4.76%. This case had a higher flow rate into the turbine entry arc than the 90° case.

In the case of the diffuser shape analysis, the most efficient diffuser shape had a C_P of 0.11 compared the other shapes. However, the graph showed that the diffuser shape was not as effective in increasing the power output compared to the nozzle. The flow rates were not significantly improved compared to the nozzle shapes. It was also seen, that the case without a diffuser was almost as good as the best case.

c) Even though the power to area ratio of both turbines was the same, the HAWT had a much higher efficiency and power output compared to the cross flow turbine. This can be attributed to the way the turbines extract energy. Because the HAWT uses lift forces, it is able to produce more power than the cross flow type turbine.

Furthermore, the air velocity was seen to decrease significantly before entering the turbine. The nozzle increased the velocity of the air and improved the power coefficient.

Acknowledgement

Firstly, I would like to express my gratitude to my supervisor Prof. Dr. Young-Ho Lee for giving me the chance to study in Korea Maritime University in the Flow Informatics Lab and for his patience and knowledge in guiding me.

Secondly, I am also indebted to the thesis committee members: Prof. Dr. Kweon-Ha Park (Chair Person) and Prof. Dr. Hyung Ho Jung (Co-Chairperson) for their patience, time, helpful comments and recommendations.

Thirdly, I wish to acknowledge the help of my numerous lab mates both Korean and foreign for their knowledge and assistance in many areas. Without their assistance, I would not have been able to achieve much.

Finally, I would like to thank my parents for being my pillar of strength during my pursuit of a Master’s degree. Their encouragement, support and interest in my studies helped me tremendously.

References

[1].IEA Renewable Energy Working Party. Renewable Energy... into the mainstream.The Netherlands: Novem; 2002 Oct

[2] World Wind Energy Association. 2012 Half-year Report. World Wind Energy Association. Retrieved November 10, 2012, from http://www.wwindea.org/webimages/Half-year_report_2012.pdf

[3] Hiester, T.R., Pennell, W.T. The Meteorological Aspects of Siting Large Wind Turbines.United States of America: United States Department of Energy; 1981

[4] Manwell.J.F, McGowan.J.G, Rogers.A.L., Wind Energy Explained. John Wiley & Sons LtD, England,2002. Chapter 2, Wind Characteristics and resources; p22

[5] Hau.E, Wind Turbines: Fundamentals, Technologies, Application, Economics.2nd ed.Springer-Verlag, New York; 2006. Chapter 4, Physical Principles of Wind Energy Conversion;p86

[6] Manwell.J.F, McGowan.J.G, Rogers.A.L., Wind Energy Explained. John Wiley & Sons LtD, England,2002. Chapter 3, Aerodynamics of Wind Turbines; p103

[7] Gasch.R, Twele.J, Wind Power Plants: Fundamentals, Design, Construction and Operation.Solarpraxis AG, Germany and James & James(Science Publishers)Ltd, UK.

[8] Gipe.P, Wind Energy Basics, a Guide to Small and Micro Wind Systems. Chelsea Green Publishing Company,1999

[9] Spera.D.A, Wind Turbine Techology, Fundametal Concepts of Wind Turbine Engineering. ASME Press;New York 1994

[10] Betz,A. Das Maximum der theoretisch moglichen Ausnutzung des Windes durch Windmotoren, Zeitschrift fur das gesamte Turbinewesen, 20th Sept 1920. German.

[11] Hau.E, Wind Turbines: Fundamentals, Technologies, Application, Economics.2nd ed.Springer-Verlag, New York; 2006. Chapter 4, Physical Principles of Wind Energy

Conversion; p84

[12] Hau.E, Wind Turbines: Fundamentals, Technologies, Application, Economics.2nd ed.Springer-Verlag, New York; 2006 Chapter 5, Rotor Aerodynamics; p102

[13] Hau.E, Wind Turbines: Fundamentals, Technologies, Application, Economics.2nd ed.Springer-Verlag, New York; 2006 Chapter 5, Rotor Aerodynamics; p139

[14] Van Rooij. R P.J.O.M, W.A.Timmer. Roughness Sensitivity Considerations for Thick Rotor Blade Airfoils.AIAA-2003-0350

[15] Timmer.W.A, van Rooij. R.P.J.OM. Summary of the DELFT University Wind turbine Dedicated airfoils.AIAA-2003-0352

[16] Kim.B.S. A Study on the Optimum Design of the Horizontal Axis Wind Turbine and Its Aerodynamic Performance Analysis. Ph.D. thesis. Korea: Korea Maritime University;2005

[17] Ingram.G, Wind Turbine Blade Analysis using the Blade Element Momentum Method .Durham University Retrieved, Febuary 04, 2012, http://www.dur.ac.uk/g.l.ingram/download/wind_turbine_design.pdf

[18] Holgate.M.J., A Cross Flow Wind Turbine.Proceedings of the International Symposium on Wind Energy Systems; Sept 7-9 1976; Cambridge, England.

[19] Shigetmitsu.T, Fukutomi.J, Takeyama.Y.,Study on Performance Improvement of Cross-Flow Wind Turbine with Symmetrical Casing. Journal of Environment and Engineering.2009.Vol.4(3): pp490-501

[20] Kishinami.K, Suzuki.J, Kon.N, Ambarita.H, Muramatu.Y, Hirama.K and Ibano.H. Proceedings of Renewable Energy; Oct 2006; Chiba, Japan.

[21] Blazek.J. Computational Fluid Dynamics-Principles and Applications. Elsevier Science Ltd, London; 2001. Chapter 3, Principles of Solution of the Governing Equations; p37

[22]ANSYS CFX-Solver Theory Guide. Release 12.0,2009

[23] Menter,F.R., Two equation eddy vicosity turbulence for engineerin applications. AIAA-Journal.1994.Vol32(8): pp.1598-1605

[24] Kim.K.P, Ahmed.M.A, Lee.Y.H. Efficiency improvement of a tidal current turbine utilizing a larger area of channel. Renewable Energy.2012 July 9.Vol.48. pp.557-564

[25] Lindenburg C. Investigation into rotor blade aerodynamics. ECN-C-03-025.Petten, Netherlands; 2003

[26] Snel H, van Holten Th. Review of recent aerodynamic research on wind turbines with relevance to rotorcraft, data and riddles on dynamic inflow, flow field of yawed rotors and rotating 3-D stall. Proceedings of the 20th Rotorcraft forum. Amsterdam; October 4-7, 1994.